UNIVERSITÀ DEGLI STUDI
DI MODENA E REGGIO EMILIA

Dottorato di ricerca in Information and Communication Technologies

Ciclo XXXVII

THERMAL AND MECHANICAL MODELLING AND ANALYSES OF WOUND FIELD SYNCHRONOUS MACHINES FOR TRANSPORTATION APPLICATIONS

Candidato: Alessandro Guiducci

Relatore: Prof. Giovanni Franceschini

Correlatore: Prof. Davide Barater

Coordinatore del Corso di Dottorato: Prof. Luigi Rovati

TABLE OF CONTENTS

List of Figures

List of Tables

List of Acronyms

WFSM	Wound field synchronous machine
WFSG	Wound field synchronous generator
LPTN	Lumped parameter thermal network
TEC	Thermal equivalent circuit
FEM	Finite element methods
CFD	Computational fluid dynamics
2D	Two-dimensional
3D	Three-dimensional
PEEK	Polyether ether ketone
VHCF	Very high cycle fatigue
HTC	Heat transfer coefficient
MEA	More electric aircraft
EV	Electric vehicle
HEV	Hybrid electric vehicle
PM	Permanent magnet
AC	Alternating current
DC	Direct current
SRM	Switched reluctance motor
IPM	Interior permanent magnet
SUV	Sport utility vehicle

NEDC	New European drive cycle
WPT	Wireless power transfers
SMC	Soft magnetic material
MMF	Magneto motive force
THD	Total harmonic distortion
CHT	Conjugate heat transfer
BC	Boundary condition
PD	Partial discharge
FE	Finite Element
IDG	Integrated Drive Generator
NdFeB	Neodymium Iron Boron
SmCo	Samarium Cobalt
FEA	Finite Element Analysis
HFVT	High-Frequency Vibration Technique
VHCF	Very High Cycle Fatigue

Glossary of Symbols

D air gap diameter

c_d empirical coefficient

L active axial length

S power

Φ flux per pole

B_m average value of flux density

p pole pairs

N number of active sides per phase

V voltage

f frequency

kf, kd, kp form factor, distribution factor, pitch factor

μ friction coefficient

I current

ρ air gap fluid density

R1 outer radius of inner cylinder

R2 inner radius of outer cylinder

δ air gap thickness

Ta Taylor number

Nu Nusselt number

Fg geometrical factor

ν kinematic viscosity of fluid

k thermal conductivity

va axial air velocity

Pr Prandtl number

d hollow shaft diameter

Ω rotational speed

ΔV delta voltage difference

K kurtosis coefficient

ABSTRACT

Wound-field synchronous machines (WFSMs) have a long-established history in power generation due to their reliability and controllability. However, when applied to transportation, particularly as generator in aerospace and motor in automotive sectors, achieving the necessary power density and efficiency becomes a challenge. To meet these demands, a comprehensive multi-physics design and modelling approach is essential. This thesis proposes a methodology that integrates advanced thermal and mechanical management techniques to optimise WFSMs for transportation applications. Innovative modelling techniques such as 3D thermal equivalent circuit (TEC), 2D and 3D finite element (FE) thermal and mechanical models, and 3D computational fluid dynamics (CFD) models are employed to assess and improve the machine's performance. In addition to the theoretical and computational work, experimental studies are conducted to monitor the fatigue of Polyether ether ketone (PEEK) insulation material, providing insights into its durability in operational environments. This research emphasizes the thermal and mechanical aspects of WFSM design, positioning them as strong contenders against permanent magnet machines for transportation applications.

ACKNOWLEDGEMENTS

This last journey of my academic training, the doctorate, has also come to an end. Here, I write the part that I prefer because I write it from my heart. They have been three intense years, where each one has been marked by a precise time. The training and knowledge in Italy the first, the time in United Kingdom the second and the time in Austria the third.

I would like to express my deepest gratitude to my entire research group Melting Lab at the Department of Engineering "Enzo Ferrari" of the University of Modena and Reggio Emilia, Modena, Italy. In particular, my supervisor Prof. Stefano Nuzzo who accompanied me on this journey with his criticism that made me grow. My tutor Prof. Giovanni Franceschini for always being available in moments of comparison and choice. My industrial tutor Prof. Davide Barater for his guidance in the doctorate and to all my colleagues for the good time together in the laboratory and in the various conferences and summer schools.

I would like to express my heartfelt gratitude to my supervisor Dr. Rafal Wrobel who guided me with such accuracy and precision during my six months secondment at Newcastle University, Newcastle upon Tyne, UK. I thank with a big smile all the British colleagues who welcomed me as a local and made this experience unforgettable.

I would like to express my heartfelt gratitude to my supervisor Dr. Philipp Renhart and Prof. Florian Grün during my six months secondment in Austria at the Montanuniversität Leoben. For the welcome given to me, the trust and for giving me the opportunity to work in a qualified research group and laboratory.

I thank my loved ones, who I carry in my heart wherever I go, especially my family, my friends and all those angels who guided me in these 3 years to live them in transparency.

I thank God, who has never left me alone but rather made me live these three years as a beloved son with his beauty, greatness and nobility.

SINTESI DEI CONTENUTI IN LINGUA INGLESE

This thesis explores the design, optimisation, and analysis of Wound-Field Synchronous Machines (WFSMs) in transportation applications, particularly focusing on the aerospace and automotive industries. WFSMs, which rely on field windings to generate the necessary magnetic field, are widely used in power generation for their fault tolerance, reliability, and cost-efficiency. However, their application in high-performance fields such as transportation poses significant challenges, especially in terms of power density, thermal management, structural integrity and fatigue monitoring. The research presented in this thesis aims to address these challenges through a comprehensive multi-physics design and modelling approach.

Research Objectives

The main objective of the thesis is to enhance the performance and durability of WFSMs for transportation by improving their thermal and mechanical designs. This is achieved through the development of advanced modelling techniques that combine electromagnetic, thermal, and mechanical considerations. The research is divided into two main case studies:

1. **High-Speed WFSM Generator for Aerospace Applications:**

- The aerospace sector demands high-power density and efficiency, especially in the context of the "More Electric Aircraft" (MEA) trend, where electric systems replace traditional pneumatic and hydraulic systems.
- The study focuses on the refined structural design of a high-speed WFSM generator. One key challenge is managing the heat generated by the rotor windings, which must be cooled efficiently to avoid overheating and structural failure at high rotational speeds.

- The rotor, with its salient poles, faces challenges in high-speed applications due to mechanical stress and centrifugal forces. The thesis proposes a solution by adding a 4 mm layer of non-electrical steel to the rotor's periphery, enhancing its structural integrity and allowing it to withstand the demands of high rotational speeds. This design modification improves both the mechanical stability and thermal management of the rotor.
- The solution allows an axial flow cooling, where air is forced through the rotor assembly to enhance heat dissipations
- This project resulted in the design of a machine that meets the high-performance needs of hybrid or fully electric aircraft.

2. Rotor Cooling in Traction Applications (Automotive):

- The automotive industry requires motors capable of high torque at low speeds, and low torque at high speeds at cruising, with strict constraints on size, weight, and efficiency. WFSMs, while less common in traction motors compared to permanent magnet machines, have the potential to meet these requirements, particularly due to their inherent reliability and sustainability (as they do not require rare-earth materials).
- The research investigates various rotor cooling techniques to improve the thermal management of high-speed WFSMs. Using analytical and numerical methods, including Thermal Equivalent Circuit (TEC), Finite Element (FE) and Computational Fluid Dynamics (CFD) models, the study evaluates different cooling strategy. These include an axial fan that generates axial airflow to actively cool the rotor, and an oil-flooded hollow shaft for passive cooling. The combination of active and passive cooling systems significantly enhances the machine's overall thermal performance and operational efficiency.
- The case study demonstrates that active cooling, involving fluid circulation through the rotor, leads to better heat management and higher power output, albeit with increased system complexity and mechanical losses.

Key Challenges Addressed

Thermal Management: One of the primary difficulties in WFSM design is the management of heat generated by the rotor's field windings, especially in high-speed operations. This thesis develops and applies advanced thermal models, including 3D TEC, 2D and 3D FE models and 3D CFD simulations, to assess and optimize heat transfer in both aerospace and automotive applications.

Mechanical Integrity: High-speed operation induces significant mechanical stresses, particularly due to centrifugal forces on the rotor's end-windings and rotor's tips. The research includes mechanical analyses to ensure structural integrity, using 2D and 3D finite element models to evaluate the rotor's performance under these extreme conditions.

Fatigue Monitoring of PEEK: The durability of insulation materials, particularly polyether ether ketone (PEEK), is critical in maintaining the long-term reliability of WFSMs. The thesis includes experimental work on PEEK, conducted under high-vibration conditions typical in aerospace and automotive environments. Using an electrodynamic shaker, the study simulates real-world vibrations and monitors the material's failure under different loading conditions.

Experimental Studies

A significant portion of the research is devoted to experimental testing, particularly on the fatigue and failure monitoring of PEEK insulation materials. These experiments were conducted at Montanuniversität in Leoben, Austria. The main focus of the activity was the development of time and frequency-based methods, which allow an early detection of damage during stress-controlled very high cycle fatigue (VHCF) experiment using an advanced electrodynamic shaker.

Contributions to Research

The thesis contributes to the growing body of knowledge on WFSM design by:

- Proposing a multi-physics modelling methodology that integrates electromagnetic, thermal, and mechanical analyses to optimize WFSMs for transportation applications.
- Demonstrating the feasibility of high-speed WFSMs in aerospace and automotive applications, particularly as a sustainable, rare-earth-free alternative to permanent magnet machines.
- Developing thermal management models, particularly for the rotor, to improve the thermal performance of WFSMs without compromising structural integrity.
- Providing experimental insights into the long-term reliability of PEEK insulation material in high-vibration environments.

Future Directions

The research highlights several areas for further investigation, including:

- Continued development of advanced cooling techniques, especially for the rotor assembly, where heat removal is most challenging.
- Exploration of new materials and manufacturing processes, such as additive manufacturing, to improve the structural and thermal performance of WFSMs.
- Further refinement of the electromagnetic design to enhance power density and reduce losses.

Conclusion

This thesis demonstrates that WFSMs, with their robust design and fault-tolerant characteristics, are a viable and sustainable option for transportation applications. By addressing key challenges in thermal management, mechanical integrity, and material durability, the research positions WFSMs as strong competitors to permanent magnet machines, offering a rare-earth-free solution for the electrification of both aerospace and automotive sectors.

1. INTRODUCTION

WFSMs represent a well-established topology of electrical machines that rely on field windings to generate the magnetic field essential for their operation. These machines are extensively used as generators in various low-speed applications to meet electrical energy demands. Compared to their rare earth permanent magnet counterparts, WFSMs offer several advantages, including ease of control, inherent fault tolerance, lower cost, and the use of more sustainable materials. However, permanent magnet machines are known for their superior power density and efficiency, making them highly attractive for traction applications where reducing the weight and volume of the electric drive system is crucial. This is further supported by the robust structure of the rotor in permanent magnet machines, allowing them to operate at relatively high speeds. In contrast, the rotor of a WFSM features salient poles, making it less suitable for high-speed applications.

While WFSMs have been widely adopted and studied as power generators in grid-connected and isolated power plants, their use as traction motors is limited and remains an area of active research. This thesis investigates the mechanical and thermal performance of high-speed wound-field machines for transportation applications, with the goal of providing a suitable, rare-earth-free solution for the electrification of the transportation sector, particularly in aerospace and automotive contexts. The electromagnetic aspects are explored through a case study of a high-speed wound-field generator designed to achieve high fault tolerance and power density, particularly for "more electric aircraft" applications.

The rotor assembly in electrical machines poses substantial challenges for effective heat removal due to the rotational nature of the system, which restricts the thermal pathways for dissipating generated heat. Additionally, factors such as system integration and mechanical power loss must be carefully considered to achieve a well-balanced thermal management and electrical machine design. This thesis

explores various rotor cooling techniques, including the circulation of fluid (air and/or oil-based coolant) through the rotor assembly.

Another critical aspect considered is the longevity of insulation materials under various conditions, such as the high-vibration environments typical of transportation applications. In aerospace applications, these vibrations are encountered during turbulence in cruising, with the most significant impact occurring during landing and take-off. Similarly, in automotive applications, vibrations are a common factor during normal road use, especially in hybrid vehicles due to the combined presence with the internal combustion engine.

An in-depth study and experimental investigation are presented on the failure monitoring of PEEK, the most commonly used insulation material in electrical machines. Since insulation degradation leads to failure of the electrical machine, it is of fundamental importance to monitor its behaviour under high vibration conditions.

Given these challenges, a multi-physics approach emerges as the ideal tool for the design of electrical machines, allowing for simultaneous consideration of electromagnetic, thermal, and mechanical behaviours. This work, therefore, focuses on improving analyses, modelling and testing aimed at enhancing the thermal and mechanical performance of WFSMs, building from a preliminary electromagnetic design.

1.1. Project description

The salient pole WFSM has a long history of reliable performance, making it an ideal choice for efficient electrical generation applications. This project aims to analyse and model the WFSM to optimize its mechanical and thermal capabilities, enhancing its performance and positioning it as a sustainable, rare earth-free option for the green transportation sector. To achieve this, a multi-physics approach is employed, beginning with electromagnetic design and progressing to thermal assessment to ensure machine temperatures remain within insulation limits. The

project involves the development of advanced analytical and numerical models, including TEC, 2D and 3D FE thermal models, and 3D CFD models. The focus is on the thermal management of the rotor assembly, which presents significant challenges due to the difficulty of effective heat removal from a moving part surrounded by air. This work was undertaken by the author during a six-months secondment with the thermal management group at Newcastle University, Newcastle upon Tyne, UK. Mechanical analyses are conducted to verify the rotor's structural integrity under high-speed operations. Initially, a 2D FE model assesses the preliminary rotor geometry's structural soundness. Subsequently, a 3D FE model, incorporating the rotor's actual geometry, evaluates the centrifugal forces from the rotor end-windings. While the focus is on this specific topology, the methodologies and models developed in this project can be broadly applied to various electrical machines and applications. To ensure the longevity of the electrical machine in high-vibration applications, failure monitoring of the insulation was conducted through experimental activities at Montanuniversität, Leoben, Austria, during a six-months secondment with the mechanical research group.

A. High-Speed Wound-Field Synchronous Generator for Aerospace applications and its main Challenges

This case of study is focused on refined structural design and thermal analyses of a high-speed wound-field synchronous generator aimed at satisfying the power demands on board of aircraft equipped with hybrid or electric powertrains. This work emerges from the need of evaluating in detail the temperature distribution inside a synchronous generator and to re-design the rotor retention system to allow high-speed rotation of the rotor while improving the rotor heat dissipation. The electromagnetic design was carried out in a previous research developed in collaboration with the University of Pisa, Pisa, Italy, and the University of Nottingham Ningbo, Ningbo, China. The rotor of a WFSM, with its salient poles, is generally unsuitable for high-speed operations. Structurally, the project addresses the centrifugal forces acting on the end-windings by adding a layer of non-magnetic material at the rotor's periphery. Thermally, it optimises cooling by allowing axial flow, generated by a fan on the shaft, by removing of the previously designed rotor

cage. The details of the multi-physics models and analyses are covered in deep in Chapter 3. The results demonstrate that the designed motor is suitable for high-speed aircraft applications.

B. Thermal Modelling of Advanced Rotor Cooling Solutions for Traction applications and its main Challenges

This project explores alternative thermal management techniques for the rotor assembly of a high-speed salient-pole wound-field synchronous motor used in traction applications. To support the analysis, a number of design tools are developed and used, including a simplified correlation-based TEC, FE and CFD methods descripted in Chapter 4. This methodology offers a computationally efficient approach, with the TEC used for initial trade-off studies and high-fidelity CFD applied at later stages of development. A case study motor design is used to demonstrate the methodology. Initial theoretical predictions suggest that active rotor cooling provides significant performance gains compared to the baseline design with passive heat removal. Both the convective heat transfer coefficient (HTC) and rotor power loss handling are analysed in the context of overall motor performance and the torque-speed envelope. Additionally, insights regarding thermal management, motor system integration, and additional mechanical power loss are discussed.

C. Monitoring of PEEK material failure under high vibration applications

High-vibration conditions are simulated using an electrodynamic shaker. The process begins with the identification and modelling of the electrodynamic shaker itself. Experiments are then conducted by testing PEEK samples under various loading conditions. Through signals post-processing of the experiment data, it is possible to predict the specimen's failure. All details are thoroughly covered in Chapter 5.

Proposed solution (s)

Considering the identified issues highlighted above for the WFSMs, it is clear that there is a potential for improving the performance of the WFSM without introducing any rare earth materials.

In particular,

A. The aerospace generator study aims at using standard cooling solutions to minimize the cost, the mechanical analysis is aimed at achieving the thickness of the end plate of 38NiCrMo4. At 15 000 rpm a layer of 4 mm is added at the end-caps of the rotor. This solution also has thermal advantage as it guarantees an axial air flow to cool the rotor.
B. This work presents a methodology (design flow) for assessing power loss handing capability of alternative rotor assemblies commonly found in electrical machines. The proposed simplified TEC-based approach allows for a rapid evaluation of the rotor heat removal capability for a set of predefined operating conditions like maximum allowable rotor temperature, type of coolant, coolant temperature and mass flow. The proposed methodology has been demonstrated on a case study high-speed wound-field salient-pole synchronous motor for traction applications. A set of alternative rotor cooling scenarios was evaluated showing that active cooling involving passing air through the rotor body offers here the best performance. The improved heat removal leads to significant performance gains over the entire torques speed envelope of the analysed motor. Note that the analysed baseline motor, relies on the rotor induced (passive) cooling only with limited heat removal capability at lower motor speeds. However, the active motor/rotor cooling comes at an expense of higher complexity of the motor and thermal management system, and mechanical power losses due to aerodynamic and/or fluid churning effects.
C. The most notable signal variation across different load levels is observed in the voltage, where an increase in the voltage difference (ΔV) is evident as the load level rises.

1.2. Aims ad objective

As outlined in the introductory sections, this thesis focuses on modelling and analysing WFSM for aerospace and automotive applications, with the goal of enhancing performance, reducing costs, and improving manufacturing processes. The primary novelty of this thesis lies in the multi-physics approach for designing and modelling electrical machines, utilizing advanced analytical and numerical tools to identify optimal solutions for the required performance. Specifically, it includes the use of a layer of non-electrical steel to ensure the structural integrity of the rotor at high speeds and the integration of an axial fan and hollow shaft for cooling the rotor.

In summary, the main aim of this project is to investigate the proposed WFSM modelling approach and consolidate the potential improvements in performance combining the electromagnetic aspect with the thermal and structural ones. To achieve this aim, several objectives and deliverables were identified at the project's outset, including:

1. Building a comprehensive understanding of wound-field high-speed synchronous machines for transportation applications with a particular focus on:
   a) Structural performance
   b) Thermal performance
2. Proposing and developing a new modelling approach based on multi-physics through analytical and numerical techniques that allow for accurate yet time-efficient modelling of the machines in question.
3. Proposing and investigating solutions to maximize the performance and the longevity of the machines.

1.3. Thesis outline

The thesis structure is organized in such a way to report all the logical passages and steps of the methodology followed towards the completion of the objectives of this project.

Chapter 1 introduces the project by highlighting the required applications and outlining aims and objectives of the project.

In Chapter 2, these concepts are strengthened by providing relevant background and a review of existing methods in terms of WFSM design, modelling and analysis, with a special focus on multi-physics approach for aerospace and automotive application.

The knowledge gained from the literature review is used in Chapter 3 and Chapter 4 to develop and implement fast and accurate analytical and numerical models such as TEC, FE and CFD of the studied topology machine. It is the 'heart' of the whole work.

In Chapter 3, the validated models are used to assess the thermal and structural performance of a WFSM for aerospace application aimed to satisfy the MEA trend.

In Chapter 4, the validated models are used to assess in deep the thermal performance of a WFSM as propulsion system for automotive application aimed to design a well alternative to IPM machine. Focusing mainly on rotor heat exchange.

In Chapter 5, the failure monitoring experiment of the PEEK material is investigated.

Chapter 6 concludes this thesis, by representing overall discussions and further work to be done in the related applications.

2. LITERATURE REVIEW

This chapter deals with the literature review carried out for preliminary investigation of the challenge related to this project which were introduced in Chapter 1. In particular, focus is given to the review of the methods aimed at improving the performance of WFSM and adapting it for transportation applications, which have been matter of research in recent literature.

2.1. Introduction

Nowadays, reducing global emissions is widely recognized as essential for limiting global warming. Many resources are being invested to accomplish this important objective and transport electrification represents one of the necessary steps. Air transportation is seeing an important growth of more electric aircraft (MEA) research and adoption, which aims at increasing the number of electric components through the replacement of pneumatic, hydraulic and mechanical actuators with lighter and more efficient electric systems [1], [2]. On the other hand, long range air transportation is expected to proceed with traditional fuel engine propulsion systems for the upcoming years and it is not easily predictable when the technological gap for an electric propulsion will be closed.

Transportation electrification is recognized as a key strategy to address pollution, particularly as traction motor in the automotive industry. The main motivations behind this trend are zero tailpipe emissions enabled by electric vehicles (EVs), higher energy efficiency of electric powertrains than conventional ones, and the elevated price of refined fuels. In this context, there is a growing demand for electric motors with increased power density, often achieved by increasing the operating rotational speeds. However, together with the structural challenges, power losses at high speed operation are a limiting factor and, thus, a primary design objective lies in efficiently dissipating the heat generated within the electrical machine.

2.2. Overview of electrical power generators in aircraft

Electrical power generation on aircraft was first introduced during World War I, allowing for on-board starting systems and wireless telegraphy [3]. Wind generators, preferred over batteries for their reliability, served as the primary power source. Between the two world wars, additional electrical systems, such as lighting, signalling, and heating, were introduced, increasing power generation capacity from *250 W* to *1000 W* [4]. This growth necessitated a transition from a *6 VDC* to a *12 VDC* electrical system. As aircraft speeds increased, drag caused by wind generators became problematic. Consequently, they were replaced by engine-driven generators. During World War II, engine-driven generators underwent significant advances, achieving better power-to-weight ratios and greater reliability, although DC generation remained standard [5]. The continued increase in electrical power demands, driven by multiple onboard systems, led to higher voltage levels to reduce current, thereby minimizing conductor size and weight. The standard voltage level evolved to *28 VDC*, with DC generators remaining prevalent until about 1950. After World War II, aircraft power systems moved to AC generation, marking a significant transition in technology. Figure 2.1 illustrates the evolution of aircraft power generators from 1950 to the present.

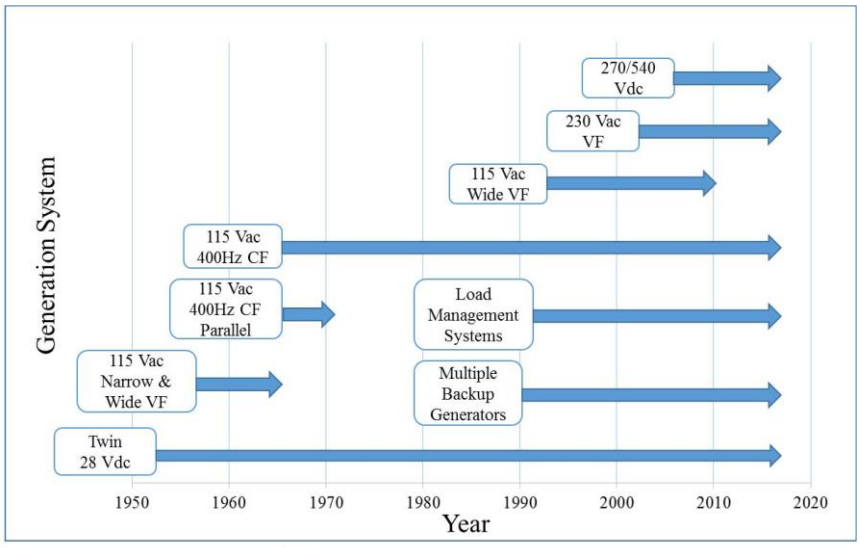

CF: Constant Frequency; VF: Variable Frequency

Figure 2.1 - Electric generation system evolution [10]

Modern DC generators are now primarily used in small aircraft for both primary and standby power generation systems. Examples of civil aircraft employing 28 VDC starter generators include the ATR-600, Dornier 328, Gulfstream G280, and Falcon 2000 [4]. However, modern medium and large aircraft have moved away from DC generators due to the significant advantages offered by AC systems at higher power levels. AC generation allows higher voltage levels to be achieved easily and efficiently using simple transformers, allowing for reduced current for the same output power. This results in smaller conductor size and weight, aligning with one of the primary goals in aircraft design: minimizing mass and volume. Additionally, AC circuit breakers are lighter, more compact, more reliable, and less expensive than their DC counterparts. AC generators themselves are also smaller and lighter than equivalent DC generators, further supporting weight and space constraints in aviation. Reliability is another critical factor that drives the preference for AC systems. AC machines, without the brush-commutator system, offer longer life and lower maintenance costs than DC machines [6].

The wound-field synchronous generator is the most widely used type in modern aircraft. Its popularity stems from its ability to directly and precisely control the rotor field, allowing flexible management of the excitation. This feature not only ensures operational efficiency, but also provides a high degree of safety by allowing immediate removal of the excitation when necessary. Typically, the generator system comprises three key components, as illustrated in Figure 2.2.

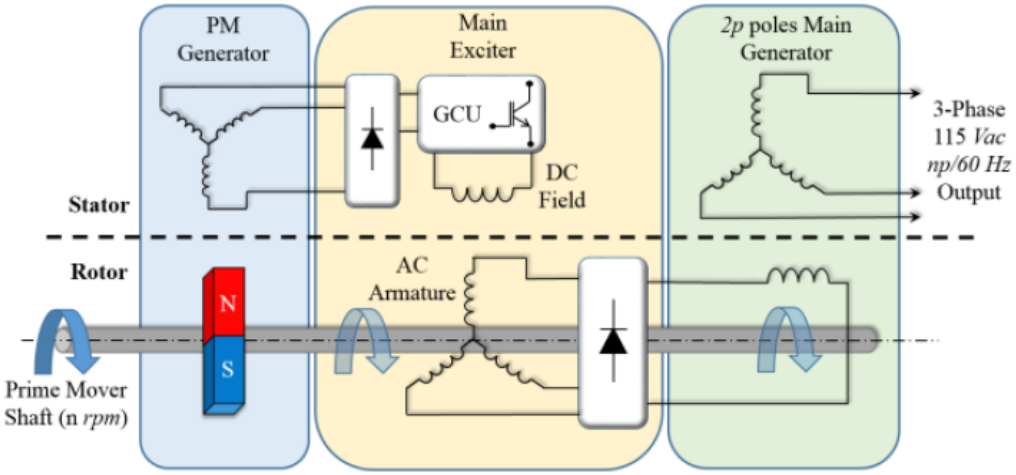

Figure 2.2 - Architecture of the three-stage wound-field synchronous generator [10]

The first stage of the system consists of a classical permanent magnet (PM) synchronous machine, characterized by a PM rotor and a three-phase stator winding. The three-phase voltages induced in this stage are rectified and used to energize the stationary DC field of the second stage, the main exciter, via an electronic control system. The main exciter is essentially a wound-field synchronous machine but with an inverted configuration: the DC excitation winding is placed on the outer stator, while the three-phase armature winding is placed on the inner rotor. The induced rotor voltages are rectified using a rotating diode bridge connected directly to the rotor. The rectified voltage then feeds the generator's main field winding, which resides on the rotor, while the three-phase armature winding is placed on the stator. The generator control unit regulates the amplitude of the main excitation, ensuring correct operation. The AC voltage output frequency depends on the number of pole pairs in the primary generator and the mechanical rotational speed of the primary drive shaft (Ω). Typically, the primary motor is the main engine, whose speed varies from 0 rpm to its rated value. This variability results in a non-constant AC voltage frequency, which is unacceptable for certain electrical loads. One solution to this problem is to integrate the generator stages with a variable-ratio drive gearbox, creating a single unit known as an integrated drive generator (IDG), as shown in Figure 2.3a. The gearbox converts the variable speed of the primary motor to a constant speed, providing a stable AC frequency. However, the gearbox adds weight and size to the system and requires regular maintenance [4]. An alternative approach eliminates the gearbox by using power electronic converters as interfaces to the three-phase armature winding of the main generator (Figure 2.3b). This configuration can use configurations such as a diode rectifier coupled with an inverter or AC/AC converter, producing a constant frequency AC output without the need for mechanical speed regulation. Although effective, power electronics introduce critical reliability issues to the entire system. A hybrid solution combines these approaches: frequency-insensitive loads are powered directly from the variable frequency generator, while frequency-sensitive loads are supplied via power electronic converters (Figure 2.3c). This method balances system complexity, weight, and reliability considerations [7].

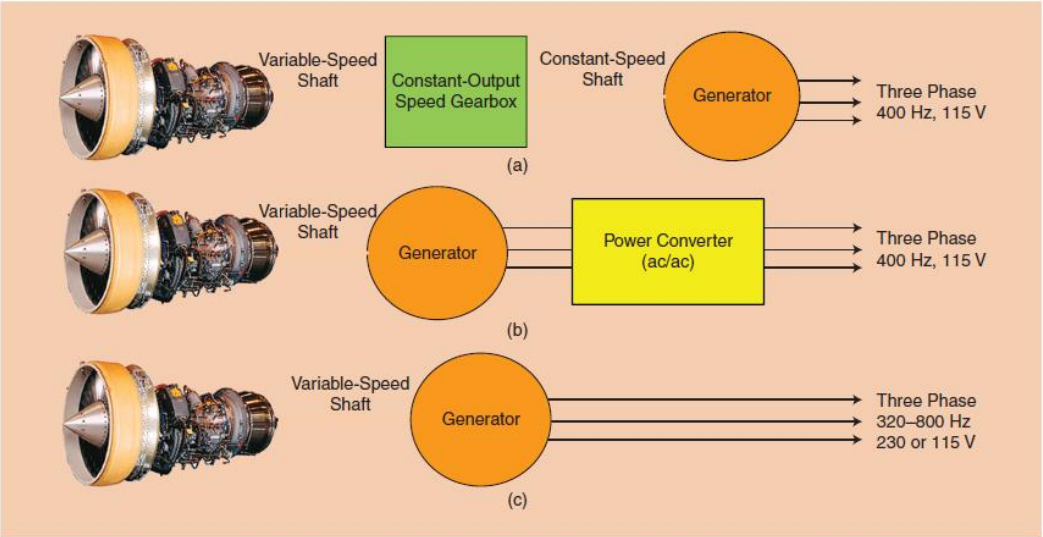

Figure 2.3 - Three methods to interface the main generator with the prime mover and with the rest of the electrical system [8]

Studies have been made regarding machine technologies used in aircraft embracing the MEA trend, including induction machines, PM synchronous machines and switched reluctance machines. The main design aim is to increase the power density, reliability and efficiency. PM synchronous machines have the highest power density compared to other topologies and good efficiency, but their cost is high due to the price of PMs and the power electronics needed to control them. Furthermore, they are sensitive to the critical environmental conditions typical of aerospace applications and have medium reliability and fault tolerance capability. In fact, the excitation of the PMs cannot be removed immediately in the event of a winding fault, this means that the PMs energize the fault until the machine is turned off or the fault is removed. Induction machines, on the other hand, have a good fault tolerance but lower power density. Switched reluctance machines also do not achieve the same power densities as PM synchronous machines, but they can operate in harsh environments due to the robustness of the rotor. Finally, they have also an inherent fault tolerance [9].

2.3. Challenges for WFSGs achieving state-of-the-art performance

The power density of the most advanced wound field synchronous generators (WFSG) recorded, such as the one developed by Honeywell [10], rivals that of PM and switched reluctance (SR) generators when evaluated as stand-alone components. Although very little information is available on how Honeywell´s state-of-the-art generator is achieved, it is very clear that, to obtain an overall power density of *7.9 kW/kg*, then all the aspects of the WFSG must be pushed beyond the standard boundaries. This requires a full understanding of each individual component in a WFSG from electromagnetic, thermal, and mechanical aspects. Finally, challenges arising from electromagnetic, thermal, and mechanical aspects are identified.

A. Background for WFSGs

Figure 2.4 illustrates a representative rotor structure of a WFSG. In the aviation industry, WFSGs face significant challenges, mainly related to thermal management [11],[12] and mechanical reliability [13]. Furthermore, aerospace applications require a high power-to-weight ratio, which requires advances beyond the limits of conventional machines. These improvements typically focus on material optimization [14], cooling enhancements [15],[16], and refinement of structural mechanical design and analysis [13].

Figure 2.4 - Rotor structure of a typical WFSG

B. Thermal challenges for WFSGs implemented for variable speed systems

Efficient cooling strategies play a crucial role in reducing the weight of WFSGs [17]. However, implementing effective cooling systems on the rotor is particularly challenging due to two primary heat sources: the rotor field winding and the damper cage. The field winding generates the excitation field for the main alternator and its losses manifest as heat. For WFSGs used in variable speed systems, electrical frequencies typically range from *360* to *800 Hz*, leading to higher-order harmonics in the air gap. These harmonics induce high-frequency currents in the damper cage, contributing to additional heat generation. In the example shown in Fig. 2.4, the damper cage is integrated into the rotor interpole spaces and slots. Furthermore, the high frequency magnetic field causes significant losses and temperature increases in the magnetic core and stator windings [18]. The most common cooling solutions for aircraft systems include forced air cooling and oil cooling. Oil-cooled generators are preferable in the constant speed-constant frequency system since oil circuits are already available within the mechanical gearbox or integrated drive generators. However, variable frequency generators face a significant challenge due to the lack of existing oil cooling units. As a result, additional cooling circuits, pumps, and meters must be integrated directly into the WFSG, increasing the weight and complexity of the overall system. Additionally, as noted in [19], when shared lubricating oil is used as a cooling agent, the cooling oil may not be available to the generator during certain flight mission cycles. This creates a critical design challenge for variable frequency systems, requiring a delicate balance between maximizing power density and minimizing the complexity and weight of both the generator and its ancillary components.

C. Mechanical challenges for WFSGs implemented for variable speed systems

WFSGs typically operate at speeds between *10* and *25 krpm*. At such high speeds and power levels, the rotor surfaces experience significant peripheral forces, which can cause mechanical fatigue or damage. In addition to speed and size, a key mechanical challenge arises from the design of the field winding, which is wrapped around salient poles, as shown in Fig. 2.4. These pole tips not only perform

electromagnetic functions, but also serve as structural supports to resist the centrifugal forces generated by the field windings. As a result, the rotor bore and pole tips often experience high levels of mechanical stress [20]. Another design challenge concerns the damper cage, located on the rotor pole surfaces, as shown in Fig. 2.4. Hollow structures on the rotor poles, created to accommodate the damper cage, can weaken the structural integrity of the rotor, especially during high-speed operation. Thermal expansion of the damper rods can exacerbate this problem. Furthermore, mechanical vibrations and centrifugal forces require additional structural reinforcements for the field windings, such as retaining rings for the end windings [21], [22], also depicted in Fig. 2.4. The highest mechanical stress (τ_{mech}) on the rotor core can be approximately calculated using equation (1), where C is a parameter related to Poisson's ratio, ρ is the mass density of the core material, r is the radius of the machine and Ω represents the angular velocity.

$$\tau_{mech} = C\rho r^2 \Omega^2 \quad (1)$$

2.4. Overview of electric motor in automotive application

The transition to EVs will continue in the upcoming years, and this will push the research to increasingly focus on improving electric and hybrid powertrains. In a driving cycle, a traction motor must operate in regions of constant-torque and constant-power as shown in Fig. 2.5.

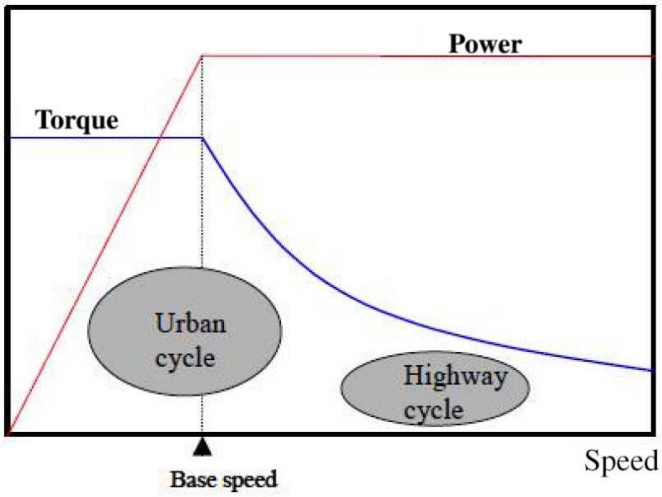

Figure 2.5 - Typical power and torque characteristics of a traction motor

An ideal traction motor for EV and HEV must offer exceptional performance and efficiency. It requires high torque at low speeds to enable smooth acceleration and starting, along with substantial power output to support high-speed cruising. In addition, the motor should maintain high efficiency over a wide range of speeds and torque levels to optimize energy consumption and reduce emissions in the powertrain. To cope with various driving conditions, the motor must offer a wide speed range at constant power and possess the ability to handle short-term overloads [23]. In addition to its performance attributes, it must meet critical customer expectations, including reliable operation under all conditions, compact and lightweight design to improve vehicle efficiency, quiet and smooth operation for a better driving experience, and seamless transitions between internal combustion engine and electric modes in hybrid systems. Economics is also equally important, including low initial costs, low operating expenses, minimal maintenance, and

convenient servicing [24]. By meeting these requirements, a traction motor can play a critical role in improving the performance, efficiency and appeal of electric and hybrid vehicles.

Automakers employ a variety of motor topologies to meet the performance and efficiency demands of electric vehicles. Among them, internal permanent magnet (IPM) motors are a popular choice due to their high torque and power density, which continue to be refined for even greater performance [25]. They also offer high efficiency and excellent flux weakening capabilities. However, achieving these advantages often requires the use of rare earth PM materials, such as neodymium-iron-boron (NdFeB) and samarium-cobalt (SmCo). These materials are subject to price fluctuations and raise concerns about their environmental sustainability and mining practices. To address these issues, ferrite-based magnets represent a more sustainable and cost-effective alternative, but their performance is significantly lower than rare earth PMs. Another promising direction is motor designs that eliminate the use of PMs entirely. The main alternatives in this category include induction motors (IM), synchronous reluctance motors (SRM), and WFSM.

IMs have been widely adopted due to their affordability and robust construction. However, they are hampered by low power factor, limited efficiency, and a narrow constant-power speed range. Synchronous reluctance motors, on the other hand, are highly efficient, capable of operating at high speeds, and offer a wide flux-weakening range. They are also cost-effective and environmentally friendly since they do not rely on PMs. Despite these advantages, their output torque, generated solely via magnetic reluctance, is relatively low compared to IPMs and IMs. Additionally, SRMs typically exhibit a low power factor, which can be improved by incorporating rare-earth or rare-earth-free PMs into their flux barriers [28]. These alternative motor topologies provide viable solutions to the challenges of traditional IPM designs, offering opportunities to balance performance, cost, and sustainability in the development of advanced propulsion systems for electric vehicles.

WFSMs are currently used by major automotive manufacturers such as Renault and BMW. These motors are an established technology in power generation, commonly

deployed in grid-connected [29] and standby/emergency systems [30]. They are also the primary choice for starter generators in aircraft [31] and marine applications [32]. While their use as traction motors in automotive applications is still being explored, it is expected to be a key area of interest in future research. Although WFSMs may not match the torque density and efficiency of IPM motors, they offer significant advantages such as inherent fault tolerance, reliability, high controllability, relatively low cost, and sustainability, making them suitable for the automotive industry. However, unlike other motor types, WFSMs require an excitation system to power the field winding, which adds complexity [32]-[34]. A comparative analysis presented in [35] summarizes the performance of four main radial flux motor options, as shown in Figure 2.6. The study evaluates torque density, efficiency, sustainability, cost-effectiveness and reliability. The results indicate that WFSMs offer a balanced solution, positioned as a promising option in terms of performance and trade-offs (represented by the orange line).

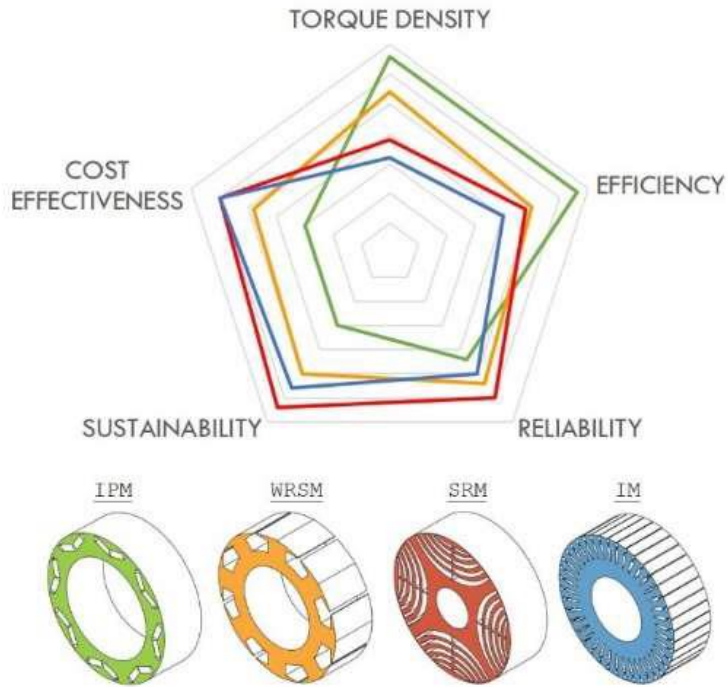

Figure 2.6 - Qualitative performance comparison among 4 radial flux traction machines: IPM (green), WFSM (orange), SRM (red) and IM (blue)

2.5. WFSMs for automotive applications

As mentioned in the above section, Renault and BMW implement a WFSM on board. The Renault´s has a basic configuration of 48 slots and 4 poles, and they have already updated the design for a 36 slots – 8 poles machine of *160 kW*, as shown in figure 2.7. The vehicles that implement this motor span from cars to commercial vehicles. The BMW IX3 motor has *210 kW* of peak power and *400 Nm* of peak torque. Considering the above, it is clear that the WFSM can cover the performance request of different car segments, from small cars to Sports Utility Vehicles (SUV).

Figure 2.7 - WFSM adopted in new Renault Megane E-TECH

Feasibility studies on WFSMs for automotive propulsion have been conducted and compared to IPM machines in [36] and [37]. In [36], the comparison focuses on a non-optimized design, using the same stator as the Toyota Prius—a 48-slot, 8-pole configuration—while evaluating an IPM rotor against a cylindrical WF rotor. The study primarily highlights the feasibility of WFSMs for automotive drive applications. Another comparison is presented in [38], involving a *100 kW* motor with the same 48-slot, 8-pole design. Here, the IPM motor is air-cooled, while the WFSM is oil-cooled. Both motors share the same stator and rotor diameters, though the WFSM has a slightly longer axial length. This study reveals that IPMs

demonstrate higher efficiency in the high-torque, low-speed region, whereas WFSMs excel in the low-torque, high-speed region. This difference can be attributed to the field coil in the WFSM, which enables higher speeds through field current regulation. Figure 2.8 illustrates a 2D angular sector representing one pole pitch for both the compared IPM and WFSM designs.

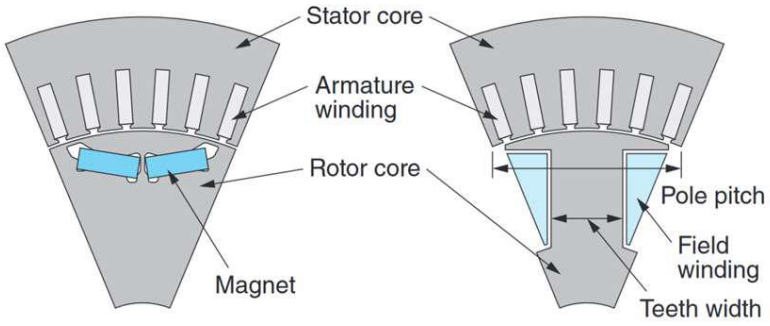

Figure 2.8 - 2D cross section of the IPM motor (left) and WFSM (right) compared in [38]

A more detailed comparison is presented in [37], which builds upon the findings of [36] by using the same IPM motor and maintaining identical dimensions for the WFSM. This study incorporates rotor optimization, and FE simulations demonstrate that WFSMs are strong contenders for EV applications due to their wide torque-speed characteristics and superior efficiency under low-load conditions in high-speed or field-weakening regions. As with [33], [37] emphasizes the potential of WFSMs as traction motors. However, one of the key challenges for WFSMs in the automotive industry is their lower power and torque density compared to PM motors. To address this, [39] proposes a hybrid PM and excited field winding WFSM design that combines reluctance torque with field torque for optimal performance. Meanwhile, [40] focuses on increasing output torque by enhancing the saliency ratio through optimized design. Torque ripple, another drawback of WFSMs, is addressed in [41] and [42], where asymmetric pole shapes and rotor slits are introduced, respectively, as effective solutions. To further improve torque and power density as well as energy efficiency, [43] employs hairpin conductors in the armature winding. The motor, optimized for the New European Drive Cycle (NEDC) [45], is a *120 kW* WFSM with a maximum speed of *10.000 rpm*. The optimized design achieves an 8.5% increase in power density

and a 0.7% improvement in energy efficiency compared to the prototype described in the same article. Hairpin windings were selected for their superior fill factor, while the dimensions of the field conductors were designed to be smaller than the copper skin depth at the frequencies caused by slotting effects and armature reaction. Cooling systems are critical for all motor types, and for WFSMs, the rotor is particularly challenging to cool effectively. The rotor, a key factor limiting power density, experiences high temperatures due to DC current in the field windings [46]. In light of this, [47] compares the designs of salient pole and cylindrical WFSM rotors, concluding that cylindrical rotors offer mechanical advantages over their salient counterparts.

2.6. Future developments: Challenges and Proposed solutions

The electromagnetic design of WFSMs is well established, but its integration with other critical aspects such as thermal management, mechanical design, materials, power electronics (especially in terms of excitation methods), automation, and manufacturing still requires substantial investigation in the coming years. To improve power and torque density as well as efficiency, significant research efforts are expected to focus on rotor thermal management [48]. One of the main challenges in this area is heat extraction from the rotating rotor, which complicates effective cooling. Additionally, higher operating speeds and frequencies can cause higher surface losses, exacerbating thermal challenges. To address this issue, low-loss ferromagnetic materials and insulating materials with high thermal conductivity can be useful [49]. Furthermore, using pre-formed wires for the field winding can improve the fill factor, reducing the insulating material and improving the thermal conductivity inside the gaps. In terms of cooling, a dedicated rotor cooling system is essential, with techniques such as forced ventilation, hollow shafts, and optimized slot thermal paths, all compatible with high rotational speeds. Oil spray cooling, a widely used and effective method to extract armature winding losses in automotive applications, appears promising. However, extracting field winding losses through cooling will still require in-depth research in the coming years. Although materials are critical to improve electromagnetic performance and reduce losses, they also play a critical role from a structural perspective, especially in WFSMs. These motors experience high peripheral speeds on the rotor surface, which leads to mechanical fatigue. The field windings, wound on the salient poles, not only perform an electromagnetic function, but also act as mechanical structures to resist centrifugal forces. As a result, the rotor bores, pole tips, and end plates experience significant mechanical stress due to the forces generated by the field windings. Therefore, advanced containment structures are needed to push these machines to their operational limits. High yield strength materials, such as Vacodur S Plus or JNEX900, can help address the structural challenges inherent in WFSMs. In terms of excitation methods, significant research is already exploring alternatives

to traditional brushed or brushless systems. Both inductive and capacitive wireless power transfer (WPT) systems have demonstrated effectiveness, but challenges remain in integrating these systems into an “exciter-less” machine while reducing manufacturing costs. One approach to integration involves embedding the WPT system within the fan and its housing, as demonstrated in preliminary studies [51]. In the context of high-volume automotive manufacturing, cost reduction is closely linked to the automation of manufacturing processes. The use of pre-formed conductors for field windings and hairpin windings for the stator are effective strategies for this purpose. Another potential avenue to reduce manufacturing costs is the development of solid rotor structures, potentially using large laminations with radial and/or axial grooves, which could help minimize iron losses. New materials and, more significantly, advanced manufacturing techniques, such as additive manufacturing, have the potential to enable innovative designs, making this one of the key emerging topics in the field. While the electromagnetic design of WFSMs is well established, as previously mentioned, insights from advances in the design of traditional machines for other applications suggest that there is still room for improvement. For example, pole shaping has been shown to effectively reduce torque ripple [53], and incorporating damping systems could serve the same purpose [18]. However, these strategies need to be carefully evaluated, taking into account the additional thermal, structural, and manufacturing challenges they may introduce. Furthermore, hybrid-excited machines are believed to hold promise for automotive applications, offering increased torque density when combined with advanced rotor cooling solutions, all while avoiding the use of rare-earth permanent magnets. Table I provides a summary of the challenges and potential solutions for WFSMs in automotive applications.

TABLE I: CHALLENGES AND PROPOSED SOLUTIONS

Wound Field Synchronous Motors	
Challenge	**Solution**
Thermal management, heat extraction from the rotor	Advanced rotor cooling, e.g. dedicated fan, slot heat paths, hollow shaft, etc.
Increase operating speeds and frequencies	Improved materials, solid rotors, sophisticated analysis tools
Structural Integrity	End plates of non-electric steel, retaining structures for windings and pole tips
Exciterless solutions	Wireless power transfers (WPT) system integrated within the fan and its housing
Cost reduction	Preformed conductors for stator and rotor windings, solid rotor
Improved Electromagnetic Design	Pole shaping, damping systems, axial and radial grooves

2.7. Multi-physics design and optimization of electrical machines

Electric machines are crucial components in various applications requiring high power, torque, and efficiency in compact dimensions, including the power generation, automotive, and aerospace industries [54]. These industries require products that are not only high-performance, but also reliable, cost-effective, and environmentally friendly. Given these requirements, electric machine design is a multidisciplinary challenge that integrates several interconnected subdisciplines, including electromagnetics, thermal management, and mechanical design. Consequently, the development of a new electric machine involves a comprehensive approach, balancing performance, cost, manufacturability, and lifetime, while optimizing the interaction between electromagnetic, thermal, and mechanical aspects. To achieve this, an in-depth understanding of a specific application is vital to inform the design process, also called "design for application". A realistic multiphysics design process for electrical machines involves continuous iterations between electromagnetic, thermal, and structural design, supported by theoretical analyses, numerical simulations, and experimental tests [55]–[59]. Traditionally, the design process has focused primarily on electromagnetic considerations, with thermal and structural evaluations conducted separately afterwards. To prevent failures, especially in high-power, high-torque, or high-speed applications, engineers often apply empirical constraints based on experience and fundamental physical principles during the electromagnetic design phase. For example, thermal design aspects are sometimes addressed by imposing limits on the current density in the coils, the magnetic flux density in the cores, or other sizing parameters. However, these approaches may not have sufficient accuracy and may not ensure a fully optimized and reliable machine design. Numerous methodologies have been developed and presented to accurately predict the design performance of electrical machines and avoid prototyping time and costs. In general, these computation methods can be divided into two approaches:

1. Classical analytical analysis

2. Numerical techniques

Analytical analysis is based on fundamental physical theories, such as Maxwell's equations and heat transfer principles. However, applying these theories to complex geometries is often challenging. Numerical methods for solving these problems can be categorized into integral equations, typically solved using the boundary element method, and differential equations, which are addressed using finite difference and finite element methods (FEM). Among these, FEM is the most widely used approach to tackling complex engineering problems. However, it tends to have a relatively high computational time. A simpler alternative is the lumped parameter model, which represents the machine as an electrical circuit with linear and nonlinear elements. This model calculates the potentials of the nodes and the current flow through the branches. While increasing the number of elements increases the accuracy, solving nonlinear circuits also increases the computation time. The main differences between these methods lie in their mathematical formulations and solution techniques, which require a balance between accuracy, complexity, and computational efficiency. Furthermore, the properties of the materials used in electrical machines play a crucial role in the design process, although the characteristics of the materials can be said to be the main reason for a multiphysics design.

A. Challenges and opportunities in multiphysics design and modelling

An electric machine is a sophisticated electromechanical system composed of various components, including electromagnetic elements (rotor, stator, and excitation), cooling systems, housings, and mechanical parts such as shafts and bearings. These components collectively form the machine. There are two main approaches that can be used to design electric machines: 1) component-based design and 2) system-based design. In the component-based approach, each part is designed and optimized independently. In contrast, the system-based design approach involves an iterative process where the design and optimization of the entire machine is performed considering the interactions between all components. While the component-based methodology is simple and straightforward, it may not produce the optimal design of the overall system. In other words, optimizing

individual components does not necessarily result in the best configuration for the entire system. On the other hand, a system-based design, although more complex and time-consuming, ensures an optimized overall solution. It is important to note that the computation time is highly dependent on the methodology used to design and model each component.

B. Electromagnetic Design

The working principle of electrical machines is established on the electromagnetic theory. The electromagnetic design of electrical machines is the core of multiphysics design and it is derived from magnetic field calculation which allows the machine parameters to be calculated.

1. Electromagnetic sizing

The design process for electrical machines typically begins with the definition of key parameters and characteristics. These include the machine type (e.g., asynchronous, synchronous, or reluctance), structural configuration (e.g., axial or radial flux, internal or external rotor, single or multistage, round or salient poles), and key performance specifications such as rated torque, power, speed, number of poles, and voltage. Additionally, critical electromagnetic parameters, such as electrical load, stator slot current density, and air gap flux density, must be determined. These values are selected based on the machine's structural design and cooling system. With these key design inputs established, rotor and stator geometries can be calculated and optimized using guidelines such as Essen's rules [55]–[58].

2. Magnetic materials

Material selection, including hard and soft magnetic, conductive and insulating materials, plays a vital role in the electromagnetic design of electrical machines. Soft magnetic materials are classified into grain-oriented and non-oriented electrical steels. Non-oriented steels exhibit uniform magnetic properties in all directions, but have limitations in terms of saturation flux density and magnetic permeability. These materials are widely used in rotating electrical machines, with silicon-iron, amorphous alloys, nickel-iron and cobalt-iron being prominent examples. Among them, silicon-iron is the most popular, accounting for about 80%

of the market, due to its affordability despite its lower saturation level compared to other alloys. Grain-oriented steels, on the other hand, possess optimum magnetic properties along the rolling direction, making them suitable for transformer applications [60], [61]. Soft magnetic composites (SMCs), composed of pure iron powder particles coated with insulating films, offer high electrical resistivity and low eddy current losses. Their powder-based structure enables the design of complex machine geometries such as axial flux, transverse flux, and hook-pole machines. Emerging materials such as two-phase [62] and multilayered magnetic composites [63], [64] show promise, although further research is needed to assess their applicability. Hard magnetic materials, also known as permanent magnets, are valuable for their ability to maintain magnetization without a continuous energy input. These materials are integral to numerous applications due to their resilience against external fields and self-demagnetization. Common options include alnico, hard ferrite, SmCo, NdFeB, and bonded magnets. NdFeB, characterized by its high remanence flux and coercive field, together with SmCo, represent the most advanced and expensive solutions. Conductive materials, mainly copper and aluminum, are essential for windings and bars in stator and rotor components. Superconducting tapes, which exhibit near-zero resistivity at extremely low temperatures (e.g., -196 °C with liquid nitrogen cooling), represent an advanced alternative for specialized applications. Insulating materials, such as PEEK, serve to separate the conductive elements from the magnetic core, preventing short circuits and ensuring mechanical stability. Commonly used insulating materials include polyamide-imide, polyester, glass-mica tape, mica paper, and epoxy glass [65], [66]. These materials not only provide electrical insulation, but also contribute to thermal management, as effective heat dissipation is critical in high-performance electrical machines.

3. Winding design

Windings in electrical machines serve various purposes and are classified into categories such as armature windings, rotating field windings, field or magnetizing windings, damping windings, commutation windings, and compensation windings [55]–[57]. Armature windings, in particular, are commonly implemented in three configurations: lumped, distributed, and ring (or core-wound) forms. Among these,

distributed windings are the most widely used despite their longer end windings and higher copper volume. This is because they offer superior performance by reducing the harmonic content in the air gap magnetomotive force waveform, improving machine efficiency, and minimizing losses. In contrast, ring windings are less common due to the complexity of their construction. The winding fill factor, defined as the ratio of the copper cross-sectional area to the gap area, is a critical parameter in the design of windings and stators. In conventional machines, this factor is relatively low, ranging from 0.25 to 0.5, mainly due to the round shape of conventional wires. Recently, there has been increasing interest in using rectangular conductors, such as foil and hairpin windings, to improve the fill factor. These advanced winding techniques can achieve higher packing density, resulting in reduced resistive losses, improved thermal management, and improved overall machine performance [67], [68].

C. Thermal design

The main aim of thermal design is to evaluate the heat distribution in the electric machine structure. The heat is generated by power losses, and it has a great impact on the machine performance since the insulation materials degraded by increasing the temperature. Furthermore, the magnetic and mechanical properties of materials are temperature dependent. Usually, the cooling system type is chosen at the beginning of the design procedure on the basis of the selected application.

1. Thermal management considerations

Thermal management is a complex but crucial aspect in electric machine design. Inefficient cooling system leads to faster insulation degradation and increased winding failure rates due to increased thermal cycles [69]. The internal heating within an electrical machine is the result of generated losses and the temperature distribution is governed by the balance between generated heat, removed heat and thermal capacity [70]. The heat can be extracted through conduction, convection (natural and forced) and radiation. The thermal management of electrical machines is an inherently 3D feature which requires complex heat extraction phenomena to be addressed; e.g., heat transfer through complex composite components such as the wound slot, temperature drops across interfaces between components and

complex turbulent air flow within the end-caps [71]. Thus, the analysis of heat transfer and fluid flow is complex due to the high non-linearity of the phenomena which may occur. Non-thermally conductive materials such as winding insulations may also result in local heat concentration. Therefore, effective thermal management improves electric machine performance and ensures reliable machine operation, while poor thermal management results in performance degradation, accelerated machine wear, and even may cause machine breakdown. Different thermal management requirements are necessary for different types of electric machine applications. In general, the rotor assembly of an electrical machine is very challenging in terms of effective heat removal. This is due to nature of the rotary part with a limited thermal path for extracting the generated heat. In a thermal

Figure 2.9 - Thermal management of electrical machines

management system design, the thermal class of the coils generally define the maximum operating temperature of the machine. To enhance thermal management in electric machines, it is essential to resolve challenges from all aspects including the heat sources, the heat dissipation paths, and the heat removal sinks, as shown in Fig. 2.9 [72].

2. Working temperature of electrical machine

The performance and longevity of insulation materials in electrical machines are highly sensitive to operating temperatures. According to IEEE Standard 117, insulation systems are classified into separate thermal classes based on their maximum allowable temperature: Class A (105 °C), B (130 °C), F (155 °C), H (180 °C), N (200 °C), and S (220 °C) [73]. Electrical machines are typically designed to operate below the upper limits of their assigned insulation class to ensure reliability and durability.

The insulation system plays a critical role in determining the life of the machine. Excessive operating temperatures can have a negative impact, significantly reducing the useful life of the machine. This effect is well illustrated by a principle derived from the Arrhenius equation: for every 10 °C increase in operating temperature above the thermal classification of the insulation, the useful life of the insulation is approximately halved. This paper highlights the critical importance of effective thermal management in the design of electrical machines to prevent overheating and extend their operating life.

3. Thermal properties of magnetic materials

The operating temperature of an electrical machine has a significant impact on the properties of magnetic, conductive, and insulating materials, influencing performance and efficiency. For magnetic materials, temperature changes affect critical characteristics such as saturation point, hysteresis, and eddy current losses. In low-carbon steels and low-silicon laminations, the saturation knee decreases by about 10% with increasing temperatures, which reduces the anisotropy energy depending on the material [61]. However, total core losses decrease due to an increase in electrical resistivity, a nearly linear trend observed in the range from 20 °C to 200 °C [74]. Non-oriented silicon steel shows a higher sensitivity to temperature changes in iron losses than grain-oriented types [61]. At cryogenic temperatures, the knee point of the B-H curve and the magnetic permeability of the lamination materials increase. However, beyond a certain low temperature threshold, the permeability begins to decrease, even below room temperature levels [61], [74], [75]. Similarly, hard magnetic materials, such as permanent magnets, are

highly temperature dependent. Elevated temperatures reduce their residual flux density, while cryogenic conditions increase the residual flux density by up to 20% [76]. Temperature also has profound effects on the conductive and insulating properties of materials. Cryogenic conditions increase conductivity but can degrade insulation reliability. Furthermore, mechanical properties of materials, including stiffness and Young's modulus, are significantly affected by temperature changes, which can affect the structural integrity and mechanical performance of machine components [77]. These multifaceted temperature dependencies highlight the importance of precise thermal management in the design and operation of electrical machines.

4. Power loss

There are different power losses in electrical machines. These losses are the main source of generated heat in the machine structure. In general, the loss components can be divided into electromagnetic loss such as copper and iron core losses and mechanical loss. The electromagnetic losses are mainly generated in the active part of the machine including rotor, stator, and excitations [78]. Some of these loss components are production technologies dependent, such as the loss increases due to the welding or punching of the laminations [79]. The copper loss results from Joule heating due to the resistivity of the conductors. Copper loss usually is a major loss component in all electric machines, especially at high torque operation. The copper loss increases as the resistance increases with the temperature. The second major loss in electric machines is iron loss. These are caused by the time-varying magnetic field that yields hysteresis and eddy current losses. It is typically dominant when a machine operates at higher frequency, i.e. at high speed. Hysteresis and eddy current losses are the main iron loss components. The hysteresis loss is caused by a time-varying magnetic field primarily in major loops. Eddy current loss is caused by the current induced in the core. In addition, frequency dependent skin and proximity effects add to the overall copper losses. The skin effect is caused by eddy currents induced by a conductor’s own flux linkage. Skin effect increases with frequency and effectively reduces the cross-sectional area of the conductor, thereby increasing its resistance. Mechanical loss in electric machines consists of friction and windage losses. Friction losses are mainly caused by the bearings and are

thermally relevant. The resulting heat and the heat passing to the ambient via bearing increase the local temperature. The aerodynamic drag experienced by rotor periphery and cooling fan causes windage loss. These losses can be minimised using high quality bearings, lubricants and high-performance fan designs.

5. Cooling techniques

The cooling systems of electrical machines can be categorized into passive cooling and active / forced cooling depending on the heat transfer mode or generated cooling flows. Passive cooling techniques denote systems without a fan or pump and feature lower power loss. Passive cooling methods work based on natural convection and radiation to dissipate the generated heat from the machine to the environment. The cost of passive cooling and its noise emission are typically very low. However, this technique is usually adopted for small size and low power/density machines. Fig. 2.10 summarizes various cooling methods in electrical machine application.

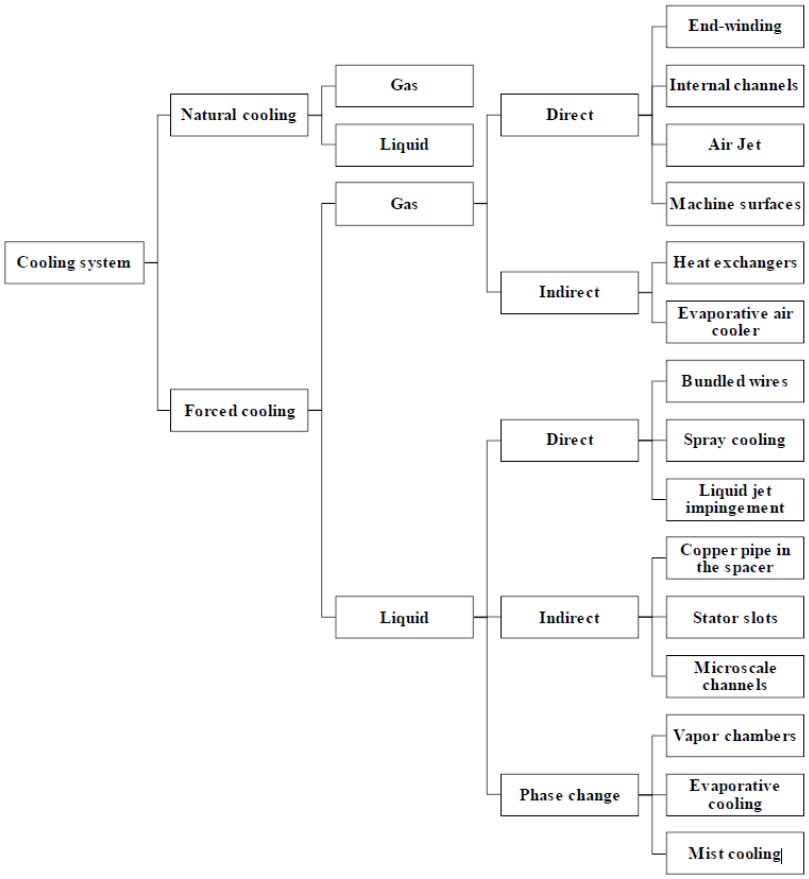

Figure 2.10 - Different cooling system used in electrical machines

Considering fin or heatsink on the outer part of stator or machine frame is one of the most common solution to enhance convection heat exchange. Forced cooling techniques feature an active mechanism for circulating the fluid, either gas or liquid, in different parts of the machine structure. This technique is well-known and widely used in a large number of applications like automotive and aerospace industry. Force cooling can be as simple as using a fan enclosed in the machine structure or it can be much more complicated system for liquid channels.

Water jacket cooling is a commonly-used indirect cooling technique, it is mainly used to cool the stator. The advantages of using water jacket include higher power-to-frame size ratio, lower noise level, higher efficiency and completely enclosed environment. The removed heat is not directly dissipated into the environment. Different configurations of water jacket channels and frame structures have been exploited including helical ducts, circumferential channels, meander shape of ducts, and axial serpentine channels, as shown in Fig. 2.11.

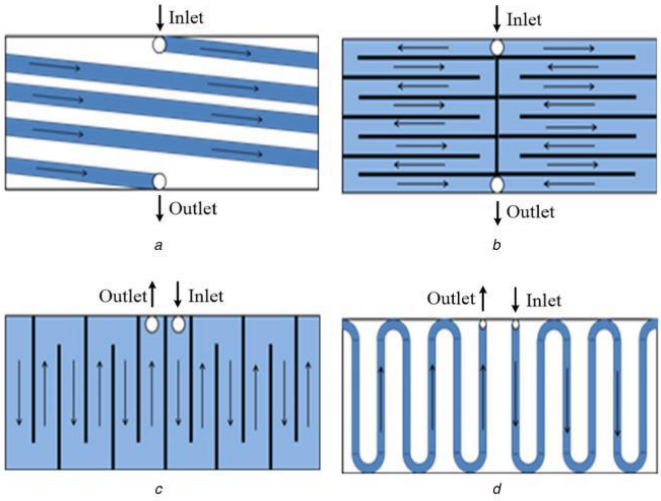

Figure 2.11 - Various water jacket cooling configurations and paths; a) Helical channels, b) Circumferential channels, c) Meander axial channels, d) Axial serpentine channels

The configuration and the number of cooling paths determine the cooling efficiency as well as the pressure drop from the inlet to the outlet. Figure 2.12 shows a typical example of external liquid cooling.

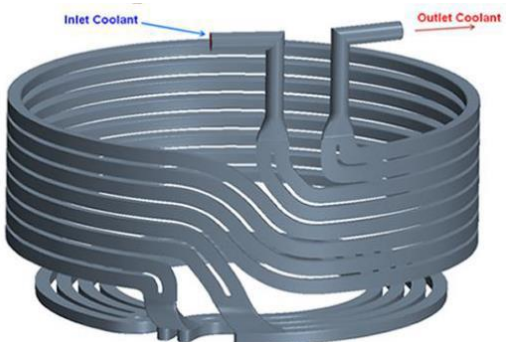

Figure 2.12 - Water jacket cooling

Disadvantages of using water jacket for cooling include higher manufacturing cost, requirement for an auxiliary system to provide coolant, risk of corrosion inside the water circuit, risk of leaks, and more precautions with maintenance. Direct stator core cooling applies where water jacket cooling is not sufficient and a significant temperature gradient might exist between the outer stator surface and the inner stator core. As illustrated in Figure 2.13, traditional cooling techniques alone, such as cooling jackets [81], [82] or air cooling [83], [84], are not sufficient to handle the thermal demands of high power density EV motors [80]. Consequently, it becomes necessary to combine conventional cooling methods with more advanced indirect or direct cooling systems to ensure effective heat dissipation from the stator windings and rotor components.

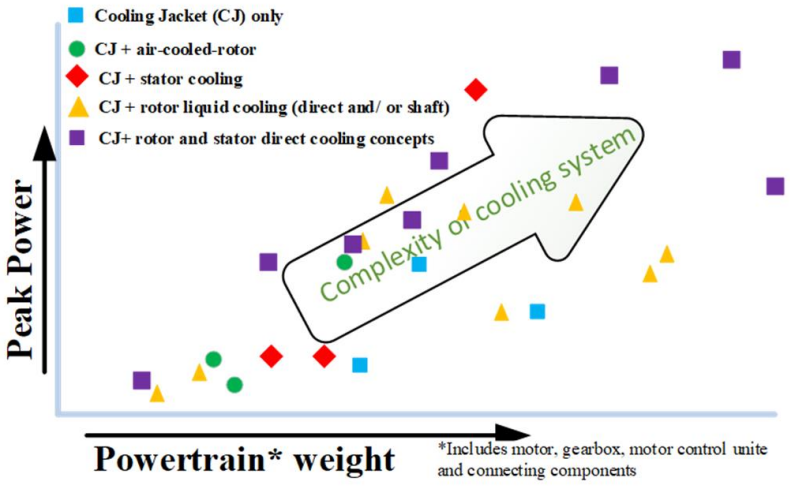

Figure 2.13 - Variation of the thermal management system of EV motors by increasing their peak power [80]

Another important area that often requires improved cooling in electric machines is the end winding. Cooling methods for the end winding include spray cooling, liquid jets, and the use of thermally conductive materials between the end windings and the machine frame. For new generation EV motors, conventional cooling methods such as housing liquid jackets are being supplemented with advanced indirect or direct cooling systems (Fig. 2.14). These systems include techniques such as stator slot cooling [85]-[89], stator core cooling [88], [89]-[92], end winding cooling [93]-[95], [11],[17], and rotor cooling [48],[96], [88], [97]-[99] to ensure effective cooling of critical machine components.

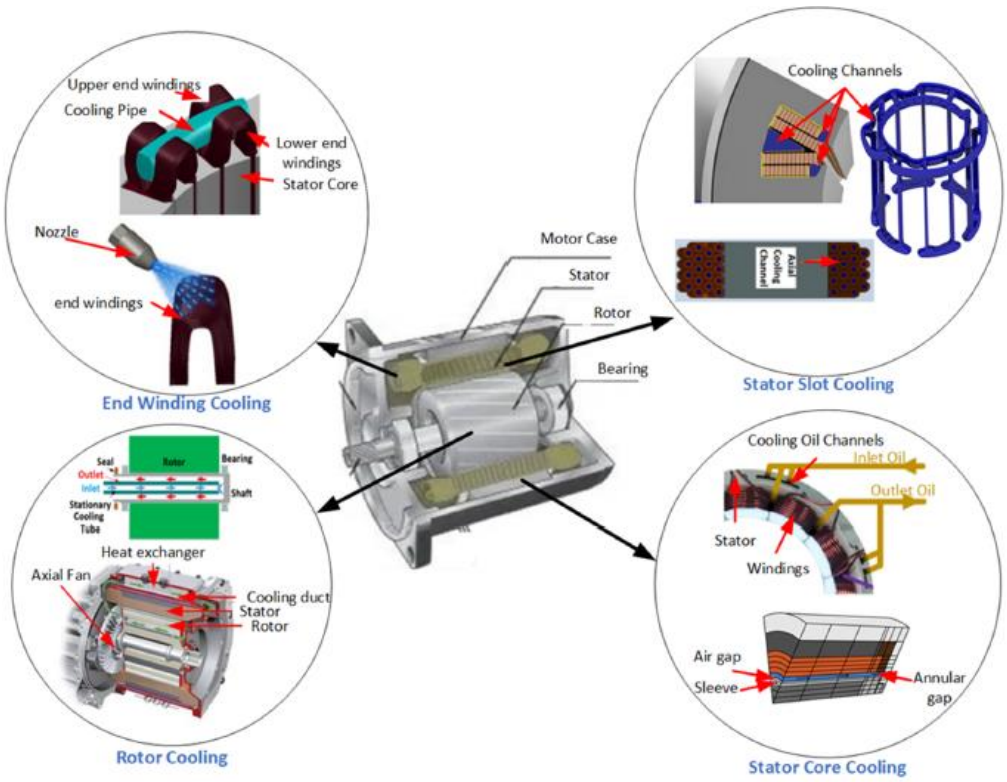

Figure 2.14 - Various cooling concepts for EV motors [96]

Another thermal management approach focuses on improving heat dissipation from the rotor. In motors with an internal rotor design, the air gap acts as a thermal insulator, significantly impeding heat transfer from the rotor [96]. As a result, the rotor tends to reach its temperature threshold earlier [97]. Since direct rotor cooling in an EV motor is a challenging task [96], an indirect shaft cooling system is

proposed as a solution. In this system, the crankshaft is equipped with concentric tubes through which a coolant (such as oil or water) circulates. This technique is commonly used in electric vehicles with induction motors, such as the Tesla Model S [100] and the Audi e-tron [101]. This cooling approach improves motor performance and rotor cooling can be integrated with the stator cooling system, as illustrated in Fig. 2.15. However, in practice, this solution is complex and may increase the axial length of the motor.

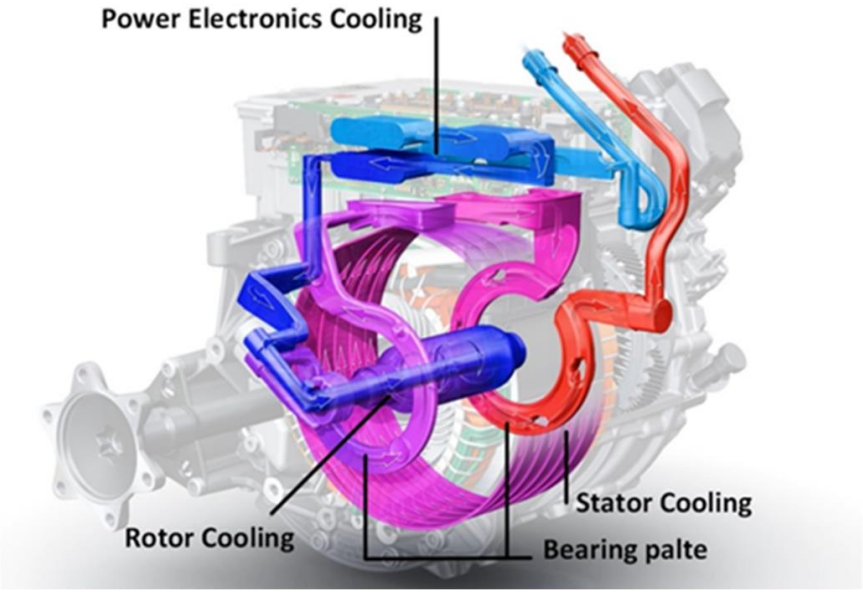

Figure 2.15 - Integrated rotor and stator cooling systems [101]

Spray cooling in electrical machines is an emerging technique, although spray cooling itself is not a new concept. Numerous research studies have explored this approach [102], [103]-[105]. The method involves a complex heat transfer mechanism, with most of the results derived from experimental studies. As illustrated in Fig. 2.16, research efforts to implement oil cooling systems in electrical machines can be classified into two main groups: evaporative spray cooling and lubricating oil spray cooling. Furthermore, lubricating oil spray cooling is further divided based on the motor winding configuration: one for stranded-winding motors and another for hairpin-winding motors. Furthermore, stranded-winding configurations are classified into two additional subcategories based on the nozzle placement.

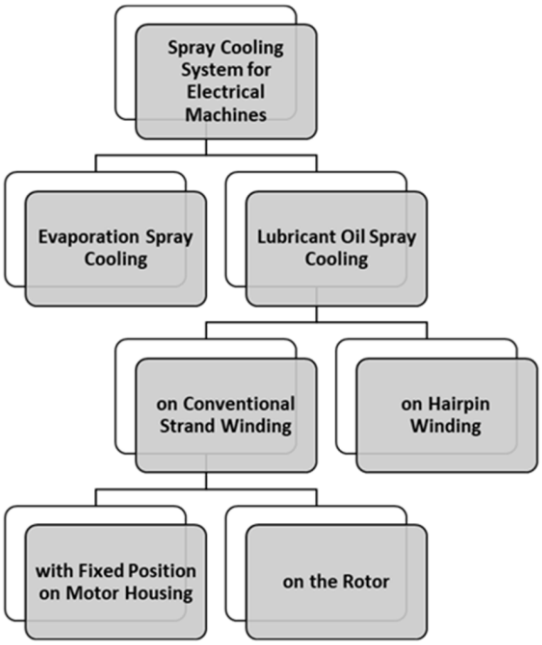

Figure 2.16 - The attempt and research on implementing of oil cooling system for electrical machines [106]

The use of spray cooling in electric machines was first explored in 2009 by Li Zhenguo et al. [107], who applied an evaporative spray cooling method to a large synchronous generator. Traditionally, such generators are cooled using a wet stator technique, where the stator is immersed in coolant. However, this method has the disadvantage of requiring a significant amount of coolant. To address this problem, spray cooling systems were introduced for the active parts and end regions of the stator, significantly reducing the amount of coolant required. Compared with the semi-flood cooling method, spray cooling offers better cooling efficiency, smaller coolant inventory, and more uniform temperature distribution. EV motors are compact and installed in tiny places. Therefore, there is no adequate space for installing extra devices such as pre-heat, extra pumps, condenser, and reservoir for evaporation coolant. Furthermore, the cooling system's primary objective is to use the available fluid as a coolant; for example, in EV motors, the coolant can be air, water, and oil. As a result, the lubricant oil with a more straightforward thermal management system, including one loop, becomes suitable for EV motors. However, the non-uniformity of oil film distribution on end-windings during high rotor speed becomes more significant, leading to uneven temperature distribution

on the end-windings. The main drawback of the uneven temperature distribution is the occurrence of unexpected hot spots in the system.

6. Thermal modelling

An important aspect of thermal management in electrical machines is the ability to predict the temperature distribution during the design phase using thermal analysis methods [108]. These methods are divided into analytical and numerical approaches.

For analytical analysis, the most commonly used method is the lumped parameter thermal network (LPTN), which provides a fast way to determine the temperature distribution in electrical machines. It allows users to quickly evaluate the effects of varying input parameters. Components can be grouped into different submodels, either radially in a 2D cross-section of the machine or in a 3D representation that considers the effects of axial heat distribution. LPTN models can predict steady-state or transient heat flows within the machine, as well as estimate the temperatures of individual components. However, a disadvantage of the LPTN method is the significant effort required to develop an accurate model [109]. LPTN models differ between machines based on specific rotor and stator configurations, which introduce fundamental variations and result in distinct thermal network paths during model development.

For numerical modelling, there are proven methods to predict temperatures within electrical machines with high accuracy compared to experimental results. The two most widely used techniques are finite element analysis (FEA) and CFD. Although these methods can provide highly accurate temperature predictions with minimal error, they are typically more time consuming due to their complexity and the need for detailed input data. As a result, each thermal analysis approach has its strengths and limitations. FEA involves dividing the machine geometry into a finely interwoven grid of nodes and elements to evaluate temperature variations between those elements. Many commercially available software tools can perform 2D or 3D thermal FEA for both steady-state and transient simulations. Thermal FEA results are generally comparable to LPTN models when similar inputs are applied. However, FEA becomes advantageous for geometries that are too complex to be

modelled using LPTN. To reduce computational time, FEA models are often simplified to partial or fractional representations of the full geometry by applying periodic patterns. FEA accuracy improves with finer mesh details, but this comes at the expense of increased computational time. CFD is generally the most accurate method for temperature prediction, outperforming both LPTN and FEA, especially in scenarios involving fluid flow and heat transfer. CFD can be used to determine heat transfer boundary conditions for LPTN and FEA models and can simulate fluid flow characteristics to optimize cooling systems (e.g., water jackets or air cooling) [110]. Various CFD thermal analyses of varying levels of complexity have been used to simulate the airflow around machine components, including the stator-rotor air gap, end windings, and cooling passages. CFD excels in cases where simultaneous airflow, mass transfer, and a combination of laminar and turbulent states need to be considered, or when designing coolant flow channels and patterns [110]. Similar to FEA, CFD requires the input of material properties and boundary conditions, such as fluid volume flow rate, inlet temperature, and pressure [111], [110]. Modern CFD tools are mainly based on the finite volume method, solving the Navier-Stokes equations with validated physical models to achieve high accuracy for 3D laminar or turbulent flow and heat transfer simulations [109]. However, the main limitation of CFD is its long simulation time, which depends on the complexity of the geometry, mesh refinement and available computing power. Simplifying the geometry while maintaining solution accuracy is a significant challenge in CFD, limiting the user's ability to quickly assess the thermal distribution impact of changes to design input parameters.

D. Mechanical design

The mechanical design process is crucial for assessing the structural integrity of the geometry derived from the electromagnetic design. In high-speed applications, where stresses and vibrations are significantly elevated, ensuring mechanical integrity becomes paramount to prevent potential failures. The primary objective is to confirm that the geometry can withstand the mechanical loads and stresses encountered during operation, including centrifugal forces, thermal expansion, and vibrational impacts. This involves not only evaluating the material strength and fatigue resistance but also optimizing the design to mitigate stress concentrations and ensure long-term durability and reliability under demanding conditions.

1. Stress analysis of rotor

Traction motors operate at very high speeds (> 10 krpm). At these speeds, the centrifugal forces play a dominant role when considering the mechanical design issues. Stress analysis is essential for evaluating the ability of a machine's structure or components to withstand various loads without failure, thereby ensuring optimal performance of electric machines. A key design parameter that significantly influences the mechanical behaviour of the rotor is the length-to-diameter ratio ($\lambda = L/D$). A smaller λ value results in higher centrifugal forces at the rotor surface and increased tangential speed. These centrifugal forces induce stresses in both the circumferential and radial directions, which must be carefully analysed, particularly at the shoes of a salient pole rotor. It's important to note that stress not only affects the structural integrity but also impacts the magnetic properties of materials, leading to an increase in hysteresis loss due to the elevated coercivity under stress [112].

2. Fatigue models and analysis

Due to the typical cyclic loading experienced in electrical machines, progressive and localized structural damage can initiate on a microscopic scale, often starting with microcracks. These microcracks can rapidly propagate, leading to significant macroscopic cracks. Over time, this degradation can culminate in material failure at stress levels well below the material's yield tensile strength or even ultimate tensile strength. This phenomenon, known as fatigue, is particularly concerning because it can lead to unexpected and catastrophic failures in machine components,

emphasizing the need for rigorous fatigue monitoring and material selection to mitigate such risks. Fatigue of a structure defines the service life of a component and it is dependent on several factors, including material, manufacturing process, operating environment, and the design. Traction motor drives are expected to deliver superior performance throughout the lifetime of a vehicle. Thus, the durability and reliability requirements (determined by fatigue life estimates) are critical factors in customer satisfaction. Fatigue analysis helps in predicting the life of the system under different drive duty cycles and severe loading conditions.

Common fatigue failure models include the S-N (stress-life) curve, fracture mechanics, and energy dissipation models. The S-N curve is the most traditional and widely used approach to predict the fatigue life of materials under specific stress levels [113]. Although it is simple and intuitive, its predictive accuracy is limited under complex stress conditions, especially when applied to composite materials and nonlinear fatigue behaviour. The fracture mechanics model, which predicts fatigue failure by analysing crack initiation and propagation [114], is particularly useful for materials susceptible to microcrack formation, such as metals and some piezoelectric ceramics. It can accurately predict crack growth rates, although its application to complex material systems requires further research. The energy dissipation model, which examines the energy dissipated by materials under cyclic loading, is suitable for polymers and composites [115]. This model captures nonlinear fatigue behaviour and provides more flexible predictions, as energy dissipation is related to the accumulation of internal damage within the material. The analysis of the fatigue mechanism focuses mainly on how microstructural changes in materials influence their macroscopic fatigue behaviour. Fatigue crack initiation typically occurs at the material surface or in regions of stress concentration, with crack propagation significantly influenced by the fracture toughness of the material and external environmental factors [116]. Understanding the crack propagation rate and path is critical to predicting fatigue failure. Under cyclic loading, the material microstructure, such as grain boundaries, dislocations, and pores, often undergoes significant changes that directly influence fatigue life [117]. This effect is particularly pronounced in nanomaterials and composites, where microstructural changes have a greater impact on fatigue performance.

Environmental factors, such as temperature, humidity, and exposure to chemical media, can accelerate the fatigue damage process. These factors accelerate material aging, corrosion, and crack propagation, which can significantly reduce the fatigue life of components. Therefore, a comprehensive understanding of these fatigue mechanisms is essential to optimize the design of electrical machines and improve their operational life.

3. Mechanical modelling

Given the nonlinear nature of the problem, the most effective method for evaluating the structural integrity of the rotor is through FE modelling. A 2D FE model is used to assess the rotor geometry at its maximum operational speed, ensuring that the design can withstand the associated stresses. However, to capture the full complexity of the system, a 3D FE model is necessary to account for the impact of end-windings on the rotor tips of a WFSM. The rotor tips are particularly critical because they bear the load of the cantilevered mass of the end-windings, making them highly susceptible to stress concentrations. A key aspect of this modelling process is accurately simulating the contacts between the rotor and winding. Properly modelling these interactions is crucial for achieving precise stress predictions, particularly in the rotor tips, where even minor inaccuracies can lead to significant errors in the evaluation of structural integrity. By carefully considering these factors, the FE model provides a comprehensive assessment, helping to ensure the rotor's reliability and longevity in high-stress environments.

3. CASE OF STUDY 1: Refined Structural Design and Thermal Analyses of a High-Speed Wound-Field Generator for Aerospace Applications

WFSMs are widely used as generators to meet the electrical energy demands of various low-speed applications. They offer several advantages over rare-earth PM counterparts, including ease of control, inherent fault tolerance, lower cost, and the use of more sustainable materials. However, PM machines are generally preferred as generators in aircraft due to their higher power density and efficiency. This preference is further supported by the robust rotor structure of PM machines, which enables reliable operation at relatively high speeds. In contrast, the rotor of a wound-field machine, with its salient poles, is less suitable for high-speed operations.

This chapter investigates the structural and thermal performance of a high-speed wound-field generator designed for aircraft applications. While the electromagnetic aspects of the design have been thoroughly explored in previous work, this study focuses on the structural design and analyses using 2D and 3D finite-element methods, as well as evaluations using CFD.

Structurally, the challenge of managing centrifugal forces on the end-windings was addressed by adding a layer of non-magnetic material to the rotor's periphery. Thermally, the removal of the rotor cage, originally designed as a retaining system, enabled axial airflow, which effectively cooled the rotor. The results indicate that the designed motor is well-suited for the intended application.

3.1. Introduction

The electrification trend which is occurring in all types of transport applications is taking a central role to contrast the climate change and improve the life quality. In this context, the aviation industry is also moving towards the design of aircraft featuring higher efficiency and lower emissions [118]. Traditional actuation systems, such as hydraulic and pneumatic ones, are being replaced by electrical actuators [119]. However, this is determining a huge increase in the total power required by electric loads on board of aircraft. For example, the installed electric power has risen up to about 1 MVA in two of the most significant applications of the MEA concept, i.e. the Boeing 787 (B787) and the Airbus 380 (A380) [120]. According to the MEA trend, the electric generators and related converters are designed to start the main engines up, thus implementing the "starter generator" function that permits to eliminate the pneumatic systems [121]. Presently, the WFSM is the most used type of electric generator on board of aircraft. While the generator system is relatively complex and bulky, it permits to achieve a good fault management capability compared to other machines equipping PMs [122]. In fact, the generator rotor field current can be easily controlled, thus permitting to zero the currents when an internal fault occurs, without the need to halt the rotor. On the other hand, it is rather a common view that wound-field machines are less power dense than other machine types used as on-board generators for MEA applications, such as synchronous PM and reluctance machines [31]. Aiming to overcome the reliability challenges associated to PM machines and to achieve higher power density values than reluctance machines, a high-speed WFSM is proposed for use as generator in an MEA context. The estimated power density of the WFSM designed is *3 kVA/kg* (active parts only), achieved thanks to the relatively high rotational speed being hypothesized (i.e. *15 krpm*). To balance the cost/performance ratio, that study was carried out using common materials and standard cooling solutions, aiming to keep the costs at reasonable levels. A water jacket is adopted to cool the stator and an axial airflow from a fan to cool the rotor. The main focus of the previous work was on the electromagnetic aspects, where a preliminary sizing and a FE refinement were mainly performed. In this chapter is reported a brief

overview on the electromagnetic design. However, starting from the WFSM electromagnetic design, the present chapter focuses on the structural and thermal aspects of the WFSM with detailed 2D and 3D FE mechanical analyses and CFD investigations. The aim of these models is twofold:

1) to design a reliable mechanical solution able to withstand the high speed of the generator while allowing for axial flow on the rotor;
2) to extrapolate an accurate temperature map, allowing to propose further design improvements of the WFSM.

3.2. Electromagnetic Design

The electromagnetic design of the generator was realised through a previous master's thesis work in collaboration with the University of Pisa, Pisa, Italy and the University of Nottingham Ningbo, Ningbo China.

3.2.1 Target of the project

The project focused on leveraging existing knowledge and expertise to design a high-power-density wound-field synchronous generator, which is the most used AC generator in aircraft. The generator under analysis was designed with specifications closely aligned with those of the Boeing 787 (B787) wound-field synchronous generator, particularly regarding mechanical inputs (nominal torque and speed) and electrical outputs (nominal voltage and power). However, the primary objective was to reduce size and weight by utilizing standard materials and cooling systems. The B787, recognized as a leading example of the MEA concept, served as a benchmark. The goal was to design a generator that could be highly competitive in the future aircraft generator market. Achieving a higher power density than the already efficient B787 generator could provide significant benefits, such as reduced fuel consumption and emissions while maintaining the same nominal power or enabling the installation of additional electrical loads without increasing overall weight.

3.2.2 Preliminary Electromagnetic Design

The rated specifications assumed for the design of the aerospace generator are showed in table II.

TABLE II: MAP OF SPECIFICATIONS

Quantity	Notation	Value
Speed	**Ω**	15 000 rpm
Input Torque	T	159 Nm
No. of stator phases	m	3
Power	S	250 kVA
Voltage	V	400 V
Frequency	f	750 Hz
Pole pairs	p	3

In order to minimize the weight of power generation system, it was assumed that the rotor is mechanically driven by a variable-speed shaft and the alternator is interfaced with the rest of the power system by means of a suitable active power convert. Therefore, the damper cage was not included in the design because the power converter takes care of properly controlling the machine operation during transients. A simplified analytical algorithm based on [123] was implemented to achieve a preliminary sizing of the generator. As a starting point, the axial active length was fixed as $L = 245mm$, which derives from reasonable space considerations. Then, the air gap diameter D was determined using (2), where c_d is an empirical coefficient.

$$D = \sqrt{c_d \frac{S}{\Omega L}} \tag{2}$$

Assuming a sinusoidal distribution of the air gap flux density and considering its half-wave average value equal to the reasonable level $B_m = 0.65T$, the magnetic flux per pole was calculated as in (3).

$$\Phi = \frac{B_m D\, L}{p} \tag{3}$$

Concerning the stator winding, aiming to achieve an acceptable quality of the trends of linked fluxes for the armature phases, a double-layer configuration with 3 slots-per-pole-per-phase was initially assumed with a shorted pitch by 1 slot to mitigate some major harmonics without significantly compromising the amplitude of the fundamental. Considering the above, the number of active sides per phase N was then calculated as in 4) assuming Y-connected stator phases:

$$N = \frac{V}{\sqrt{3}\left(k_f k_d k_p\right)\Phi\, f} \tag{4}$$

where k_f, k_d and k_p are respectively the form factor, the distribution factor and the pitch factor. Since the phase current is obtained as $S/\sqrt{3} = 360.8A$, the stator winding was divided into 3 parallel paths, one per each pole pair, to reduce the current flowing in each active side. Assuming a standard external forced air cooling system, a stator current density of $6\ A/mm^2$ was chosen, allowing the conductors and, consequently, the stator slots to be sized. Consistent with the choice to design a machine that is not too expensive, standard fully processed M330-35A non-oriented silicon steel laminations were selected for the rotor and stator cores. For the rotor pole body, the rotor and the stator yokes, an operating flux density of $B_p = B_{sy} = B_{ry} = 1.6T$ was chosen. Finally, magnetic circuit analysis was performed to calculate the excitation magneto-motive-force MMF_{exc} needed to compensate for the magnetic voltage drops in each part of the generator. These drops were then calculated for different values of the output voltage knowing the geometry and the magnetization curve of the ferromagnetic material used, thus allowing to build the open circuit characteristic. Although a salient-pole machine structure was

envisioned from the beginning, a rough estimation of the *MMF* needed for the magnetization of the machine MMF_{exc} when operating with nominal load was obtained using the Potier method to account the *MMF* due to the armature reaction. Since a relatively small machine equipped with common forced-air cooling of the rotor was envisioned, a reasonable rated current density equal *6 A/mm*^{2} was assumed for the field winding, whose corresponding rated voltage at no load was chosen as *60V* assuming again a reasonable typical value. Such data permitted to determine the number of turns and the wire diameter for the field winding. Having completed the preliminary sizing of the generator, its electromagnetic analysis was carried out for verification purposes using the model described in [124]. Implementing the equivalent circuit equations as in [125], the machine inductances and the terminal voltages were determined for different operating conditions. To evaluate the load condition, it was assumed that the power converter draws a symmetrical set of sinusoidal currents in phase with the fundamental harmonic of the corresponding voltages. At full load condition, to keep the output terminal voltage at its rated value, it was necessary to increase the excitation current up to *9.2A.* A summary of the main characteristics obtained from preliminary design is reported in Table III.

TABLE III: MAIN CHARACTERISTICS OF THE INITIAL MACHINE DESIGN

Parameter	Notation	Value
Axial active length	L	245 mm
Rotor diameter	D_r	183 mm
Outer stator diameter	D_{out}	209 mm
Air gap thickness	g	2 mm
Number of slots	Q	54
Number of conductors per slot	n_c	2
Number of excitation turns per pole	N_{exc}	155
No-load excitation voltage	V_{exc}	69 V
No-load excitation current	I_{exc}	7.9 A
Full-load excitation current	I_{out}	9.2 A

3.2.3 Electromagnetic design refinement

Despite its reduced computational burden and accuracy under specific operating conditions [125], the developed analytical model is based on a number of simplifying assumptions, e.g. the linear behaviour of the ferromagnetic materials and the neglecting of leakage fluxes above all. Hence, a FE model of the generator was built in MagNet® software using the geometry resulting from the preliminary design. First, the no-load operation of the machine was evaluated through a 2D transient-with-motion simulation, observing a pretty good waveform quality for the open circuit terminal voltages. However, the rms-value of such voltages was lower than the expected rated value. Therefore, the excitation current was increased (up to 12A) until the rated value of the output voltage was reached at no-load. To compensate for the negative effects deriving from such an action, the geometry was modified to properly adjust the saturation level in the cores and to keep the current density values still compliant with the assumed cooling system. As a result, the stator outer diameter was increased keeping the same yoke thickness, thus resulting in an increase of the rotor diameter. The rotor yoke thickness was decreased while the pole width was increased to limit the magnetic stress. Therefore, the available space to locate the field winding was increased, permitting to keep standard values of current density even with higher excitation currents.

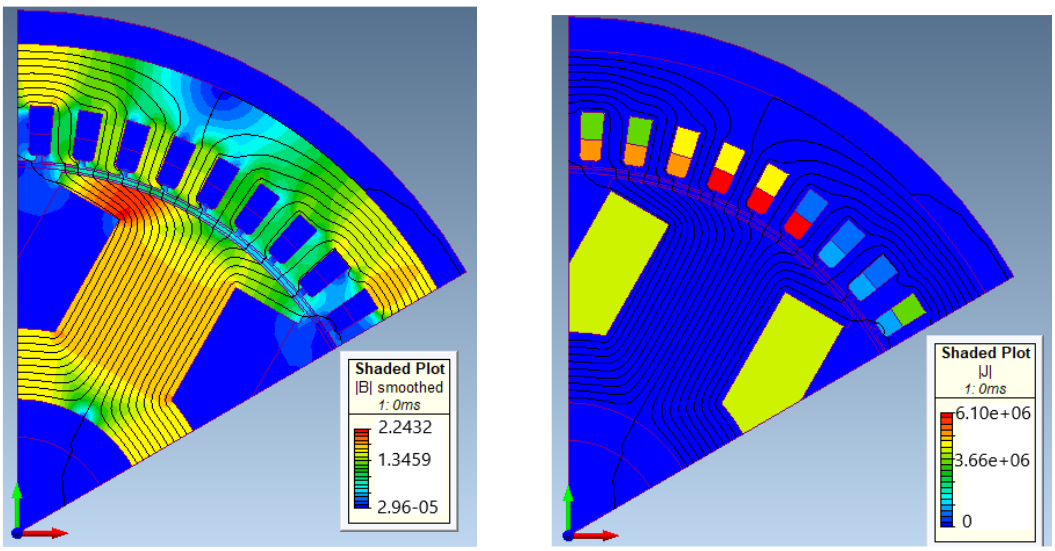

(a) Flux density map (b) Current density map

Figure 3.1 - Flux density and current density maps of the generator at full-load condition

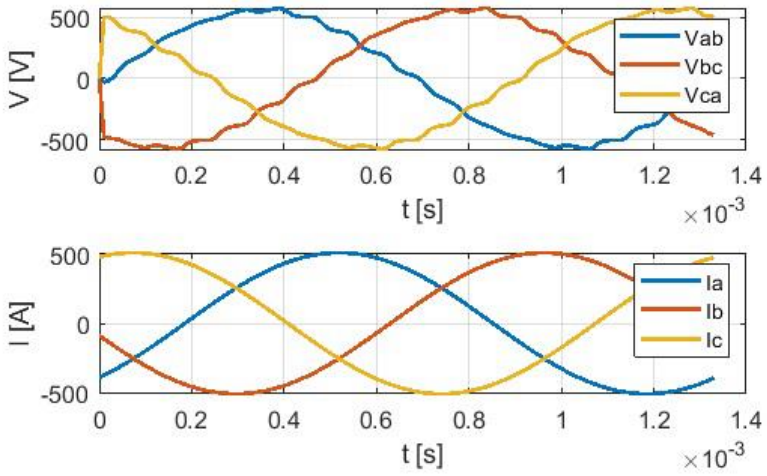

Figure 3.2 - Line-to-line voltages and phase currents at full-load condition

A second significant simulation was then run at rated load conditions. As at nominal load condition the armature reaction produces an overall demagnetization effect, it was found necessary to increase the excitation current up to *13.5A* to provide the nominal terminal voltage. Referring to full-load operative conditions, in Fig. 3.1 the flux density and the current density maps are shown, whereas the waveforms of line-to-line voltages and phase currents are depicted in Figure 3.2. Since Figure 3.1a) shows a peak flux density of *2.2T* in the rotor pole shoes, modifications were made to the inner profile of the rotor pole core to reduce this excessive value. Chamfers were introduced as part of these modifications. Figure 3.3a) illustrates the updated geometry along with the corresponding flux density map at full load. The flux density inside the pole shoe decreases by about *0.2T*, while overall the rotor and stator cores appear properly loaded from a magnetic point of view. As shown in Figure 3.1b), the actual current density values were calculated by considering the assumed slot fill factor of *0.65*. This resulted in current densities of *9.38 A/mm²* for the stator and *6.46 A/mm²* for the rotor. To reduce the stator current density to an appropriate level, the outer diameter of the stator was increased, leading to larger stator slots. This adjustment effectively limited the maximum stator current density to *6.75 A/mm²*, in alignment with the assumed cooling capabilities.

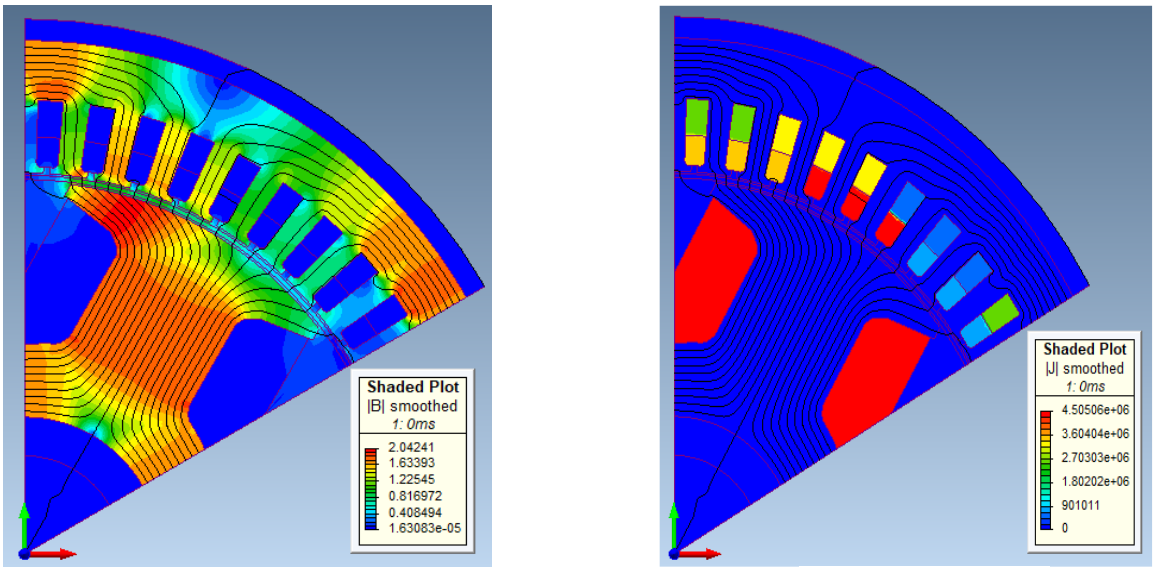

(a) Flux density map (b) Current density map

Figure 3.3 - Flux density and current density maps of the update geometry at full-load condition

The terminal voltages shown in Figure 3.2 determine an rms-value of the fundamental component of *405V* that meets the technical specifications, with an acceptable total harmonic distortion *THD = 4.9%*. The last modification to the preliminary design consisted in increasing the number of turns of the field winding up to *166* per pole, allowing to keep the excitation voltage below *100V*. Hence, the excitation current decreased down to *12.6A* to keep the same MMF_{exc}. The main characteristics of the refined machine are summarized in Table IV.

TABLE IV: MAIN CHARACTERISTICS OF THE REFINED MACHINE

Parameter	Notation	Value
Axial active length	L	245 mm
Rotor diameter	D_r	207 mm
Outer stator diameter	D_{out}	240 mm
Air gap thickness	g	2 mm
Number of slots	Q	54
Number of conductors per slot	n_c	2
Number of excitation turns per pole	N_{exc}	166
No-load excitation voltage	V_{exc}	100 V
No-load excitation current	I_{exc}	11.1 A
Full-load excitation current	D_{out}	12.6 A

3.3. Mechanical Design and Modelling

The selected rated speed of *15 krpm* presents a significant challenge, as the salient pole structure of the rotor is not ideally suited for high peripheral speeds. Therefore, it is crucial to assess the structural integrity of the rotor at this speed. This assessment is performed using both 2D and 3D FE models, with Altair Hypermesh utilised as the pre-processor and MSC MarcMentat as the solver. The primary objective of this chapter is to identify a solution that can withstand the rotor's high rotational speed while also enhancing its cooling. To achieve this, the initial step involves evaluating the geometric layout from the preceding electromagnetic design using a 2D FE model to check the rotor's structural integrity at *15 krpm.* Following this, the stress on the rotor tips due to rotor end-windings is analysed through a 3D FE model. Based on the results from both the 2D and 3D models, observations were made that led to a potential solution: adding a *4 mm* layer to each rotor end-cap to improve structural integrity and cooling efficiency.

3.3.1 2D FE Model – Pre-processing

First, structural simulations have been performed to record the stress of some critical parts of the components at maximum rotational speed of *15 krpm*. An important aspect of the FE model is the definition of the mesh. It is important to consider a trade-off between the computational time and the accuracy of the results. The mesh has been prepared by employing only half rotor pole has been modelled, which corresponds to half pole pitch of the machine, taking advantage of its symmetry. A mesh size of *2 mm* has been adopted employing Quad4 elements (four-node, four Gaussian integration points, isoparametric, bilinear element). The mesh is shown in Fig. 3.4.

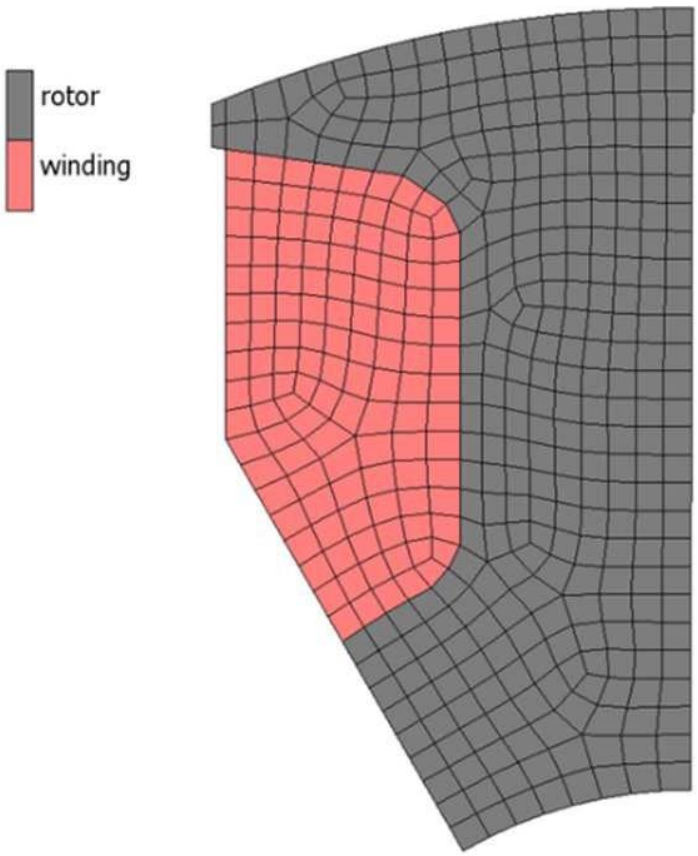

Figure 3.4 - Structural 2D FE model – mesh used

The displacements orthogonal to the symmetry planes and the rotations of the planes are constrained. Table V shows the structural property of the materials adopted.

TABLE V: MATERIAL PROPERTIES

M330-35A		
Density	7650	Kg/m3
Young's modulus	195000	MPa
Poisson ratio	0.3	
Yield strength	365	MPa
Equivalent orthotropic copper		
Density	5980	Kg/m3
Young´s modulus longitudinal	58763	MPa
Young´s modulus transversal	11548.4	MPa
Poisson ratio	0.3	
38NiCrMo4		
Density	7800	Kg/m3
Young´s modulus	210000	MPa
Poisson ratio	0.3	
Yield strength	1020	MPa

Since the rotor winding shows a complicated geometry to be discretised in the FE model, an equivalent solid part has been inserted. In particular, an equivalent density has been computed considering the ratio between the full and the empty parts of the winding. This has permitted to properly take into account the centrifugal load caused by the winding on the rotor. Also, it should have been necessary to calculate the equivalent mechanical properties of the winding. Since it exhibits an orthotropic behaviour, different properties should be applied in the axial direction and in the plane orthogonal to this axis. Since this contribution focuses on the rotor, the mutual interaction between the copper wires of the winding has not been studied in detail. As a result, the stress and strain state of the winding could not be accurately captured. However, the contact area with the rotor and the corresponding load transfer from the windings to the rotor were computed precisely, as shown in Figure 3.5. The contact modelling involved defining the elements at the copper-rotor interface and assigning the appropriate meshed deformed contact interaction type. To simulate the retain force of the winding, a friction coefficient of *0.5* is applied.

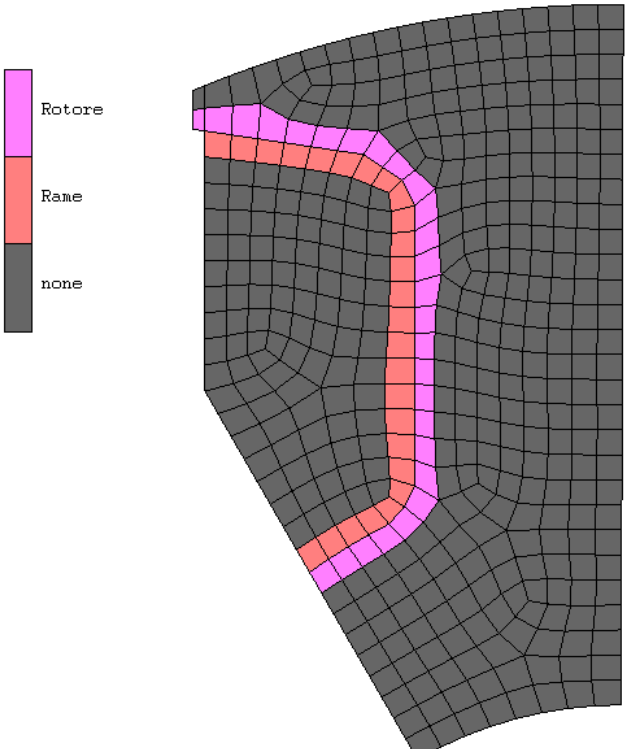

Figure 3.5 - Highlight of the element in contact in the 2D FE model

3.3.2 2D FEM – Results

Two main aspects have to be considered in this analysis. First, the structural integrity of the rotor has been investigated. In particular, the yield stress of the material has been considered as the limit of both the static loadings and of the repeated fatigue cycle that involves the assembly. Secondly, the maximum radial displacement of the periphery should have been less than 2 mm not to jeopardize the function of the machine. Figure 3.6 shows the contour bands map of the von Mises stress of the rotor. The maximum value of von Mises stress is *279 MPa*, lower than the yield stress of *365 MPa* for the steel M330-35A employed. Therefore, no critical issues should be encountered. Figure 4 shows the radial displacement of the rotor. The maximum displacement of the periphery is *0.075 mm*. This value is not negligible and should be properly considered during the definition of the main air-gap. However, with the current airgap thickness of the machine (i.e. 2 mm), no critical challenges should occur.

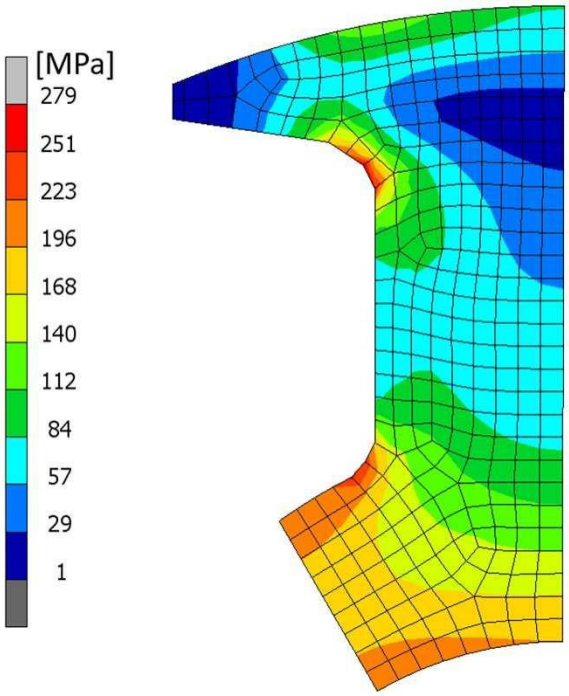

Figure 3.6 - Equivalent von Mises stress contour plot of the rotor

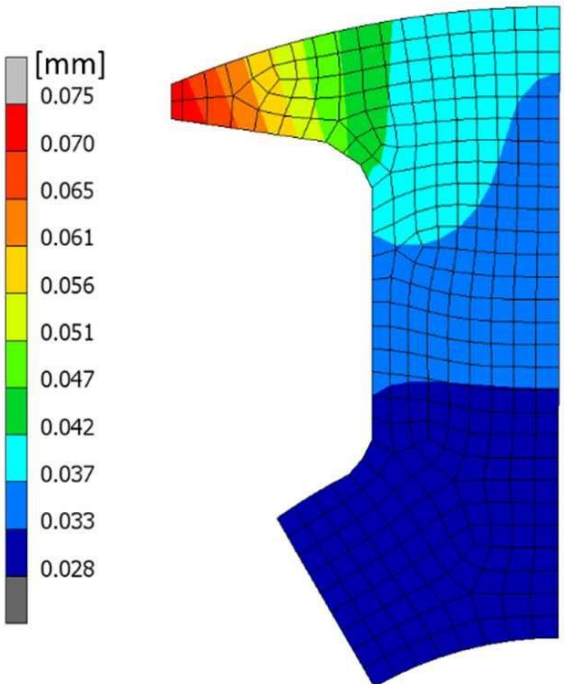

Figure 3.7 - Radial displacement contour plot of the rotor

3.3.3 3D FEM – Pre-processing

Although the 2D model has not shown critical issues, it is necessary to set up a full 3D model to study the stress on the rotor due to end-windings. In fact, the 2D planar model is sufficient to study the behaviour of the assembly far from the extremities but it is not enough to predict the behaviour of the end-windings. The 3D analysis takes into account the real axial geometry of the machine. Figure 3.8 shows the discretised 3D model. The same methodology chosen in the 2D model has been adopted, and one half of the axial extent has been modelled exploiting the transversal symmetry of the WFSM rotor. A mesh size of *2 mm* has been adopted. HEX8 3D elements (eight-node, isoparametric, hexahedral element) have been employed.

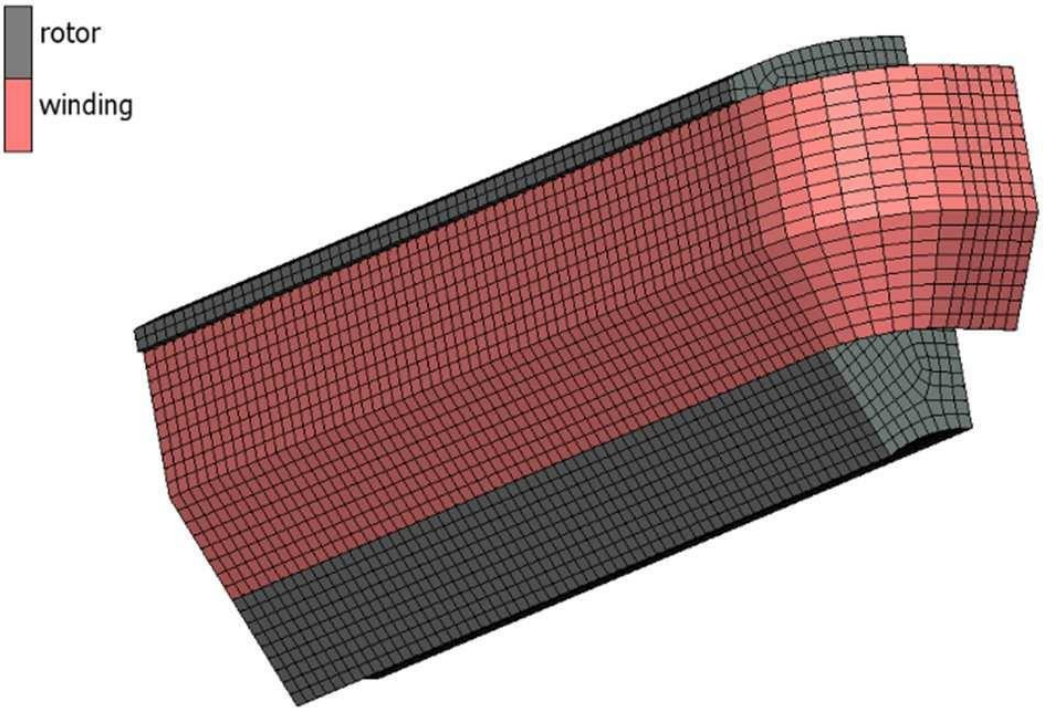

Figure 3.8 - Structural 3D model – mesh used

The contact modelling involves defining the elements at the copper-rotor interface and assigning the appropriate meshed deformed contact interaction type. To simulate the retain force of the winding, a friction coefficient of *0.5* is applied. Figure 3.9 highlights the elements of both the winding and the rotor that are in contact.

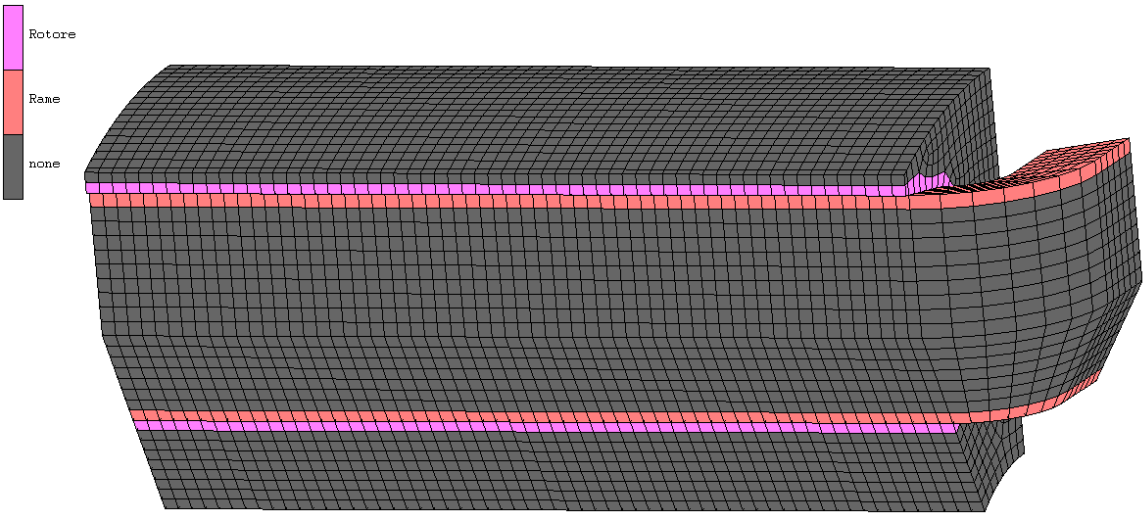

Figure 3.9 - Highlight of the element in contact in the 3D FEM model

3.3.4 3D FEM -Results

The built 3D model has been able to consider the influence of the end-winding. In fact, the end-winding might be considered to be a cantilever mass that loads the extremities of the rotor. Three aspects have to be analysed in detail:

1) the structural integrity of the rotor is considered as done for the planar model;
2) the maximum radial displacement of the rotor periphery should be less than 2 mm not to compromise the operating conditions of the motor;
3) the radial displacement of the end-winding should be also considered.

Figure 3.10 shows the von Mises stress contour plot. A peak value of *653 MPa* is located on the periphery of the rotor in correspondence to the end-winding. Clearly, cantilever mass is not supported by anything and therefore it loads the extremity of the rotor. This stress field is not tolerable and a solution is proposed in the next section.

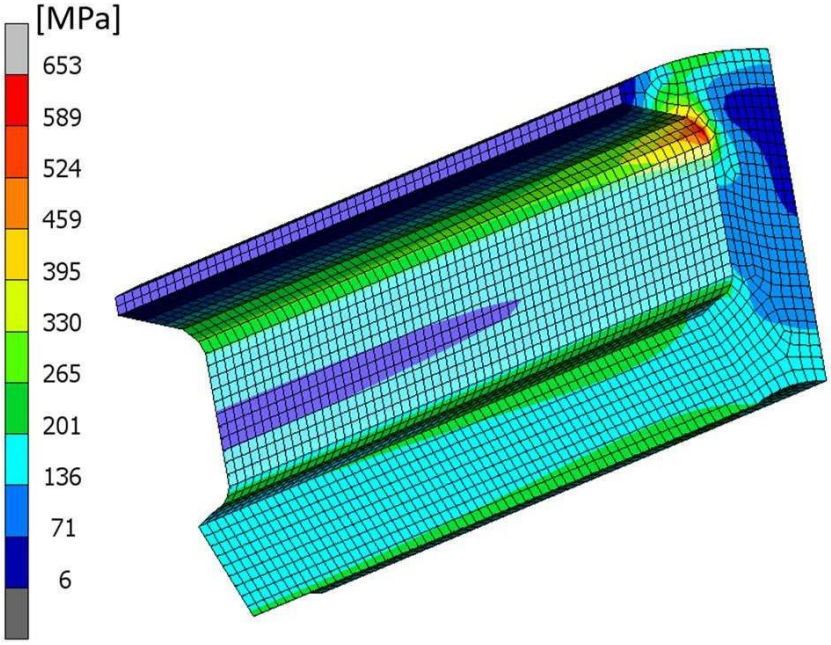

Figure 3.10 - Equivalent von Mises stress contour plot of the rotor

3.3.5 Design refinement

The electrical steel M330-35A, used for the rotor core, exhibits good electromagnetic properties but lacks in mechanical strength. To enhance the mechanical robustness of the rotor, a *4 mm* layer of non-electrical steel, 38NiCrMo4, is added to the periphery, as detailed in Table V and illustrated in Fig. 3.11.

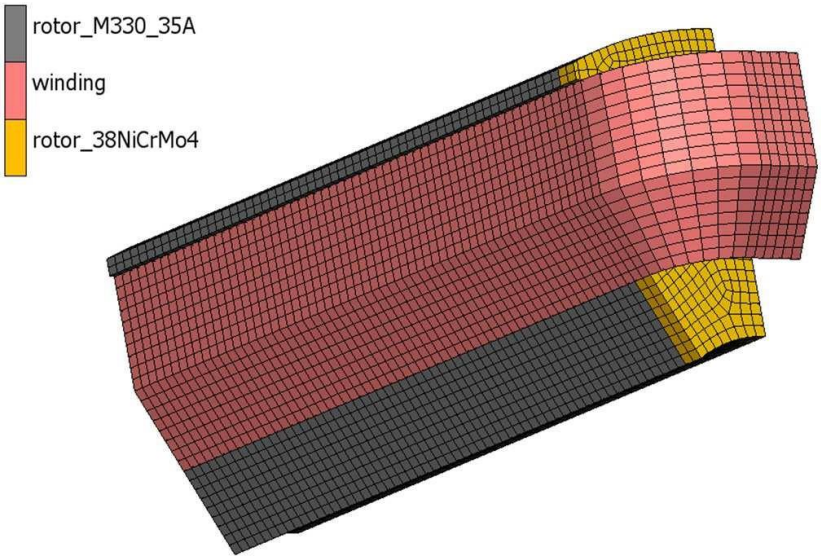

Figure 3.11 - Structural 3D model, improvement design

The von Mises stress distribution, shown in Fig. 3.12, reveals a maximum value of *653 MPa* at the rotor's extremity. Given that the yield stress of 38NiCrMo4 is *1020 MPa*, this stress level is within acceptable limits. The maximum stress observed in the M330-35A electrical steel remains below its yield stress of *365 MPa*, ensuring structural integrity.

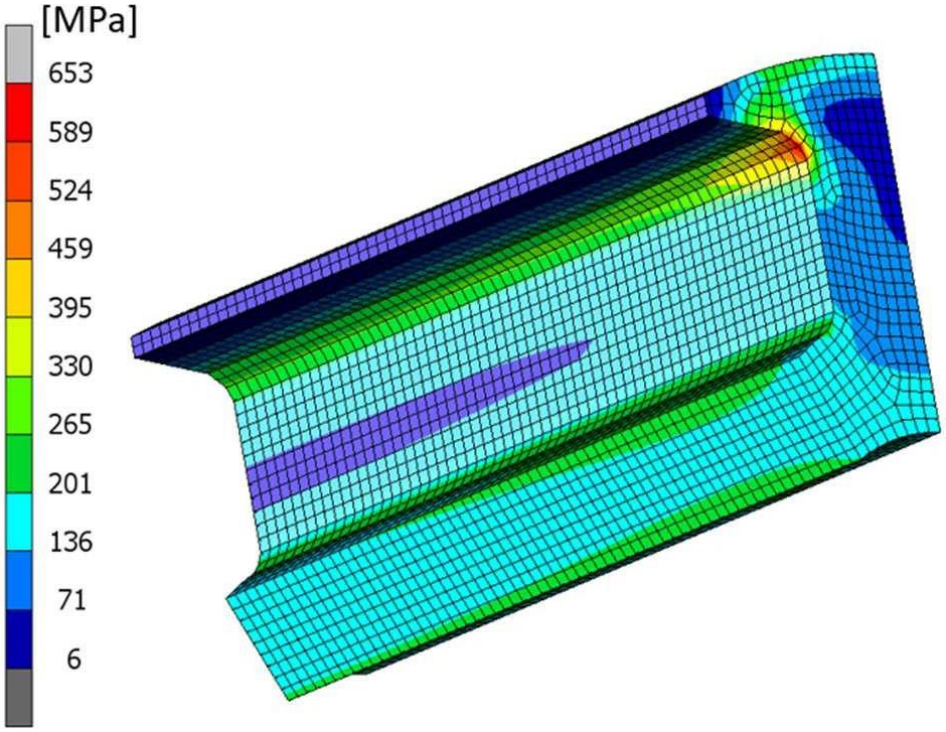

Figure 3.12 - Equivalent von Mises stress contour plot of the rotor

Figure 3.13 presents the radial displacement of both the rotor and the winding, showing that the deformation is negligible compared to the original configuration. The addition of the steel layer increases the total axial length of the rotor by *8 mm*, from *245 mm* to *253 mm*. This length increase leads to a corresponding increase in the winding length, resulting in approximately a *2.7%* rise in Joule losses in the rotor winding a reasonable trade-off for the enhanced mechanical stability.

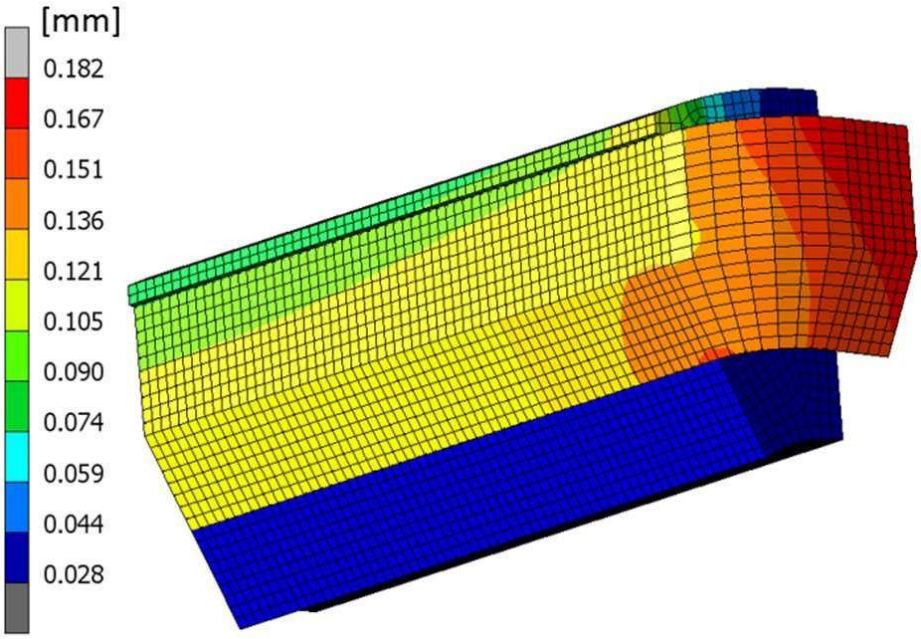

Figure 3.13 - Radial displacement contour plot of the assembly

Considering the computed displacements, this solution could enable the reduction of the air gap thickness from *2 mm* to *1 mm*, potentially improving the performance of the wound-field synchronous machine (WFSM). This further geometrical interaction will be considered in the future work.

3.4. CFD Analysis

The second significant aspect addressed in this chapter is the thermal analysis, which plays an important role since the maximum temperature affects both power density and efficiency of the machine [52]. The heating in electrical machines is primarily due to the internal losses and the temperature distribution is governed by the balance between generated heat, cooling and thermal capacity [70]. Heat removal takes place with different mechanisms, conduction through the solid components, convection (natural and forced) via cooling circuit and/or air flow and radiation. The thermal field of an electric machine is the result of complex 3D phenomena, such as heat transfer through composite components (for example the insulated wires deployed inside the slots) and complex turbulent air flows in the end-caps [126]. Therefore, an accurate analysis of such phenomena is usually time-consuming and not effortless. 3D CFD simulations, especially conjugate heat transfer (CHT) ones, can be proficiently adopted to evaluate an electrical machine thermal field. CHT occurs when at least two different heat transfer mechanisms are simultaneously involved. In the present chapter, a CHT simulation is carried out to evaluate the thermal field of the investigated generator, following a well consolidated methodology developed in the past by the authors [127]. The CHT model allows to account for both the conduction heat transfer in the solid components and the forced convection related to both the water jacket and the axial air flow that cools the rotor.

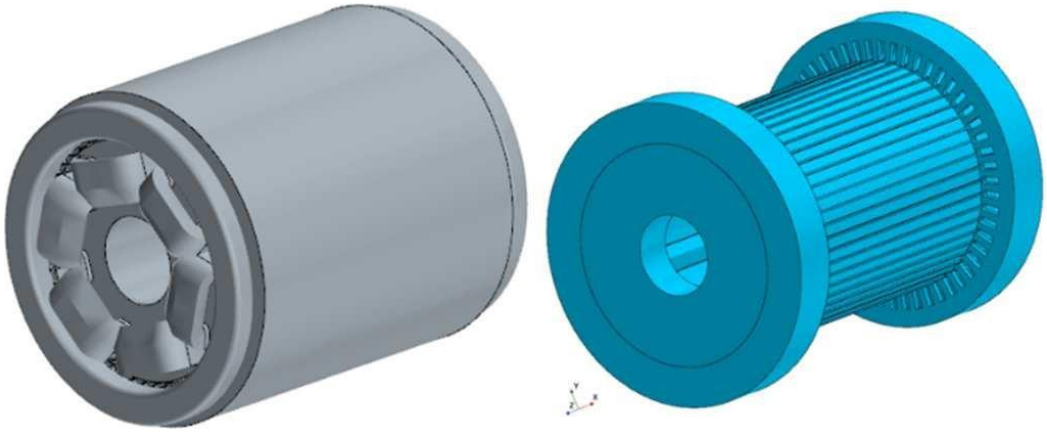

Figure 3.14 - Solid and fluid domain

3.4.1 CHT Model – Pre-processing

The CHT model of the 6-poles generator is built in STARCCM+ licensed by SIEMENS DSWI and it is used to evaluate the thermal field of the solid components. Rotor, stator and windings are included in the solid domain. The fluid one is represented by the cooling air, as depicted in Fig. 3.14. In order to account for the rotor motion (and the relative effect on the flowing air) with a fixed mesh, thus saving computational cost and time, a moving reference frame approach is adopted. The fluid region is simulated using the RANS k-ϵ Realizable Two-Layer turbulence model. An all y+ approach recently developed by the authors [128] is chosen for the wall treatment in order to properly model the near-wall flow throughout the cooling jacket, regardless the y+ value (i.e. regardless of the local mesh resolution and the flow conditions inside the circuit). It relies on a high-Reynolds near-wall grid and it forces the use of wall functions even in case of low y+ values, thus avoiding the use of very refined layers in the near-wall region. As for the mesh, polyhedral cells are used to discretise the entire CHT domain. Prismatic layers are added next to the fluid walls in order to improve the boundary layer modelling. Maximum cell size is set to *5 mm* in the air region and *10 mm* in the solid region, while the minima are *1 mm* and *5 mm*, respectively, in order to reduce total number of cells and, simultaneously, to have an accurate mesh in the fluid domain. A detail of the mesh is reported in Fig. 3.15, where an axial section cutting both solid and fluid domains is visible.

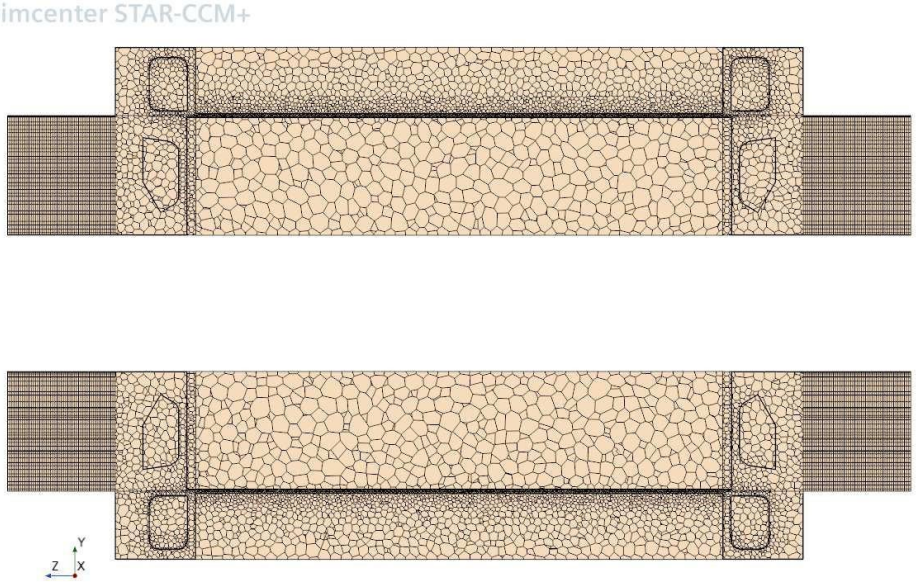

Figure 3.15 - Detail of the polyhedral mesh for solid and fluid regions

Boundary conditions (BCs) are defined in order to replicate the presence of both a fan that triggers the air flow on the rotor and a water jacket that cools down the stator. In particular, a mass flow rate and a temperature are imposed at the inlet and they are equal to *0.186 Kg/s* and *300 K*, respectively. A pressure is fixed at the outlet and it is equal to the ambient one (i.e. *1 bar*). A heat transfer coefficient and a reference temperature are imposed at the top of the stator to mimic the presence of the water jacket and they are fixed to *1000 W/m^{2}K* and *300 K*, respectively. As for the physics of the problem, air is modelled as an ideal gas and the solid as a multi-part domain made of copper (in the windings) and Fe-Si M330-35A (in both rotor and stator). The presence of the insulation system for both rotor and stator windings is taken into account through the definition of an orthotropic thermal conductivity. An equivalent axial thermal conductivity of *251.15 W/mk* (obtained considering a fill factor of *0.65*) and a transversal one of *1.4 W/mk*. Contact resistances are used to model the insulation liners in the stator and rotor slots with a value of *0.0002 W/m^{2}K* and the glue between the layer of 38NiCrMo4 and the rotor core with a value of *0.0009 W/m^{2}K*. Interfaces are placed in correspondence of the contacts among the solids and between solid and fluid domains to allow heat transfer. As for the rotor and stator core and windings, heat sources are placed to simulate the presence of the electromagnetic losses. The latter are estimated by an electromagnetic analysis in the designed machine at full load considering the conductivity of copper at 20 °C and they are briefly resumed in Tab. VI [52].

TABLE VI: AVERAGE VALUES OF ELECTROMAGNETIC LOSSES

	Hysteresis Loss	**Eddy Current Loss**	**Ohmic Loss**
Rotor	17.04 W	25.10 W	892.82 W
Stator	4138.00 W	2492.91 W	314.64

3.4.2 CHT – Computational Results

Once the convergence is met, the generator thermal field can be critically discussed. Figure 3.16 shows the temperature map on the axial section of the machine cores.

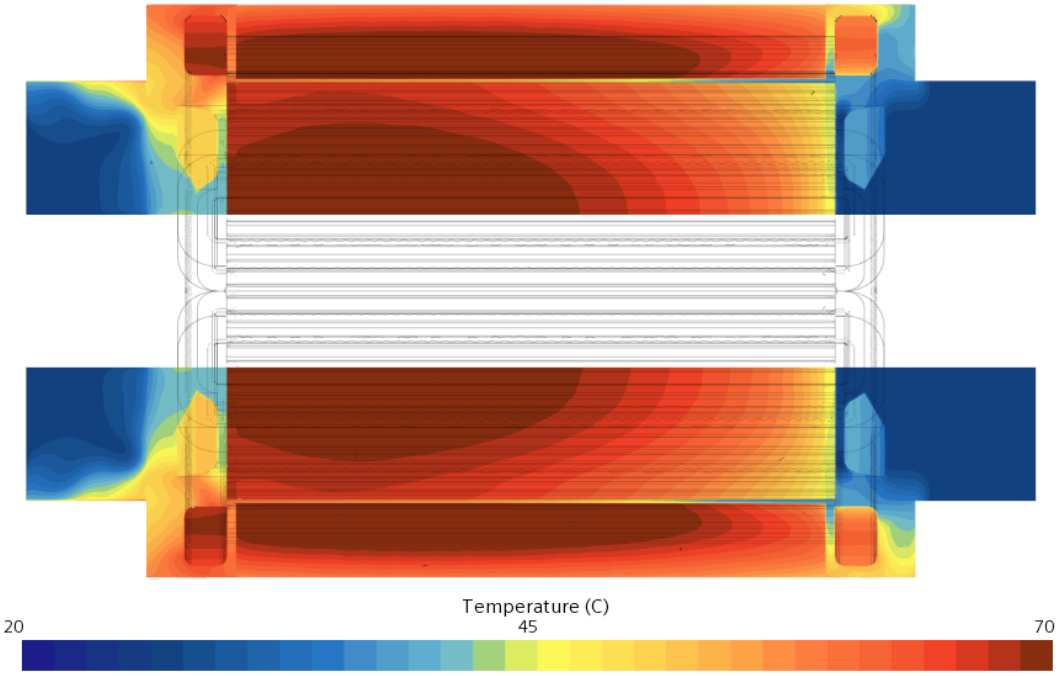

Figure 3.16 - Temperature map on the axial section of the machine cores

The cool air enters the domain on the right and it exits on the left. This is the reason why an increase of temperature along the axial direction can be noticed from the right to the left. The highest temperatures are registered in both stator (*76 °C*) and rotor (*72 °C*) cores at the interface with the winding. Figure 3.17 shows the temperature map on the axial section of the rotor and stator windings. The highest temperatures are recorded at the back end-winding (*72 °C*) and at the interface of the rotor winding with the rotor core (*73 °C*). As for the stator winding, the highest temperatures are at the interface with stator core (*75 °C*) and at the interface with the airgap (*75 °C*). The heat power balance highlights that the air flow produced by the fan cools down the rotor. However, it also helps to cool the temperature of the stator of nearly *6 °C*. Both the temperatures of stator and rotor windings are lower than the limits imposed by the insulation class. This means that there is a significant room for increasing the current density values in both rotor and stator windings,

thus potentially obtaining a significant increase of the WFSM performance. These further studies will be presented in future research.

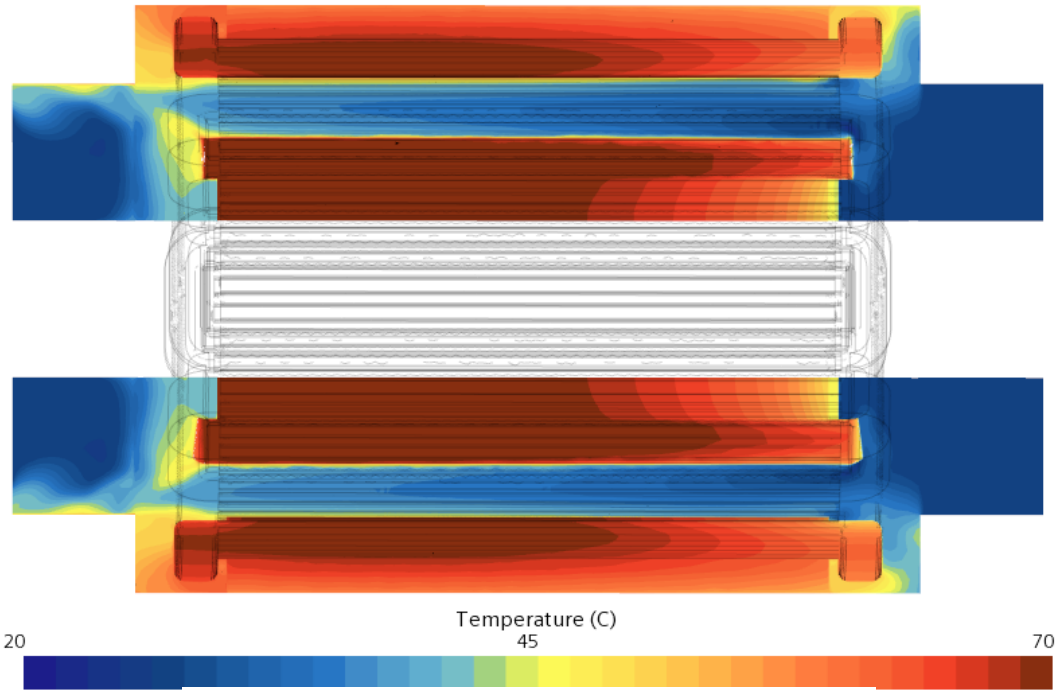

Figure 3.17 - Temperature map on the axial section of the windings

3.5. Conclusion

This chapter investigated the possibility of increasing the performance of a previously designed salient-pole, WFSM, intended to cope with the electric energy demand in a MEA application. To do so, in-detail structural and thermal investigations were performed through purposely built 2D and 3D FE models for the structural aspects, and 3D CFD model for the thermal ones. The structural high speed requirement, achieved through end plates made of a suitable material, indicated negligible values of the displacements. This would allow to significantly reduce the airgap thickness, currently equal to *2 mm*. The CFD analysis, carried out considering a fan and a water jacket as cooling systems for the machine, indicated low values of the temperatures in the stator and rotor cores and windings, with a maximum value of *76.2 °C* recorded in the stator winding. This would allow to significantly increase the current density values in the generator. The results highlighted a significant room for increasing the performance of the generator, when the design recommendation provided above were applied.

3.6. Contributions to research

The results of this chapter are reported in two academic publications in a high profile machines conference. The publication name is listed below.

- M. G. Pasquinelli, P. Bolognesi, A. Guiducci, S. Nuzzo and M. Galea, "Design of a High-Speed Wound-Field Synchronous Generator for the More Electric Aircraft," 2021 IEEE Workshop on Electrical Machines Design, Control and Diagnosis (WEMDCD), Modena, Italy, 2021, pp. 64-69, doi: 10.1109/WEMDCD51469.2021.9425625.
- A. Guiducci et al., "Refined Structural Design and Thermal Analyses of a High-Speed Wound-Field Generator for the More Electrical Aircraft," 2023 IEEE Workshop on Electrical Machines Design, Control and Diagnosis (WEMDCD), Newcastle upon Tyne, United Kingdom, 2023, pp. 1-6, doi: 10.1109/WEMDCD55819.2023.10110937.

The second paper was awarded as the best paper award of the conference.

4. CASE OF STUDY 2: Thermal Modelling of Advanced Rotor Cooling Solution for Traction Applications

This chapter explores alternative thermal management techniques of a rotor assembly of a high-speed salient pole WFSM for traction applications. The work was carried out during a six-month secondment of the author at Newcastle University, Newcastle, UK in the thermal management research group. In general, the rotor assembly of an electrical machine is very challenging in terms of effective heat removal. This is due to nature of the rotary part with a limited thermal path for extracting the generated heat. Further to this, factors like system integration and additional mechanical power loss need to be carefully considered for a well-balanced thermal management/electrical machine design. In this chapter, the author investigates several selected cooling techniques, which involves passing a fluid (air and/or oil-based coolant) through the rotor assembly. To facilitate the analysis, several design tools have been developed/used, including a simplified correlation-based thermal TEC, an FE method, and a CFD. The proposed methodology offers a computationally efficient approach, with the TEC used for initial trade-off study, and high-fidelity detailed CFD employed at later stage of the development process. A case study motor design is used here, to demonstrate the methodology. The initial theoretical predictions suggest that the active rotor cooling offers clear performance gains, as compared with the baseline rotor design with passive heat removal. Both convective heat transfer coefficient (HTC) and rotor power loss handling are discussed in the context of the overall motor performance/torque-speed envelope. Moreover, comments regarding the thermal management and motor system integration, and additional mechanical power loss are provided.

4.1. Introduction

Transportation electrification is recognized as a key strategy to address pollution, particularly in the automotive industry. The main motivations behind this trend are zero tailpipe emissions enabled by EVs, higher energy efficiency of electric powertrains than conventional ones, and the elevated price of refined fuels. In this context, there is a growing demand for electric motors with increased power density, often achieved by increasing the operating speeds. However, together with the structural challenges, power losses at high speed operation are a limiting factor and, thus, a primary design objective lies in efficiently dissipating the heat generated within the electrical machine. Thermal management in electrical machines is crucial for ensuring their reliable and efficient operation. The temperature reached is governed by the balance between heat generated, heat removed and thermal capacity. Major sources of loss are Joule losses in the windings, core losses due to eddy currents and hysteresis phenomena, and mechanical losses, such as bearing and windage losses [70]. Table VII shows how these depend on various operating parameters of the electrical machine: I is the current and R the resistance, Ω is the rotational speed, μ is the friction coefficient, D the rotor diameter, L the rotor axial length, B the magnetic flux density in the cores and ρ the air gap fluid density.

TABLE VII: DEPENDENCY OF POWER LOSSES ON MACHINE OPERATING PARAMETERS

Joule loss	$\propto I^2R$
Eddy current loss	$\propto \Omega^2B^2$
Hysteresis loss	$\propto \Omega B^n$
Bearing loss	$\propto \Omega\mu$
Windage loss	$\propto \Omega^3D^4L\rho$

Heat removal takes place with different mechanisms: conduction through the solid components, natural and forced convection, and radiation [13]. In this study, emphasis is given to the thermal modelling of cooling solutions on the rotor of electrical machines. Cooling the rotor poses significant challenges due to its status as a fast rotating component restricted within an air environment. In addition, at high rotational speeds, rotor losses could become comparable to stator ones (see Table VII), thus making this task even more complicated. Also, in wound-field machines, such as electrically-excited synchronous motors and induction motors, rotor Joule losses increase the cooling challenges [35]. Rotor cooling solutions are designed based on the specific requirements of the electrical machine, taking into account factors such as power rating, operating conditions and dimensions. The choice of cooling method depends on the desired level of cooling efficiency and the application requirements. In this work, four distinct scenarios of heat transfer in the rotor are examined:

- The rotational effect only;
- The rotational effect with an oil flow in the hollow shaft;
- The rotational effect combined with axial air flow in the annular gap;
- The rotational effect along with axial air flow and oil flow in the hollow shaft;

These scenarios are investigated using analytical correlations on simplified geometries and operating conditions. The aim is to prove their validity under various cooling conditions and extend it to more complicated rotor geometries, such as a salient-pole structure typical of electrically-excitated synchronous machines. To such purpose, thermal finite element and computational fluid dynamic analyses are performed.

4.2. Analytical correlations for heat transfer predictions

This section shows how to estimate the HTC in the main parts of the rotor using correlations defined in [129]–[132]. To simplify the burden, a basic system composed of two concentric cylinders is assumed as shown is Fig. 4.1.

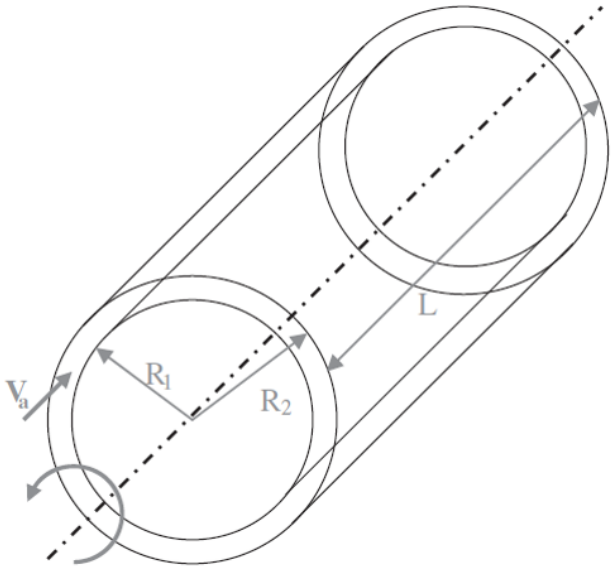

Figure 4.1 - The considered simplified geometry

The outer radius of the inner cylinder R_1, representative of the outer profile of the rotor, is equal to 66 mm in the following calculations. Whereas, the inner radius of the outer cylinder R_2, which is representative of the inner profile of the stator, is set to 67 mm. The air gap thickness δ is thus 1 mm, while the axial active length L is 100 mm. These dimensions are taken from an existing machine design for traction applications.

4.2.1 Airgap heat transfer prediction

Different studies [133], [134] on the heat transfer of electric motors have demonstrated the importance of convective heat transfer within the cylindrical gap (i.e. the area separating the rotor from the stator). In fact, the rotor is the locus for

largescale dissipations of electromagnetic losses, and its cooling is ensured principally by the air flow of the cylindrical gap. From the heat transfer point of view, two main families of rotating electric machines may be distinguished: closed frame machines, characterised by rotor rotation without axial air flow (Taylor-Couette flow), and open frame machines, featuring an axial flow combined with rotor rotation (Taylor-Couette- Poiseuille flow) [135]. To estimate the HTC in the airgap a number of analytical correlations are used in this section. However, starting from the ratio of the Taylor number (Ta) and a geometrical factor (Fg) it was possible to identify the flow condition and select the specific empirical formulas to estimate the Nusselt number (Nu) which is required for deriving the convective heat transfer coefficient. The Taylor number is a dimensionless number applicable to cylindrical geometry machines. It provides an indication of the relative effects of inertial forces and viscosity in an annular region with rotation of the cylindrical surface. This is calculated as in (5), where $r_m = (R_1+R_2)/2$, and ν is the kinematic viscosity of the fluid.

$$Ta = \frac{\Omega\, r_m^{0.5}\, (R_2 - R_1)^{1.5}}{\nu} \tag{5}$$

The factor Fg is calculated as in (6), where S is determined as in (7).

$$F_g = \frac{\pi^2}{41.19\,\sqrt{S}} \left(1 - \frac{(R_2 - R_1)}{2\, r_m}\right)^{-1} \tag{6}$$

$$S = 0.0571 \left(1 - 0.652\, \frac{(R_2 - R_1)/r_m}{1 - (R_2 - R_1)/(2\, r_m)}\right) + 0.00056 \left(1 - 0.652\, \frac{(R_2 - R_1)/r_m}{1 - (R_2 - R_1)/(2\, r_m)}\right)^{-1} \tag{7}$$

When Ta is low, then the flow is a laminar shear flow and, for $T_a^2 / F_g^2 < 1700$, heat transfer is dominated by conduction and can be predicted for inner surface using

the correlation reported in (8) [129], where $D_h = 2(R_2 - R_1)$, k is the thermal conductivity of the fluid and h is the HTC.

$$Nu = \frac{h\,D_h}{k} = \frac{2\,[(R_2 - R_1)/R_1]}{\ln[1 + (R_2 - R_1)/R_1]} \tag{8}$$

For laminar flow with vortexes ($1700 < T_a^2\,/F_g^2 < 104$), Nu can be found as in (9) [130], [136], whereas for turbulent flow ($104 < T_a^2\,/F_g^2 < 107$) it can be determined using (10) [130], [136].

$$Nu = 0.128\left(\frac{T_a^2}{F_g^2}\right)^{0.367} \tag{9}$$

$$Nu = 0.409\left(\frac{T_a^2}{F_g^2}\right)^{0.241} \tag{10}$$

The above correlations all apply to Taylore-Couette flow whereas the remainder of this section concerns the case of axial throughflow. Moving to the axial flow in the airgap combined whit rotor rotation we assumed an axial air velocity $v_a = 6$ m/s. In this case to estimate the Nusselt number we use the Konesterin and Finatev correlation reported in (11) [131].

$$Nu = 0.018\left\{Re_z\left[1 + 0.6\left(\frac{\Omega R_1 D_h/\nu}{Re_z}\right)^2\right]^{0.5}\right\}^{0.8} \tag{11}$$

The correlation is valid for $0 < \frac{\Omega R_1 D_h}{\upsilon} < 10^5$ and $3000 < Re_z < 3\cdot10^4$, where $Re_z = \frac{v_a\,D_h}{\upsilon}$.

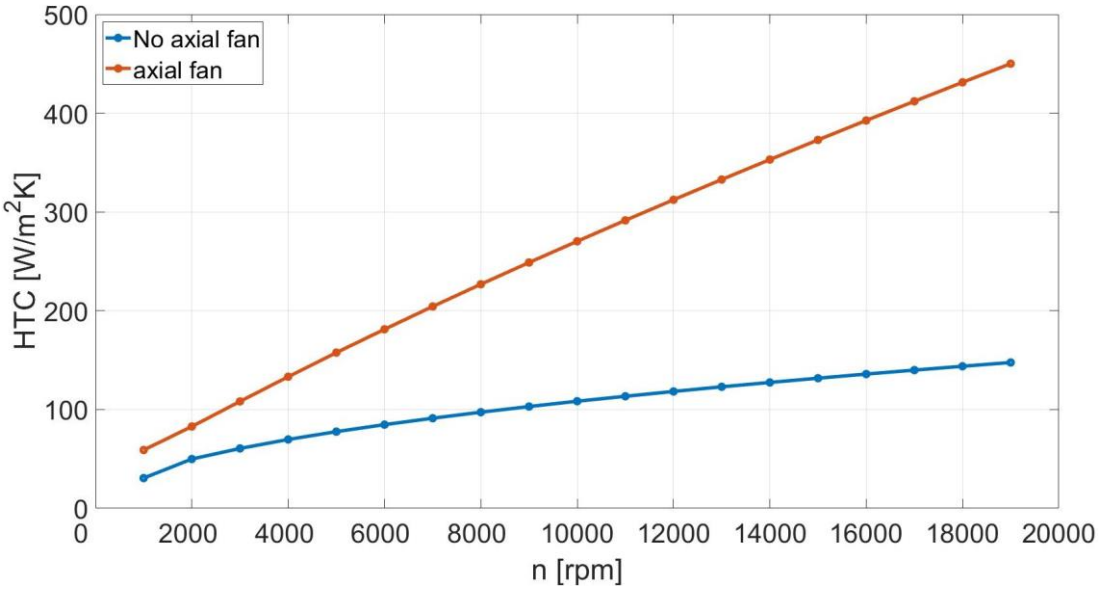

Figure 4.2 - HTCs in the air gap vs. rotor speed

Fig. 4.2 illustrates the trend of the HTCs vs. rotational speed for both flow conditions. The case with no axial flow shows a slight increase of the HTC vs. speed. Contrarily, axial flow cooling enables a significant increase of the HTC at high rotational speeds.

4.2.2 Rotor end cap heat transfer prediction

The rotor end caps and air heat transfer is mainly dominated by air convection. The Nusselt number Nu is defined as in (12) [137], where $\mathrm{Re_r} = \frac{\Omega R_1}{\upsilon}$ and $Pr = \frac{c_p \mu}{k}$.

$$Nu = \frac{0.585\ Re_r^{0.5}}{\frac{0.6}{Pr} + \frac{0.95}{Pr^{1/3}}} \qquad (12)$$

Figure 4.3 shows the HTC trend vs. speed in the the rotor end caps.

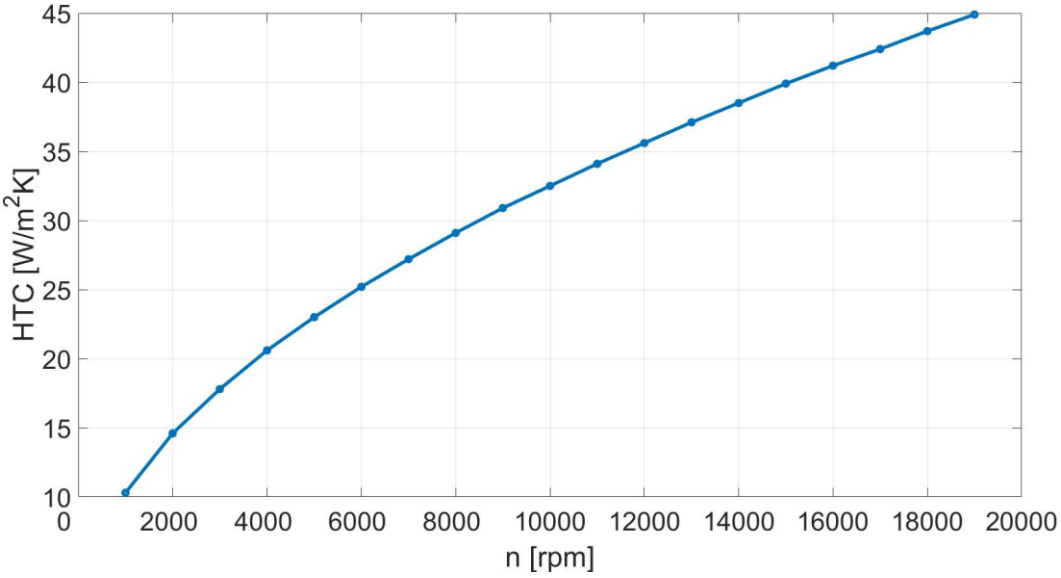

Figure 4.3 – HTC trend in the rotor end cap vs. rotational speed

4.2.3 Heat transfer prediction for axially flooded rotor shaft

The rotor shaft cooling is approximated as an axially oil flooded rotating hollow cylinder. The heat transfer in a rotating shaft is dominated by the fluid behaviour in axial and radial directions, the geometry of the shaft, and the fluid properties [138], [139].

Recent research on oil-cooled shafts of traction motors showed that the destabilising effect of the high rotational speed increases the heat transfer and, therefore, the rotor shaft cooling is a quite effective cooling method for traction motors [138], [139]. For laminar flow (Re < 180), (13) is proposed to determine Nu in steady state conditions [132], where Rer = $\frac{0.5\ \rho D V_r}{\mu}$ (with Vr being the velocity in [m/s] at the inner radius of the hollow shaft), ρ is the density and μ is the viscosity of the E-fluid M oil.

$$Nu = 3.8111 \left(\frac{1}{Re_r\ Pr}\right)^{-0.641} \qquad (13)$$

Considering an oil volume flow rate of *3 l/min* and hollow shaft diameter d of 12 mm, the trend of the heat exchange of the oil in the hollow shaft is shown in Fig. 4.4, where the HTC increases with the rotation speed can be observed.

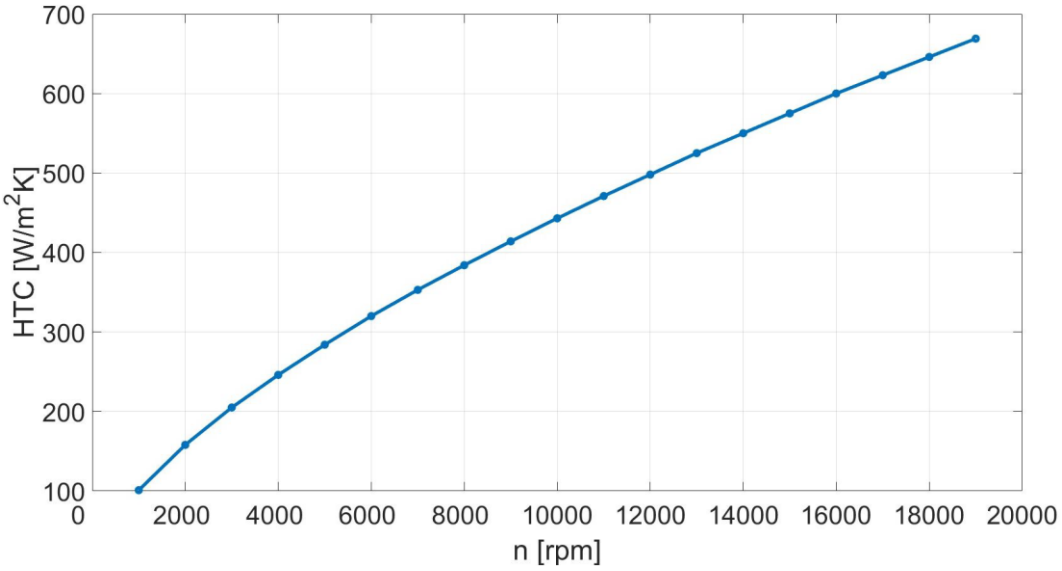

Figure 4.4 - HTC for axially flooded rotor vs. rotational speed

4.3. Simplified Analysis

In this section an analytical model to estimate the maximum heat extraction for each of the cooling solutions listed in Section I is developed in MATLAB/Simscape. The simplifying assumptions are:

- a simple geometry of the rotor is assumed, as in Fig. 4.1;
- the heat flows in the radial and axial directions are independent;
- a single mean temperature defines the heat flow both in radial and axial directions;
- the thermal capacity and heat generation are uniformly distributed;
- no interaction between the rotor and the stator is considered, i.e. only rotor simplified representation is considered;
- rotor is modelled as an equivalent homogeneous structure (material).

Fig. 4.5 illustrates the representation of the rotor modelled within Matlab Simscape environment. The power losses are introduced as heat source within the block, and the resulting heat flux is predicted in both radial and axial directions along the core.

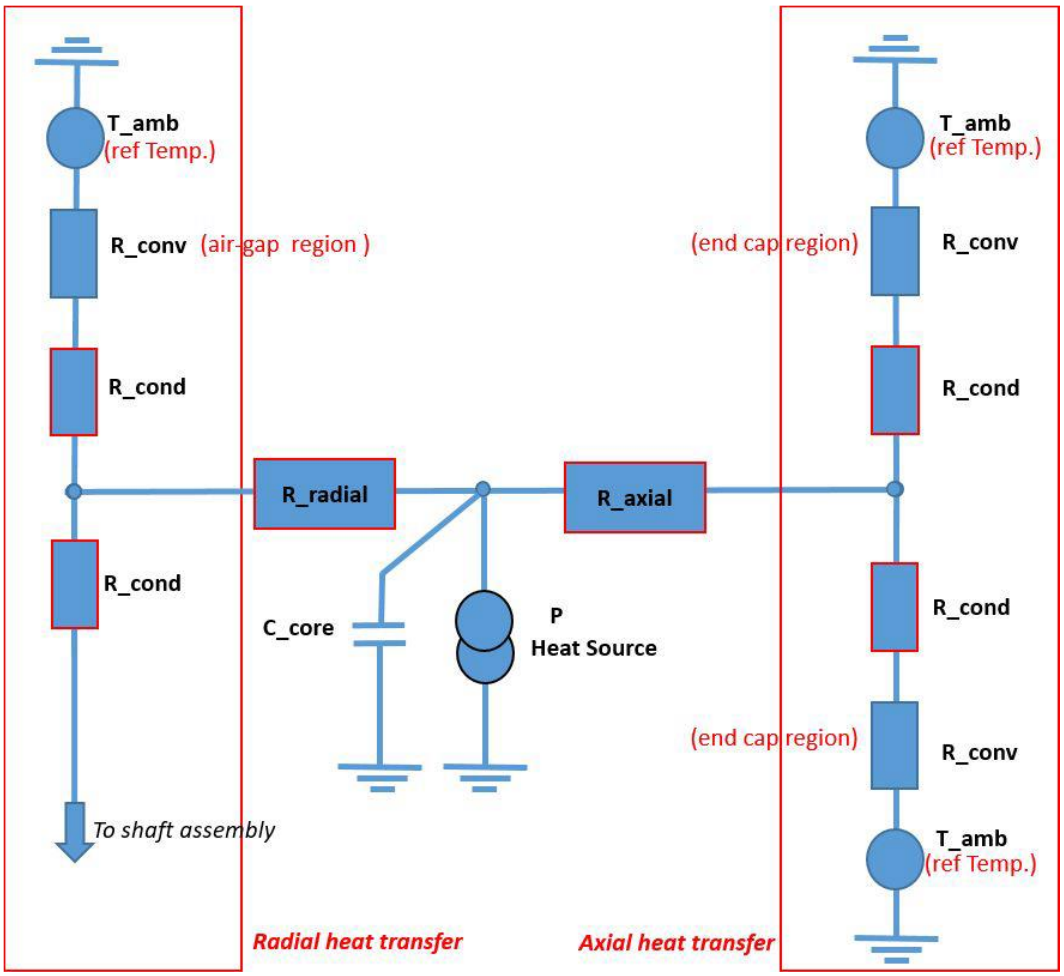

Figure 4.5 - Rotor core layer modelled in MATLAB Simscape environment

The maximum temperature is set at *180 °C* corresponding to the maximum temperature allowed for class H insulation and an ambient temperature of *25 °C* is considered. The T-model introduced in [140] is used, where all the resistances are described in detail. The conduction thermal resistances are defined to model the conduction heat transfer in the radial and axial directions of the rotor core and the shaft. The heat flux is directed radially from the rotor core to the air gap and from the core to the shaft. Conversely, in the axial direction, it extends from the centre of the cylinder to each end cap. Consequently, there are four thermal resistances: two in the radial direction and two in the axial direction for each layer. The other two resistances Rradial and Raxial located adjacent to the heat source block are referred to as interconnecting resistances, serving to connect the two distinct heat paths.

Regarding convection heat transfer, the model defines two convection thermal resistances in the radial direction: one for the heat transfer with the air and one for heat transfer with the oil through the shaft, in the case of an oil cooling solution being in place. Along the axial direction, the model incorporates two convective thermal resistances for each end cap, accounting for heat transfer with the air in the rotor core layer and the shaft, respectively. These two convection thermal resistances are determined using the HTCs derived from (8) provided in each cooling case. The cooling solutions are modelled with the corresponding HTCs obtained from the above analytical correlations. Two thermal capacities are specified in the model, one for the rotor material NO20 and another for shaft made of steel AISI8620. Aim of this model is to rapidly estimate the amount of heat that can be extracted from each cooling solution.

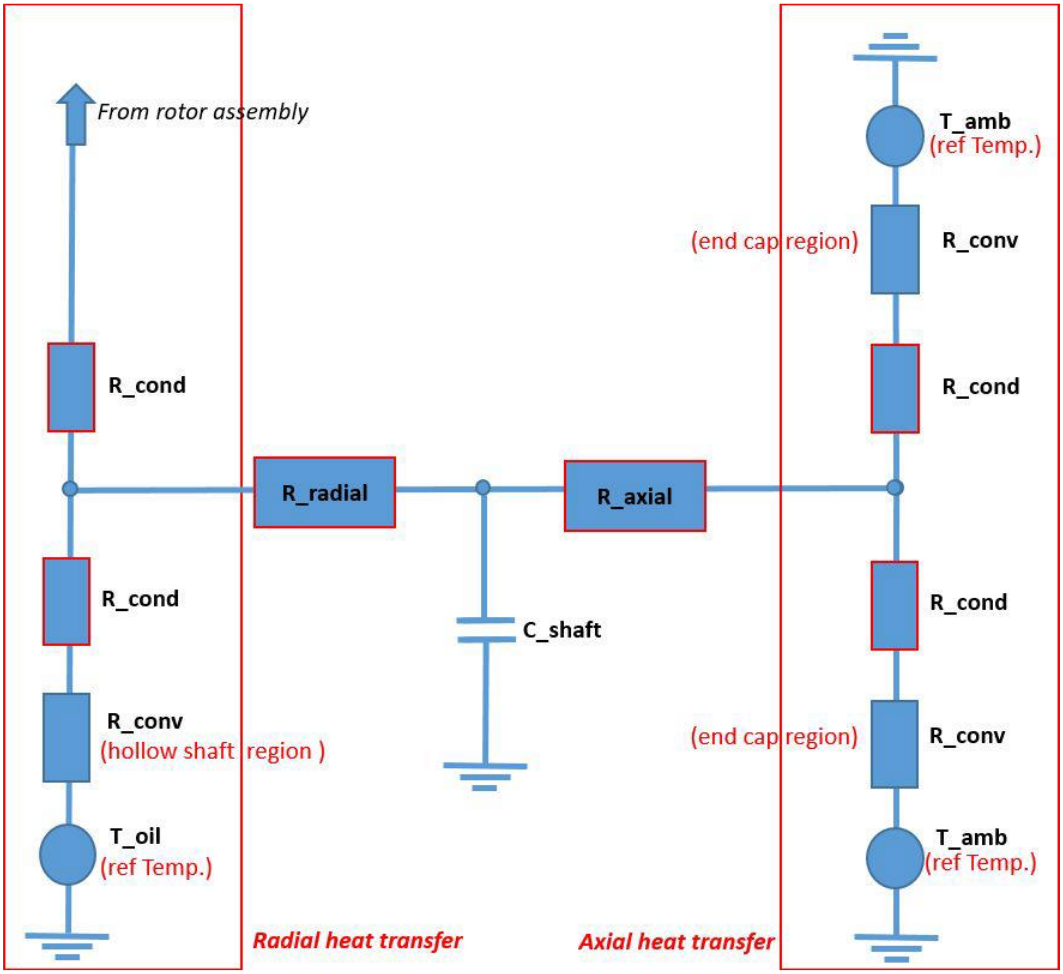

Figure 4.6 - Shaft modelled in MATLAB Simscape environment

The same modelling methodology is applied to the shaft layer, as depicted in Fig. 4.6, with an external shaft diameter of *60 mm*. In this case, there is not heat source as all losses are injected into the rotor core layer.

The cooling performance varies according the considered scenario, with an increasing trend from Case 1 to Case 4. The considered cases are summarised below:

1) *Case 1 - Rotational effect*: Heat dissipation occurs through the heat transfer from the rotor body via the air-gap and ends, as a result of the rotor motion covering a speed range from *1 krpm* to *18 krpm*. The convective resistance takes into account the HTCs estimated through (4)-(6) corresponding to the specified speed range.
2) *Case 2 - Rotational effect and hollow shaft*: Heat dissipation occurs through both the rotational motion of the rotor and the oil flow inside the hollow shaft, with a volumetric flow rate of *3 l/min*. The hollow diameter is set equal to *12 mm*. This solution is incorporated in the HTC of the convective thermal resistance in the shaft layer, where the HTC values are determined using (9).
3) *Case 3 - Rotational effect and axial flow*: Heat dissipation occurs through the combined effects of the rotational motion and axial airflow at *6 m/s* in the airgap. Specifically, the HTCs of the convective thermal resistance in the radial direction of the rotor core are estimated using (7).
4) *Case 4 - Rotational effect, axial flow and hollow shaft*: Heat dissipation is achieved through the combined mechanisms of rotational motion, axial airflow at *6 m/s* in the airgap, and oil flow at *3 l/min* within the hollow shaft. The convective thermal resistances in the radial direction utilize the HTCs from (7) to simulate the presence of an axial fan. Additionally, (9) is employed to model the oil flow within the shaft.

4.3.1 Case study: WFSM for traction application

Considering as case study a 6-pole electrically-excited synchronous traction motor as shown in Fig. 4.7, whose main data and geometrical parameters are shown in table VIII.

TABLE VIII: DATA OF THE MACHINE

Parameter	**Value**	**Unit**
Peak Power	160	kW
DC bus voltage	500	Vrms
Stator current	250	Arms
Base Speed	6000	rpm
Rotor DC current	16	A
Poles	6	
Stator slots	72	
Outer stator diameter	202	mm
Inner rotor diameter	133	mm
Active axial length	100	mm
Air-gap thickness	1	mm

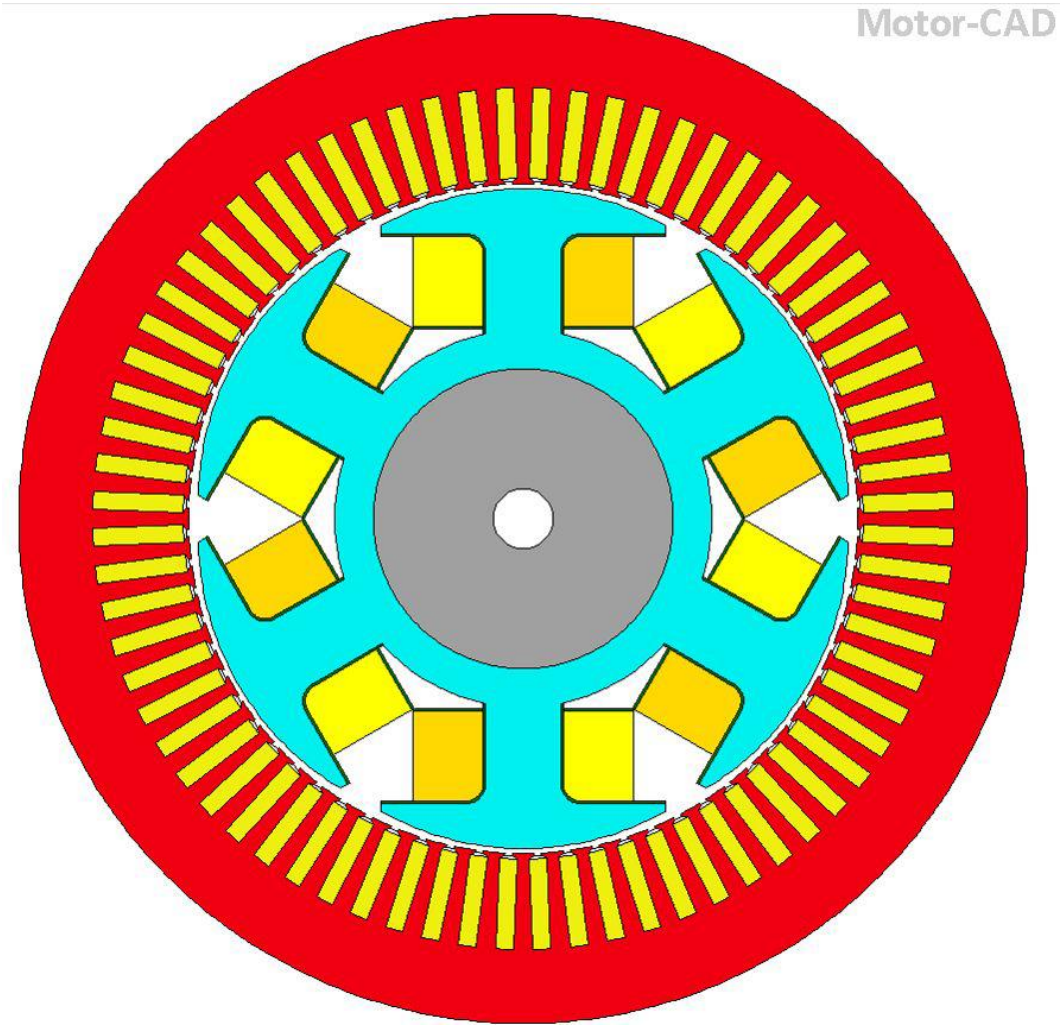

Figure 4.7 - Wound-field high-speed synchronous motor for traction application

4.3.2 Results and application

Fig. 4.8 shows the power heat loss dissipated for the four cases vs. speed, which ranges from 1 krpm to 18 krpm. The highest cooling performance is found for Case 4, as expected. The axial airflow impacting the rotor contributes significantly to improve heat dissipation, particularly evident in Case 3 at high rotational speeds. This means that direct air cooling is very efficient solution to extract heat from the rotor. However, given the operating speeds typically employed in traction applications, it is necessary to have a separate fan on the shaft rotating independently on the rotor speed.

Hollow shaft liquid cooling is rather a conventional method nowadays, since it is relatively easy to manufacture but lacks in thermal performance due to the relatively high interface resistances from heat source (rotor core, winding and magnets) to the coolant within the shaft [141].

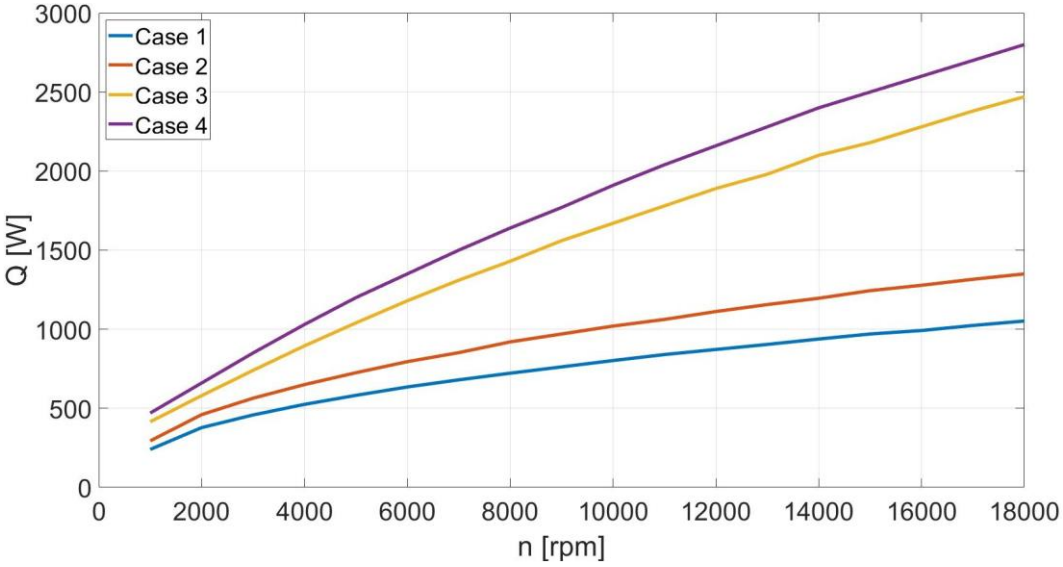

Figure 4.8 - Dissipative power loss (generated heat) versus rotational speed for 180 °C of the rotor body

The rotor copper losses of the case study obtained using MotorCAD software are plotted in Fig. 4.9. While being a very sustainable solution as opposed to permanent magnet machines, this wound-field topology is characterised by lower torque density and efficiency values. To reduce the extra rotor losses and increase the torque density of the machine, implementing a high-performance rotor cooling system is of paramount importance, thus making this investigation worthy. Together with the rotor losses, Fig. 4.9 shows the heat extraction capabilities of each cooling solution in the torque-speed envelope. The dotted line envelope delineates the thermal limits for each scenario. It can be observed that cases 3 and 4 appear overly aggressive, extracting more heat than necessary from *3 krpm* onward. In contrast, at low speeds cases 1 and 2 show cooling limitations. From *1 krpm* to *3 krpm* all the cases demonstrated a thermal limit due to the low rotor speed.

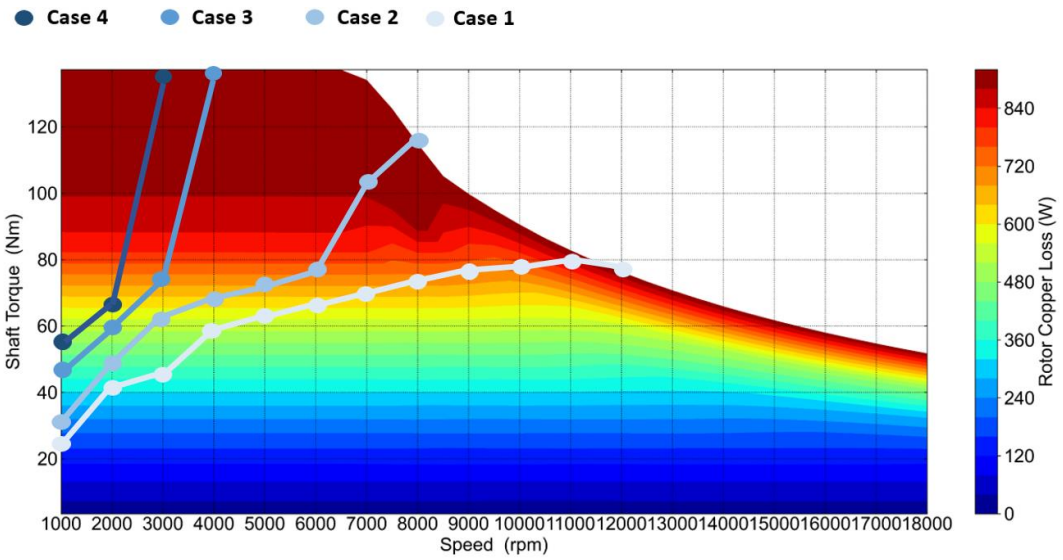

Figure 4.9 - Rotor copper losses map in Torque-speed curve

4.4. Detailed Analysis

The aim of this section is to compare the results obtained from the simplified model with those derived from a 3D FE thermal model using the same boundary conditions. A 3D FE thermal model for one pole of the electrically-excited synchronous motor at hand is built in Simcenter Thermal, as shown in Fig. 4.10. The FE model considers the same geometric dimension and HTC as the analytical model. As a cooling solution for the rotor, the thermal model considers oil flow towards a hollow shaft and an axial air flow generated by a fan, i.e. the Case 4 cooling scenario is investigated through the FE model.

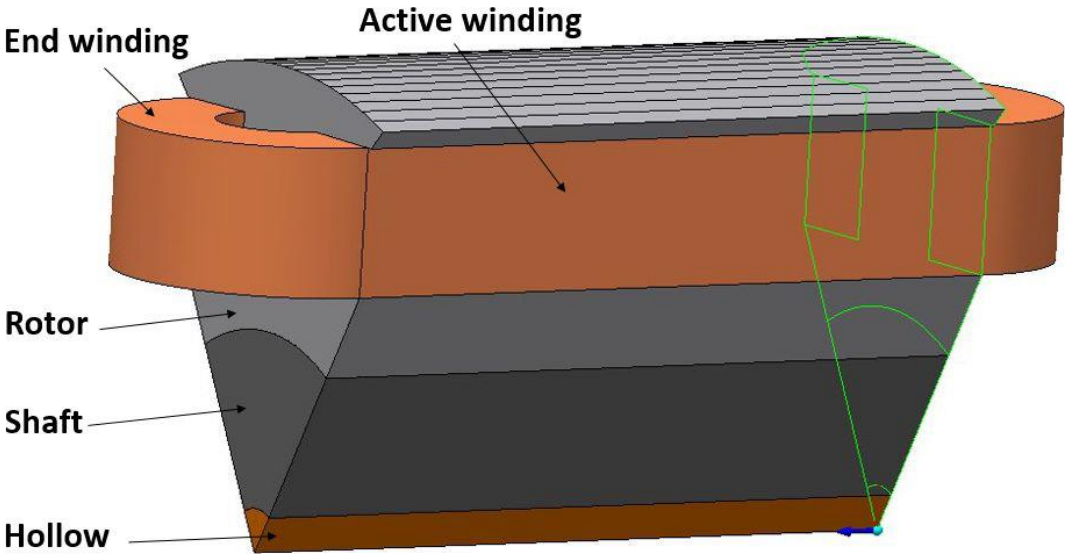

Figure 4.10 - FE model of one rotor pole

Fig. 4.11 shows the comparison between analytical and FE results in terms of thermal power extracted vs. rotational speed. The main differences are that in the FE model the more representative geometry of the rotor is modelled, the presence of copper winding and the relative heat transfer with air are considered. An acceptable match can be observed, with a discrepancy up to *22%* being registered at *2 krpm*. As expected the simplified model representation of the rotor overestimates the maximum dissipative power loss handling for a given heat removal scenario.

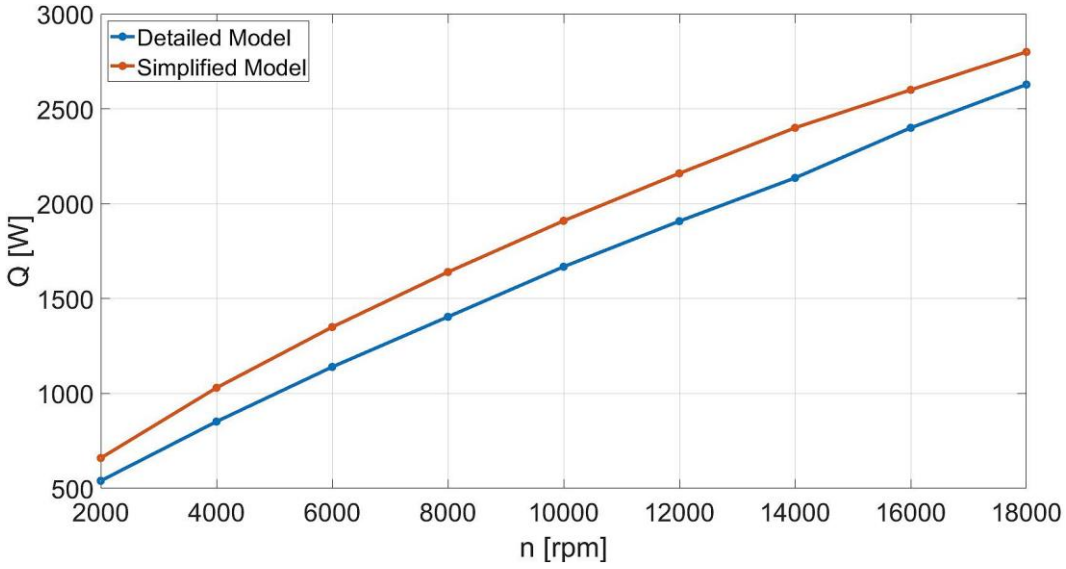

Figure 4.11 - Comparison between analytical and 3D FE results in terms of power extracted vs. rotor speed

It is worth mentioning that an approximation in both the analytical and FE models is considered for the HTC. This consists of assuming a homogeneous HTC value on the surfaces. On the contrary, it is expected that the HTC distribution is not very homogeneous. To such purpose, a 3D CFD analysis is carried out leveraging on the researches presented in a previous authors` publication [13]. In particular, a CHT simulation is performed to evaluate the thermal field of a wound-field high-speed machine, to which more complexity is added such as the 3D geometry of the rotor, including the end-winding region, and considering the interaction with the stator. The CHT model allows to account for both the conduction heat transfer in the solid components and the forced convection heat transfer related to both the water jacket that cools the stator and the axial air flow that cools the rotor, which rotates at *15 krpm*. Fig. 4.12 illustrates the solid (rotor, stator and windings) and fluid (air) domains of the CHT model.

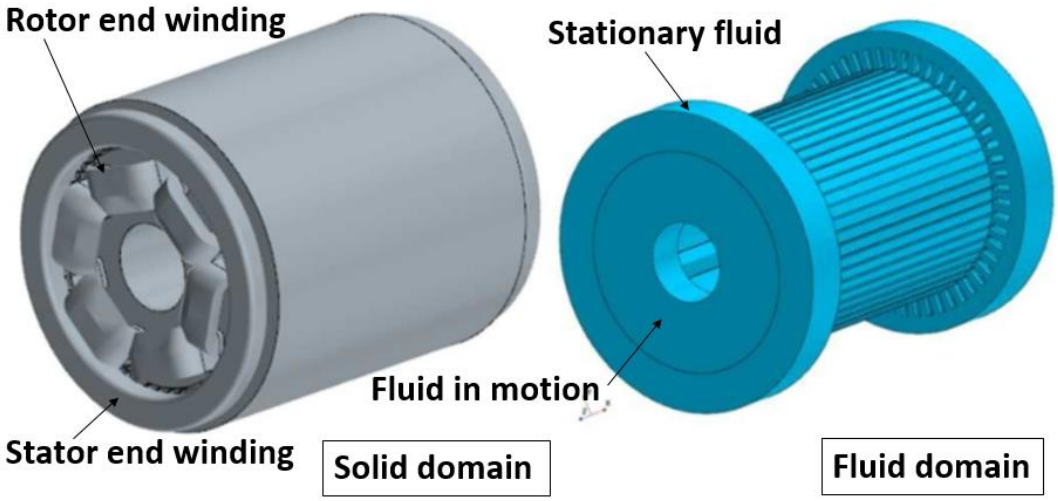

Figure 4.12 - Solid and fluid domains of the electrically-excited machine

Fig. 4.13 shows the HTC map of the rotor front surface investigated directly by a mass flow air rate of *0.186 kg/s*. The average HTC value on rotor end-winding and end cap surface is *190.02 W/m^{2}K*. There is a rather homogeneous value in the rotor end-winding, while the HTC is increased in the rotor shoes.

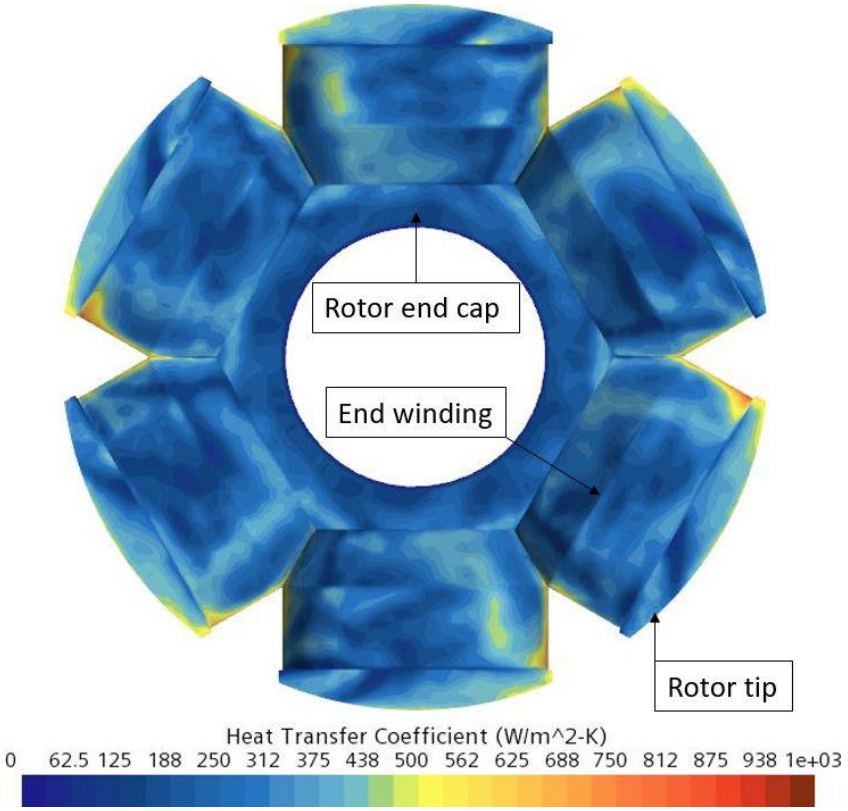

Figure 4.13 - HTC map of the front rotor

Fig. 4.14 illustrates the HTC map in the rotor outer surface, where the axial flow enters the rotor from right to left. The range is pretty uniform, with an increase of the HTC at the inlet. The average HTC value on the rotor top surface is *251.89* W/m^2K.

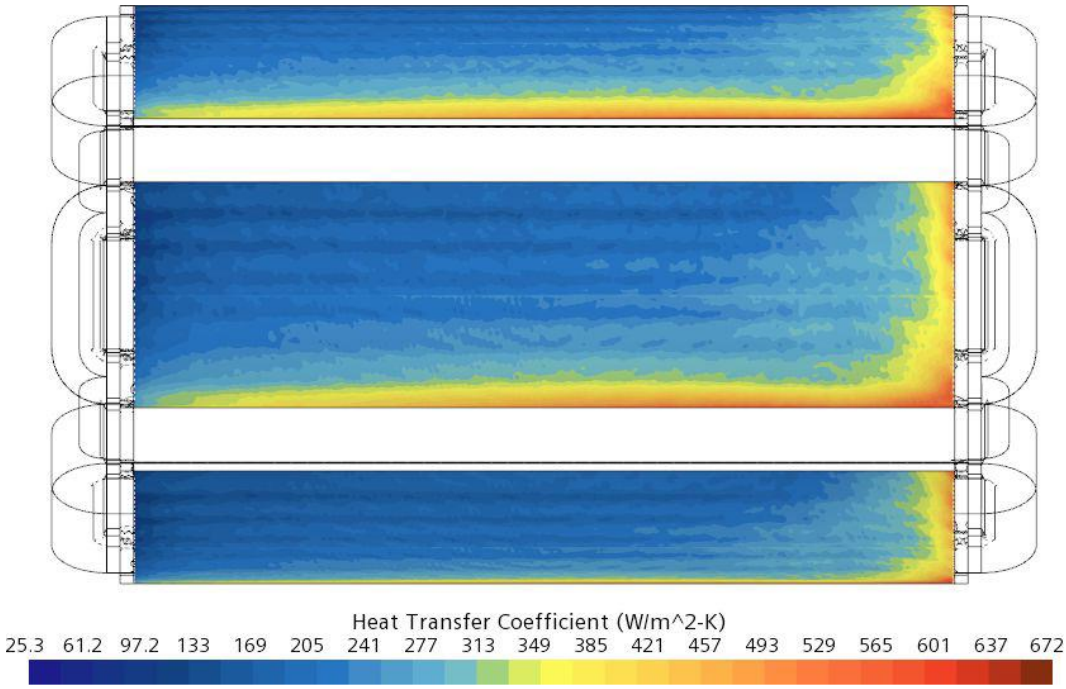

Figure 4.14 - HTC map of the top salient rotor view

The literature indicates a lack of a correlation for estimating the HTC on the rotor winding surface. However, CFD can be employed for this estimation. Fig. 4.15 illustrates the HTC map on the rotor active winding surface interacting with air. The elevated values on the right side result from the influx of fresh air moving from right to left. The average HTC on this surface amounts to *224.91* W/m^2K.

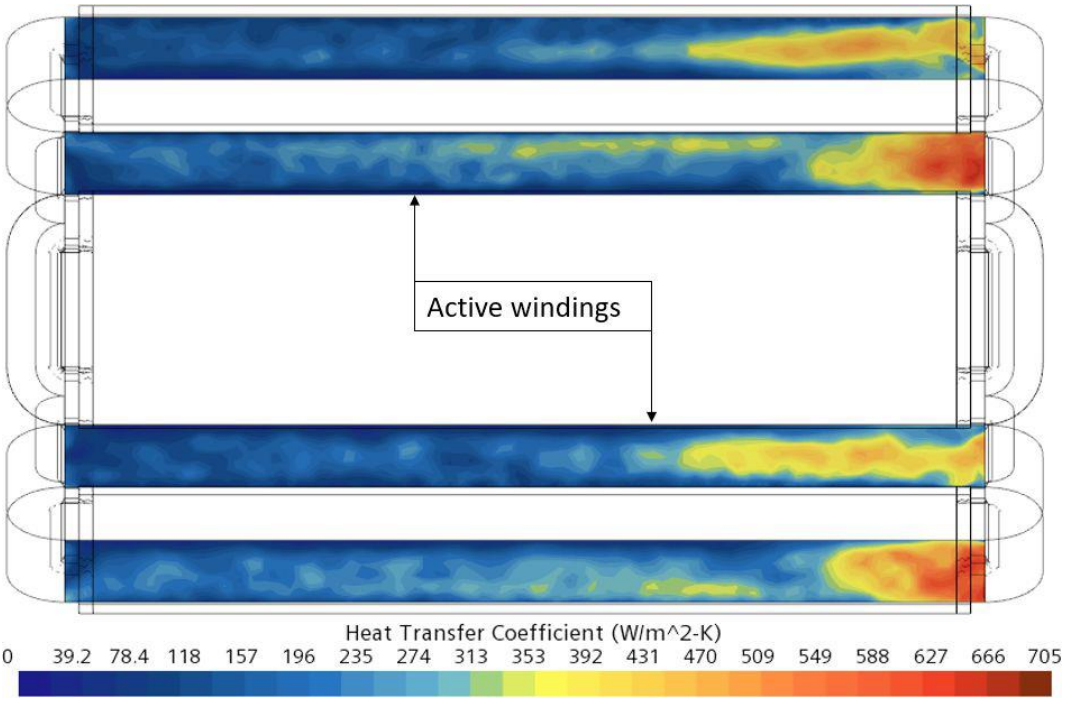

Figure 4.15 - HTC map of the rotor winding surface

The HTC maps obtained from CFD simulations highlight that the HTC vary significantly from point to point. However, using suitable homogeneous values in both the analytical and FE models allow for a more manageable representation in the simulations and a rapid prediction of the cooling performance at each rotor speed.

4.5. Thermal analysis of WSFM for traction applications

This section presents a 2D FE thermal model of the WFSM for traction applications described in Table VIII. The analysis initially focuses on heat transfer within the rotor, followed by a comprehensive examination of the entire machine in the 2D domain. Both analyses are conducted under base operating conditions, with the machine running at *6000 rpm*. Pre-processing and post-processing of the thermal models are carried out using Altair Flux software.

4.5.1 Pre-processing 2D rotor model

The aim of this model is to predict the heat flux in the rotor and determine its maximum power heat transfer capability at *6000 rpm*. Figure 4.16 illustrates one pole of the rotor, highlighting several critical details essential for accurate thermal management.

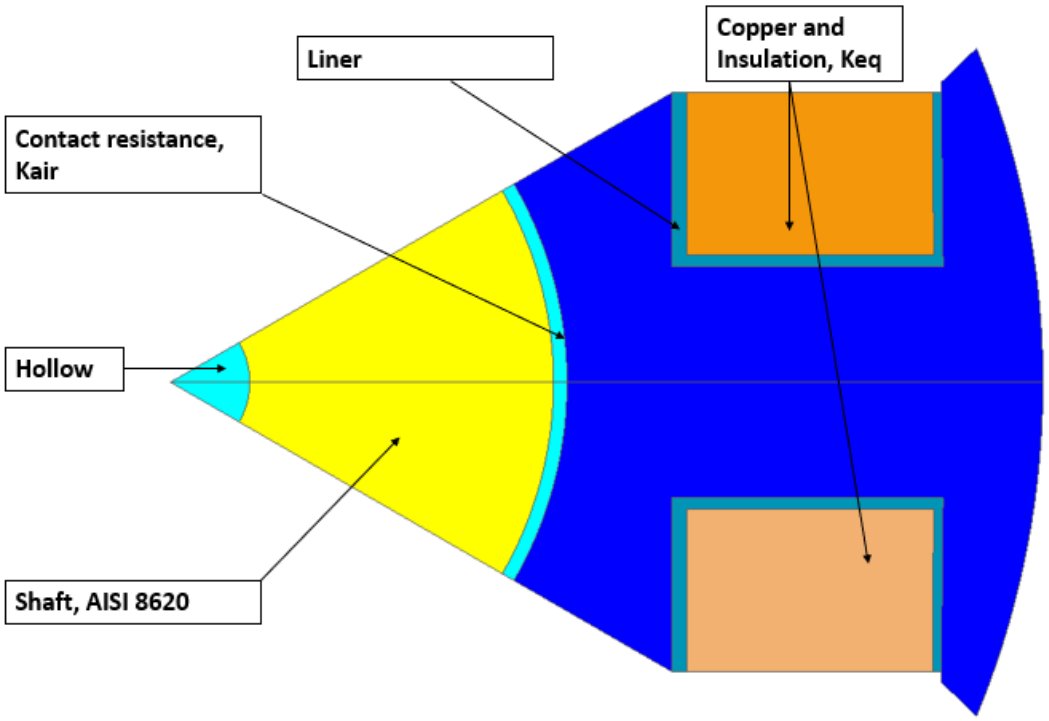

Figure 4.16 - 2D Rotor thermal FE model

Key parameters for predicting conductive heat transfer include:

- Keq_air = *0.024 W/mK*: The equivalent thermal contact resistance in regions with air, a highly sensitive parameter influenced by surface roughness and contact pressure.
- K_{8620} = *37 W/mK*: The thermal conductivity of the steel used in the shaft.
- Keq,cu = *0.77 W/mK*: The equivalent thermal conductivity of the windings, considering a fill factor of *0.65*. It accounts the presence of insulation in the winding.
- K_{NO20} = *21 W/mK*: The thermal conductivity of NO20, used in both the rotor and stator cores.
- K_{NOMEX} = *0.11 W/mK*: The thermal conductivity of NOMEX, used as an insulation material in the liner.

The model replicates the cooling effect of an axial fan and an oil-flooded hollow shaft on the rotor, with appropriate HTCs defined for each boundaries. At the rotor's top surface, an HTC of h = *181.2 W/m²K* at *25°C* is applied, derived from correlation (11), while along the hollow shaft, h = *320 W/m²K* at *40°C* is used, based on correlation (13). In the winding region, an HTC of h = *100 W/m²K* is specified.

4.5.2 Post-processing 2D Rotor model

The objective of the model is to evaluate the maximum heat dissipation capacity of the rotor, cooled by both the fan and hollow shaft. A maximum allowable temperature of *180°C* is set as a boundary condition, assuming an insulation class "H". For a 6-pole machine, the 2D thermal model estimates that the cooling solution allows a maximum dissipated power of *570 W*. Figure 4.17 provides a temperature distribution map of the model.

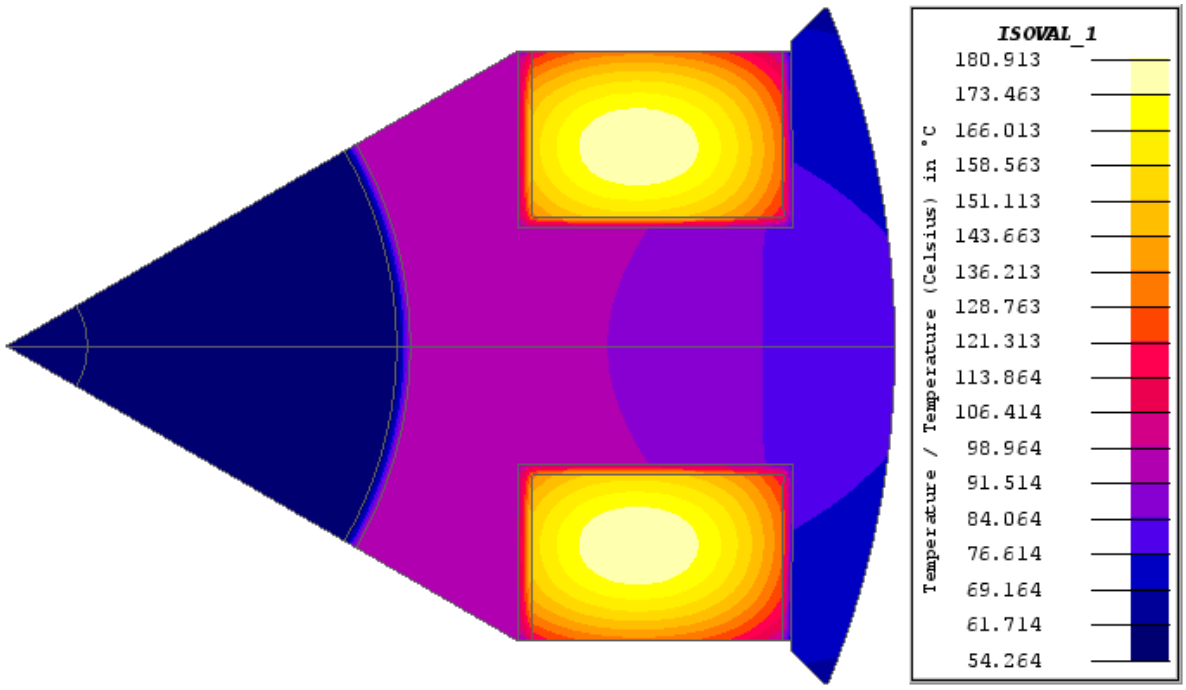

Figure 4.17 - Temperature map of one pole of the Rotor

It is also crucial to analyse the heat flux within the rotor to identify the primary cooling mechanism. Figure 4.18 illustrates the heat flux vectors, revealing that the active cooling solutions significantly impact the rotor's thermal management. The results clearly indicate that the heat flux directed toward the air gap ensures that active cooling via a fan is the most effective cooling method, as confirmed by the simplified model.

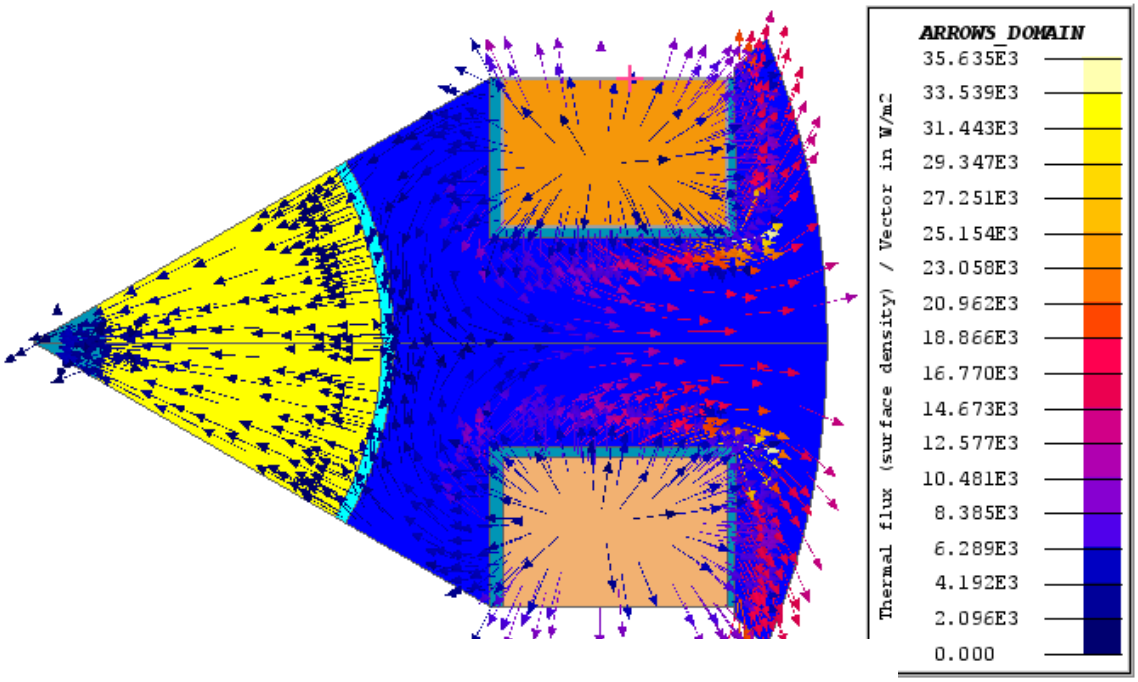

Figure 4.18 - Thermal flux map of one pole of rotor in 2D thermal model

4.5.3 Pre-processing 2D WFSM thermal model

The model of a single pole of the 6-pole WFSM motor, leveraging symmetry, was built using Flux software, the same environment used for the electromagnetic model. The machine's specifications are listed in Table VIII. The rotor and stator cores are made of N020 steel, while copper is used for the windings. An equivalent thermal conductivity has been defined to account for the combined presence of copper and insulation material in the rotor windings, as illustrated in Fig. 4.19. In the stator, the design includes eight layers of hairpin windings, with impregnation, wedge, and slot opening features modelled as depicted in Fig. 4.20.

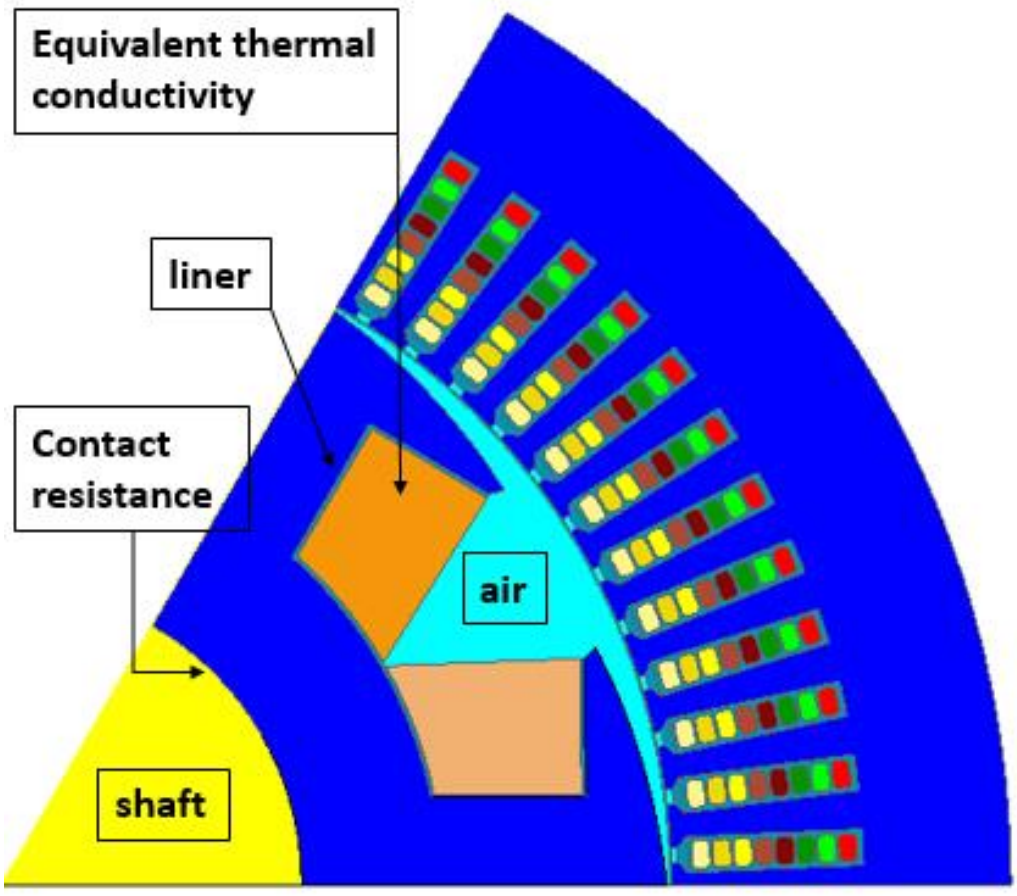

Figure 4.19 - 2D Thermal model of one pole of WFSM for traction applications

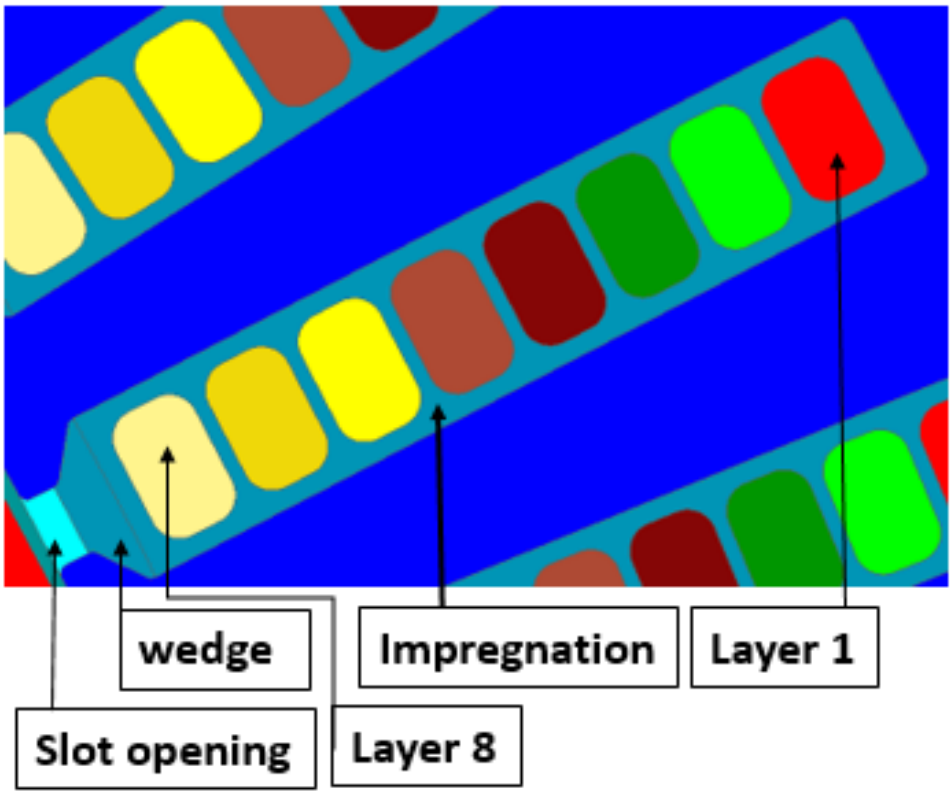

Figure 4.20 - Zoom of stator winding of the 2D thermal model

The stator model focuses on heat transfer through conduction within the stator slots, as well as convection with air in the air gap and water in the case, as the stator is cooled by a water jacket. To accurately assess the motor's temperature, thermal coefficients are defined for each region, following the values used in the 2D rotor model for the same materials. For the wedge and impregnation regions of the stator, a thermal conductivity of $K_{impregnation}$=*0.2 W/mk* is applied.

The cooling system consists of a water jacket for the stator and a fan generating axial airflow at 6 m/s to cool the rotor. To replicate this system, appropriate heat transfer coefficients are defined: h_{rotor}= *200 W/m²K* at *80°C* for the top rotor boundaries, and h_{stator}= *2000 W/m²K* at *80°C* for the top stator boundaries.

The heat sources are derived from the electromagnetic losses evaluated in the 2D FE electromagnetic model, with resistivity values based on a winding temperature of *155°C* for the rotor and *263°C* for the stator. These temperatures were determined

through iterative coupling between the electromagnetic and thermal models, ensuring a stable temperature distribution. A breakdown of the losses in the machine at a base speed of *6000 rpm* is provided in Table IX.

TABLE IX: AVERAGE VALUES OF ELECTROMAGNETIC LOSSES

	Iron losses [W]	Ohmic Losses [W]
Rotor	3	153
Stator	57.5	348

4.5.4 Post-processing 2D WFSM thermal model

Figure 4.21 shows the resulting temperature distribution in the motor at base speed, with the hotspot located in the stator winding, exceeding *200 °C*. This temperature surpasses the limit for insulation class "H" i.e. *180 °C*. To address this issue, the stator winding's current density could be reduced by revising the electromagnetic design. Alternatively, a more aggressive cooling solution, such as spray cooling for the stator coils, could be considered.

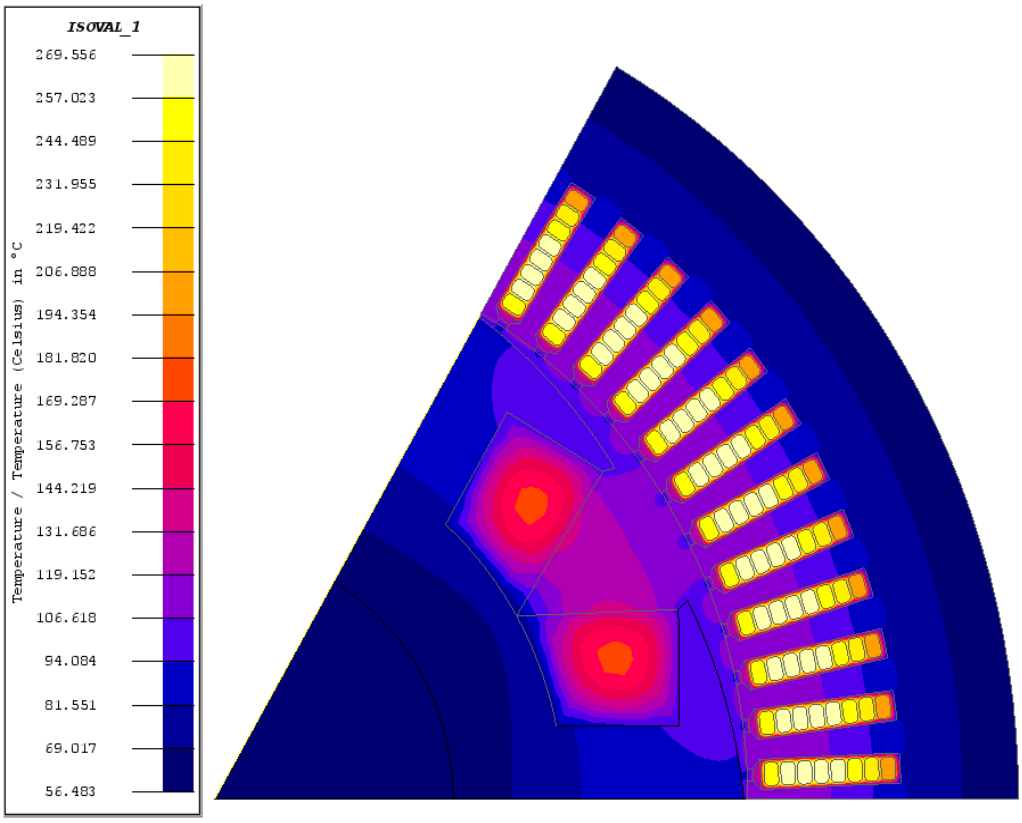

Figure 4.21 - Temperature distribution from 2D thermal model

4.6. Conclusions and Observations

This work presents a methodology (design flow) for assessing power loss handing capability of alternative rotor assemblies commonly found in electrical machines. The proposed simplified TEC-based approach allows for a rapid evaluation of the rotor heat removal capability for a set of predefined operating conditions like maximum allowable rotor temperature, type of coolant, coolant temperature and mass flow. As the model uses a combination of theoretical and empirical correlations derived for simplified geometries, it is recommended to use the model in conjunction with a high fidelity CFD model or experimental data for a more detailed analysis. The proposed methodology has been demonstrated on a case study high-speed salient-pole WFSM for traction applications. A set of alternative rotor cooling scenarios was evaluated showing that active cooling involving passing air through the rotor body offers here the best performance. The improved heat removal leads to significant performance gains over the entire torques speed envelope of the analysed motor. Note that the analysed baseline motor relies on the rotor induced (passive) cooling only with limited heat removal capability at lower motor speeds, in particular. However, the active motor/rotor cooling comes at an expense of higher complexity of the motor and thermal management system, and mechanical power losses due to aerodynamic and/or fluid churning effects. These however can be addressed by the appropriate sub-systems integration and ‘intelligent’ thermal management, all of which will be investigated by the authors as a continuation of this work.

4.7. Contributions to research

The results of this chapter are reported in one academic publication in a high profile electrical machines conference. The full publication citation is listed below:

- A. Guiducci, S. Nuzzo, D. Barater, G. Franceschini and R. Wrobel, "Thermal Modelling of Advanced Rotor Cooling Solutions for Traction Applications," 2024 International Conference on Electrical Machines (ICEM), Torino, Italy, 2024, pp. 1-7, doi: 10.1109/ICEM60801.2024.10700224.

5. FATIGUE MONITORING OF PEEK MATERIAL

This chapter presents an experimental study conducted by the author during a six-month secondment at Montanuniversität Leoben, Austria, as part of the Mechanical Research Group. The study focuses on predicting the failure of specimens made from PEEK, a widely used material for slot and linear insulation in electrical machines and many other applications. By analysing the current, voltage, force and acceleration data from an electrodynamic shaker, the research aims to development of time-and frequency-based methods, which allow an early detection of damage during stress-controlled fatigue experiment.

5.1. Introduction

Researchers have been investigating the phenomenon of material fatigue [142] for more than 150 years. Fatigue is described as a three-step process comprising crack initiation, crack propagation and the final fracture caused by varying loads. The fact that fatigue occurs at much lower macroscopic loads than the elasticity limit for example, have led to many new findings in research throughout the decades. Wöhler carried out the first tests in the 19th century and defined a fatigue limit (constant amplitude limit) between 10^6 and 10^7 cycles, which was mainly initiated by the railway industry. Loads below the fatigue limit result in an infinite life of the components, when reaching 10^7 cycles without failure [143–145]. For many years, various models [146] have suggested that material damage cannot occur below the fatigue limit, a concept that is still widely incorporated into general descriptions. Testing time was limited up to some 10^6–10^7 cycles. Because of economic reasons, new approaches for material testing were developed as a consequence of increasing requirements of new applications in the railway, automotive and aircraft industry [147]. The most common testing technique for actual investigations in the very high cycle range (10^7 -10^{10}) is the usage of ultrasonic testing equipment. Several previous investigations performed by Stanzl-Tschegg [148], Mayer [149], Marines-

Garcia [150] and Bathias [151] have given a broad overview. Besides the ultrasonic testing devices (up to *40 kHz*) there are other setups as well mentioned in [148] reaching testing frequencies from *20 Hz* up to *1.8 kHz* [151–156].

This work presents a novel high-frequency fatigue testing method, capable of operating at frequencies up to *4000 Hz*. Existing testing systems are limited to frequencies of up to *30 Hz* (servo-hydraulic) and *200 Hz* (electromechanical), making tests up to 10^9 cycles inefficient and uneconomical. The development of this new method is driven by several key requirements, including higher testing frequencies (around *1 kHz*), flexibility in both setup and specimen design, and the ability to test both standard specimens and component-like samples. To meet these demands, an electrodynamic shaker system is selected, and a specialized oscillatory test setup is designed. The aim is to excite the system at its resonant frequency using the shaker, leveraging the amplification of the excitation signal to induce high loads within the specimen.

5.2. Electrodynamic shaker identification and modelling

Electrodynamic shakers have the advantages of being relatively inexpensive, simple to control, and have approximately linear behaviour, and are widely used in vibration tests. As shown in Figure 5.1, the core of the shaker is the coil, which is wound around a stiff thin-walled tube and forms the coil form.

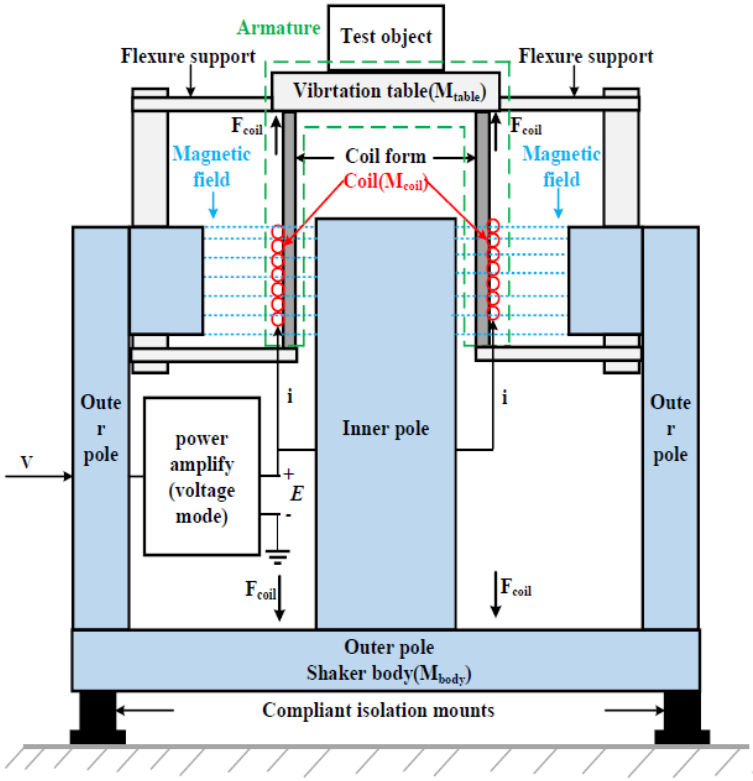

Figure 5.1 - The structure of the electrodynamic shaker [157]

The coil form is suspended in a magnetic field between the inner pole and the outer pole, one end of the coil form is attached directly to the vibration table, and the other end of that is attached to a compliant disk. The shaker adopts these flexure supports to keep the coil form concentric between poles and restrain any out-of-plane moments applied to the vibration table. When the current flows through the coil, a force F_{coil} is produced in proportion to the current i and is transmitted to the test object, which is affixed to the vibration table. By reaction, the force F_{coil} is also operated on to the shaker body. Meanwhile, as the coil moves axially in the magnetic field, a back-emf $U_{backemf}$ is generated in proportion to the velocity across the coil and reflects the mechanical activity into the electrical domain, which means a "two-way street" between the mechanical and electrical parts and these two are coupled. The power amplifier has two operation modes: voltage and current. In the former mode, E is related to the input voltage V, in which the current i flowing into the coil depends on the mechanical movements. This leads to evident electromagnetic damping when the movement of the armature exhibits a maximum around the resonance frequency. In the latter mode, the output of the amplifier is the current i. For the current independent of the $U_{backemf}$, the mechanical movement of the shaker affects V, which means that there is no electromagnetic damping effect. The vibration shaker applications typically adopt the voltage amplifier.

Figure 5.2 depicts the electrical part, and we should account for the resistance *R*, and the inductance *L* of the coil, and *Uemf* is the back-emf coefficient of the shaker. The mechanical part is ignited by force F_{coil} proportional to the current *i* of the electrical part. Meanwhile, the electrical part is excited by the back-emf $U_{backemf}$ proportional to the coil velocity of the mechanical part. Therefore, these two parts are cross-coupled, and the small shaker is a 3 DOFs coupled system. It works as a linear motor.

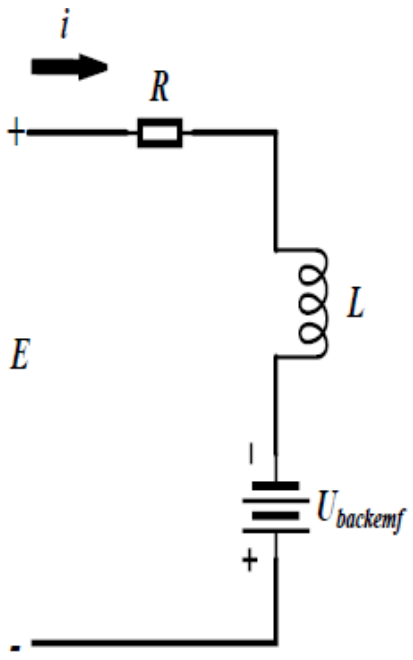

Figure 5.2 - Equivalent Electric Circuit

5.2.1 Identification

To identify the characteristics of the electrodynamic shaker, the experiment is conducted without a specimen as shown in figure 5.3. The goal is to compare the transfer functions obtained from the data acquisition system of the shaker with those estimated using MATLAB, both under an acceleration of *200 m/s²*. Five tests are performed, covering a frequency range from *20 Hz* to *4000 Hz* in both upward and downward sweeps.

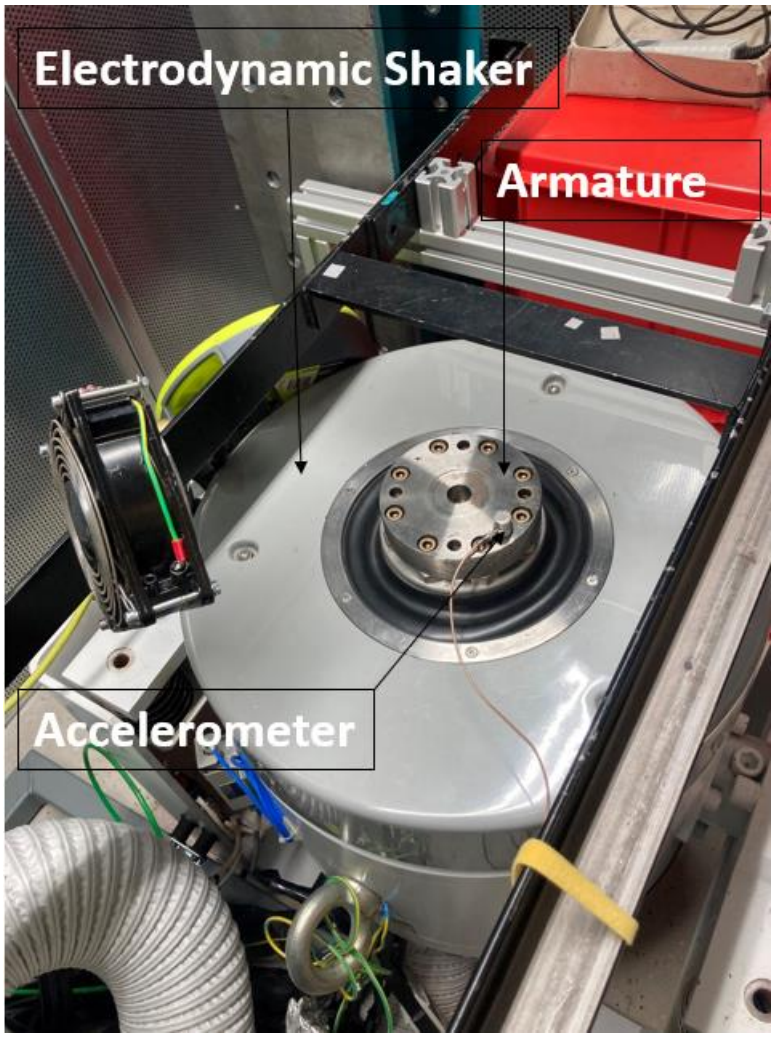

Figure 5.3 - Electrodynamic shaker

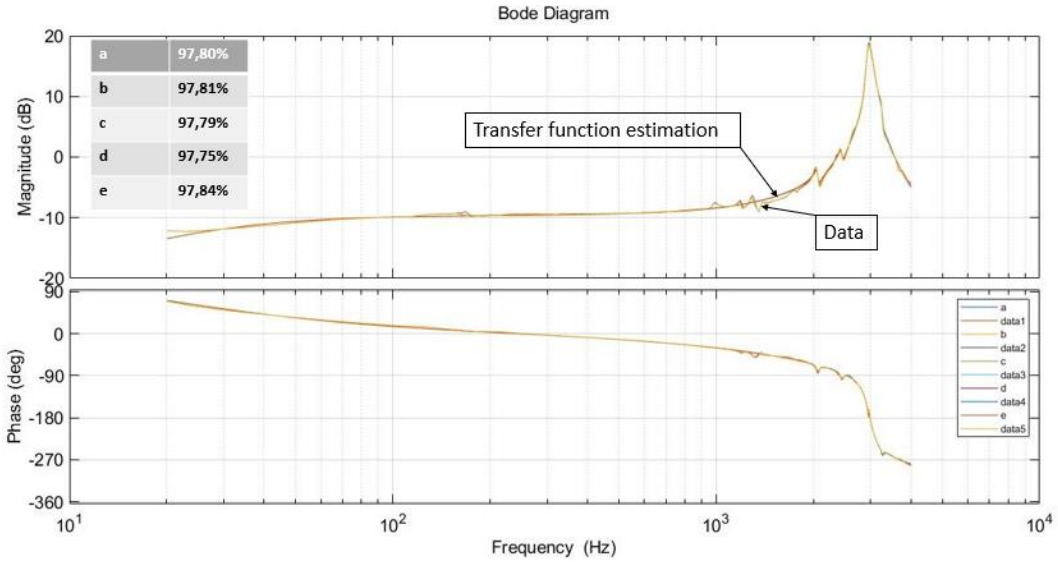

Figure 5.4 - Comparison between transfer function estimation and data acquisition system from 20 Hz to 4 kHz

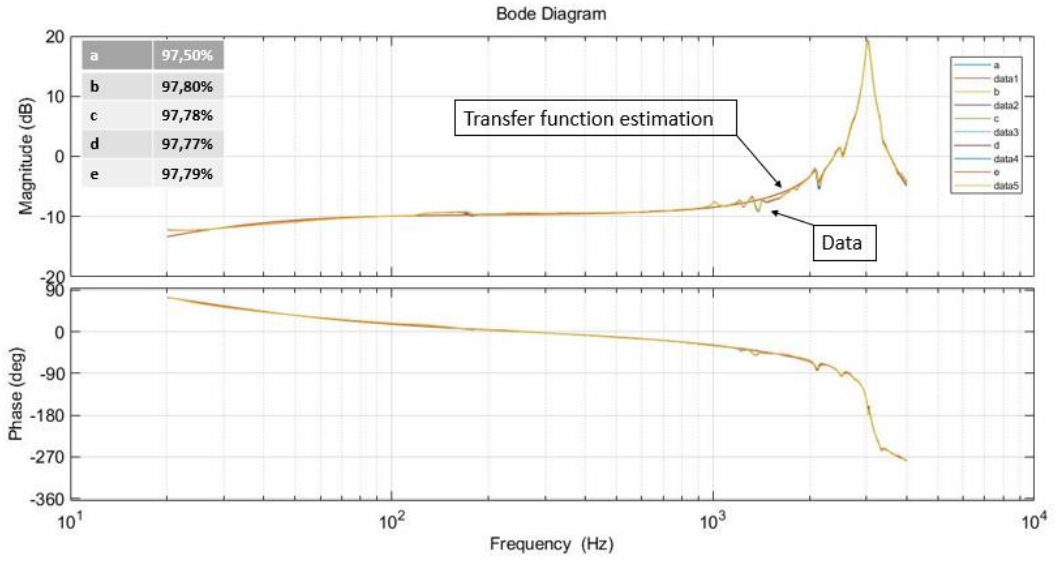

Figure 5.5 - Comparison between transfer function estimation and data acquisition system from 4 kHz to 20 Hz

The analysis begins by considering the transfer function from the shaker software, $F(s) = a / V$, and the phase date for each experiment.

The first step is to decompose *F(s)* into a complex signal, then create a frequency-response data model in Hz and subsequently generate the transfer function from the complex signal. Finally, *F(s)* is compared with the transfer function estimated in MATLAB, as shown in Figure 5.4 for the upward frequency sweep (*20 Hz* to *4000 Hz*) and in Figure 5.5 for the downward sweep (*4000 Hz* to *20 Hz*). The table in each figure demonstrate a strong agreement between the transfer functions.

5.3. PEEK material

High performance polymers have further expanded its technological lead in the high-performance polymers sector with PEEK compounds. It is particularly suitable for applications in which extremely high mechanical, thermal, and chemical requirements must be met. These compounds are particularly characterised by the following material properties:

- Very high heat resistance
- High rigidity
- Lower water absorption and therefore high dimensional stability
- High hardness
- Good strength
- Excellent sliding friction behaviour, minimal abrasion
- Good electrical characteristics
- Excellent chemical resistance
- Excellent hydrolytic stability
- Good processability
- Low tendency to form stress cracks

To meet the requirement of different applications, manufactures can adjust the properties of pure PEEK selectively by adding various additives:

- Processing aids facilitate demoulding.
- Fillers and reinforcing materials increase rigidity and dimensional stability upon exposure to heat. Chopped carbon fibres are most effective for this. Minerals and glass microbeads also counteract the tendency to wrap.

PEEK compounds can be used for a wide range of applications, such as in electrical, electronic, aerospace, railway, food, medical and automotive industries, as reported in Fig. 5.6.

The figure 5.6 highlights that PEEK compounds are an excellent choice for transportation applications, particularly in the electrical and electronic industries. This is due to their exceptional combination of properties, including thermal,

Figure 5.6 - Relevant properties of polyether ether ketone for industrial applications [158]

chemical, mechanical, and electrical field. Additionally, PEEK offers outstanding dimensional stability and processability, making it highly suitable for manufacturing and ensuring reliable performance in demanding environments.

In this thesis, we focus on PEEK specimens reinforced with *30%* glass fibers. For confidentiality reasons, a sketch of the PEEK sample is provided in figure 5.7. This material is primarily used in insulation systems for electrical machines as shown in Figure 5.8 and rotor retention systems.

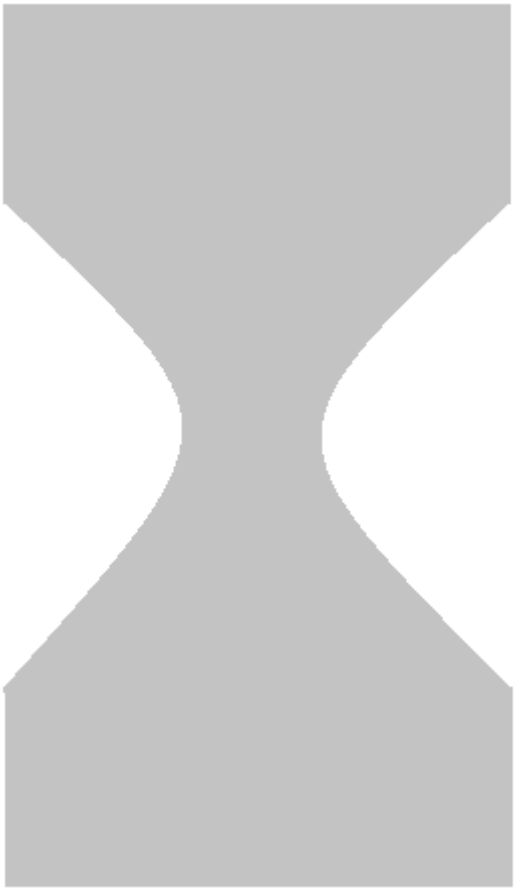

Figure 5.7 - Sketch of 30% Glass Fibers Reinforced PEEK specimen

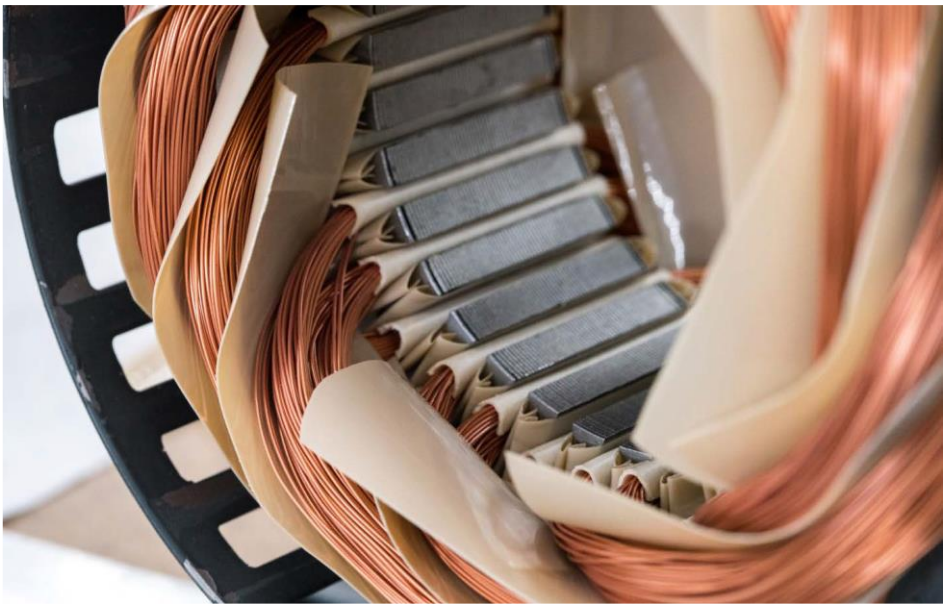

Figure 5.8 - Completed stator winding with PEEK magnet wire, PEEK slot insulation and PEEK phase insulation

PEEK materials are specifically designed to address the unique challenges of rotor and stator applications in electrical machines. Primarily used to insulate the slot between motor windings and metal laminates, slot liners and bobbins also serve as containers for stator windings, providing rigidity, shape retention, ease of assembly, and protection from damage and vibration during both assembly and operation.

The more rigid PEEK magnet wire offers greater resistance to coil movement during start-up, surge, and similar scenarios. PEEK material demonstrates superior tear resistance and maintains its shape when installed as slot insulation, including cuff formation. While the PEEK wire is stiffer than standard magnet wire, making its installation into the slot slightly more challenging due to its reduced ability to retain bends. However, for use as slot liner, installation of the PEEK is comparable to the installation of the standard Nomex® [154]. After resin impregnation, follow-up electrical testing shows no significant partial discharge (PD) activity [159].

Engineered plastics are heavily influenced by filler reinforcements. Although unfilled polymers typically have a thermal conductivity of ~ *0.2 W/mK*, the appropriate choice of fillers can significantly increase this value.

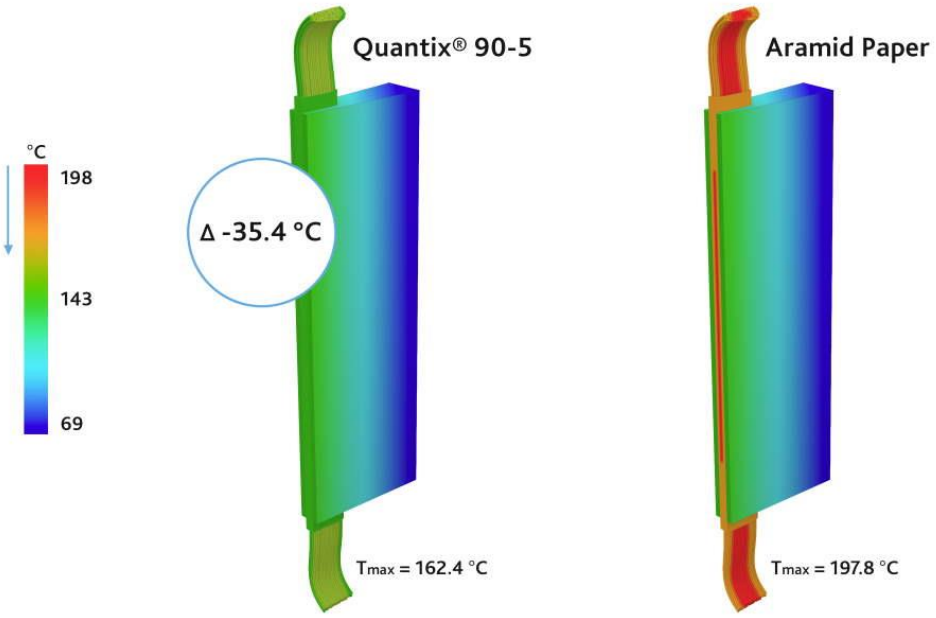

Figure 5.9 - Thermal advantage of PEEK material respect Aramid paper [160]

Szparagowski and a team of material experts have successfully developed several material grades that enable PEEK compounds to offer a customized solution that can be matched to specific application requirements. Each grade offers a unique blend of material characteristics such as tensile strength, elongation, electrical and thermal properties, that are achieved by adjusting the filler. Quantix 90-5, for example demonstrates high thermal conductivity of *0.6 W/mK* through plane and *4W/mK* in-plane. Extensive material testing confirms the material's superior thermally conductive while maintaining high, electrically isolating properties (volume resistivity of $2\ x10^{14}\ Ohm{\cdot}cm$). As a result, these materials help designers enhance electric motor performance by improving thermal management. The reduced internal temperatures within the electrical machine can provide several key benefits, including increased motor power density, simplified cooling strategies, and extended lifespan, as both winding enamel and potting materials tend to degrade at higher operating temperatures [160].

5.4. Testing procedure

To better understand the functionality, the equipment, measurement technology, and developed testing components used in this study are presented below. The testing setup is integrated with an electrodynamic shaker system to perform high-frequency fatigue tests. Various high-frequency testing methods exist, including servo-hydraulic, electromagnetic, and ultrasonic test rigs. In this case, an electrodynamic shaker is chosen with the goal of developing a setup capable of testing at frequencies up to approximately *1 kHz*. Similar setups are proposed by Yun [161] and George [162].

5.4.1 Shaker system

An electrodynamic shaker i210 (IMV Europe Ltd.) has been installed at the Department of Mechanical Engineering at the Montanuniversitaet Leoben. The system arrangement, excluding the blower which is installed for cooling the shaker body, is displayed in Fig. 5.10.

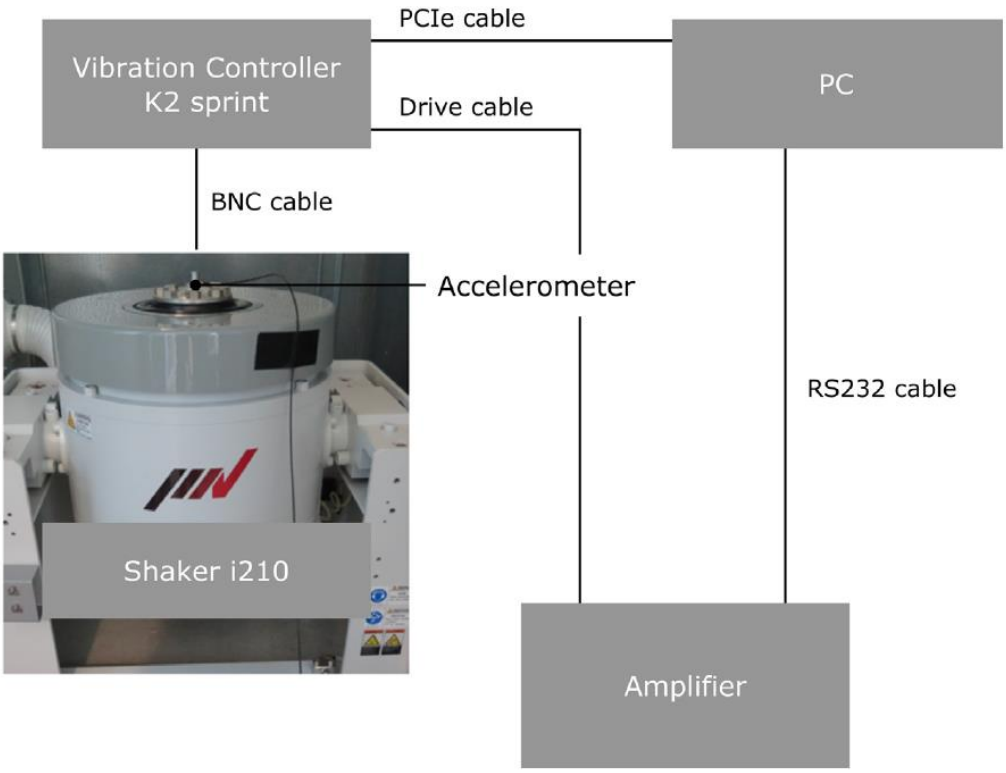

Figure 5.10 - Description of the arrangement and components of a common shaker system IMV i210

The shaker itself (Shaker i210) is built out of a field coil and a drive spool. These electrical components are covered under a steel casing. The armature is supported by air suspensions and centred by an upper support system. The whole body is supported by an additional air suspension where vibrations are decoupled from the ground. An oscillating force is provided by Fleming's left hand rule where a force is caused by the flow of electric currents perpendicular to a magnetic field. The system is capable of testing up to maximum *4000 Hz*. The shaker armature has a weigth of *3 kg*, a diameter of *128 mm* and a maximum acceleration of *1000 m/s*^{2} is reachable. A maximum force of *3 kN* can be achieved in SINE (sine signal) mode while acceleration a is limited by Eq. (14). With increase of m the reachable a decreases and limits the performance of the shaker.

$$F = m\,a \tag{14}$$

The amplifier, as the name suggests, serves for amplification of electric signals. The shaker is capable of running in different modes like SINE, RANDOM and DWELL. For example the SINE mode describes an operation mode where a sine shaped acceleration (or equal value) signal is performed by the shaker armature. The vibration controller K2 sprint is responsible of processing accelerometer signals. At least one external accelerometer is needed to maintain the internal control loop (closed loop system) of the shaker.

5.4.2 System operation

Operation of the shaker was established by the K2 operation software. Dependent on the actual drive mode (SINE, RANDOM, DWELL) certain settings have to be adjusted to ensure proper operation. The functionality of the software is described by the IMV manual in detail. As displacement, velocity and acceleration values are equivalent they can be adjusted in a certain range dependant on the frequency.

5.4.3 Test setup

A fan is used to cool the specimen during testing. The shaker is located in a climate chamber equipped with a ventilation system. The test rig set up is shown in fig. 5.11, where the specimen is clamped at both ends.

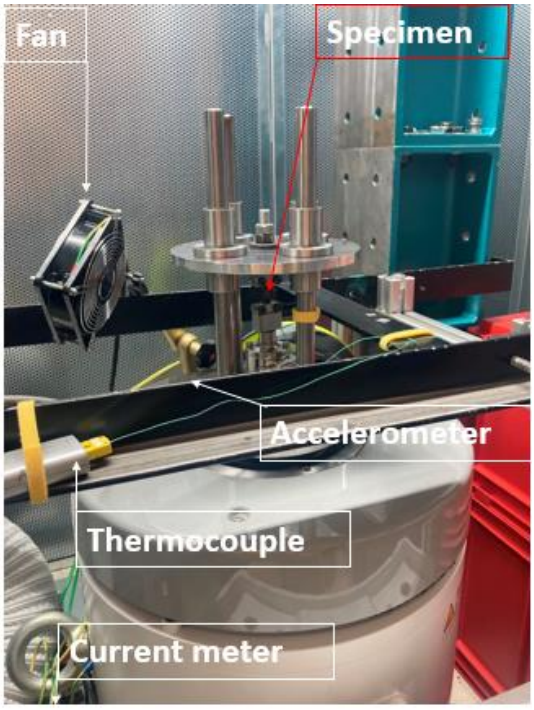

Figure 5.11 - Experimental test rig

Several tests have been conducted with applied loads of *350 N*, *400 N*, *450 N*, and *470 N* at a frequency of *230 Hz*, as shown in the table below.

Table X: Experimental tests

Test	Material	Force [N]	Frequency [Hz]
1	PEEK GF 30 - L	450	230
2	PEEK GF 30 - M	450	230
3	PEEK GF 30 - M	450	230
4	PEEK GF 30 - M	400	230
5	PEEK GF 30 - M	400	230
6	PEEK GF 30 - M	350	230
7	PEEK GF 30 - L	350	230
8	PEEK GF 30 - L	470	230
9	PEEK GF 30 - L	470	230
10	PEEK GF 30 - R	470	230
11	PEEK GF 30 - L	450	230

5.4.4 Measurement equipment

Accelerometers play a crucial role in continuously measuring and verifying vibration behaviour, providing valuable data on the stability and reproducibility of the vibration tests. The accelerometer used in this study is a Kistler 5128829. Additionally, a thermocouple is employed to monitor the specimen's temperature, while a current meter measures the input current to the electrodynamic shaker. The shaker itself is equipped with internal voltmeters and force meters for further monitoring.

5.5. Results

To post-process the experimental data, the initial step is to clean and normalize the data, focusing on the range from the start of the experiment after the transient trend to the point of failure. The root mean square (RMS) provides a clear view of trends in acceleration, current, voltage, and force in the time domain. Additionally, kurtosis is used to assess how prone a distribution is to outliers. Kurtosis formula is shown in the equation below as the ratio between the fourth central moment μ_4 and the standard deviation σ^4.

$$K = \frac{E\,(X-\mu)^4}{\sigma^4} = \frac{\mu_4}{\sigma^4} \qquad (15)$$

K=3, It means a normal distribution.

K >3, Distribution that are more outlier-prone than the normal distribution.

K<3, Distribution that are less outlier-prone than the normal distribution.

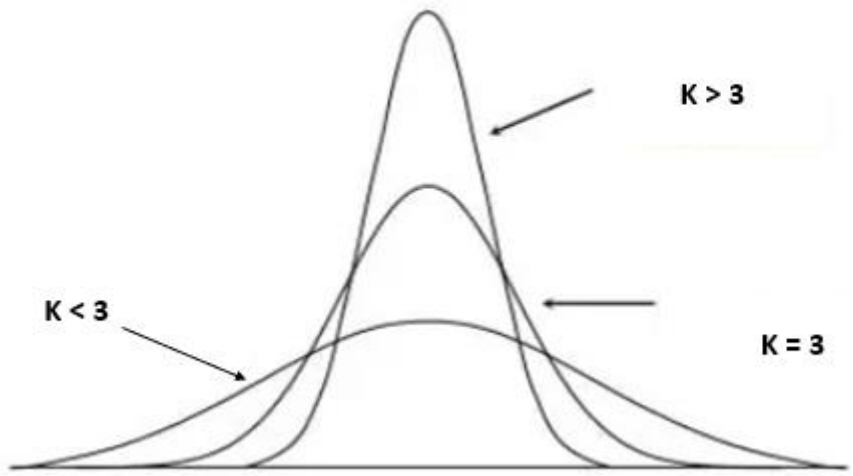

Figure 5.12 - Trends in explanations of Kurtosis

All the cases shown in table VII are post-processed and for a better understanding only case 6 at *350 N* and case 8 at *470 N* are reported and explained through an interpretation of data trend.

5.5.1 Case 6 - 350N – short term experiment

In case 6, the specimen was subjected to a *350 N* load and failed after *1026 minutes*, categorizing it as a short-term test.

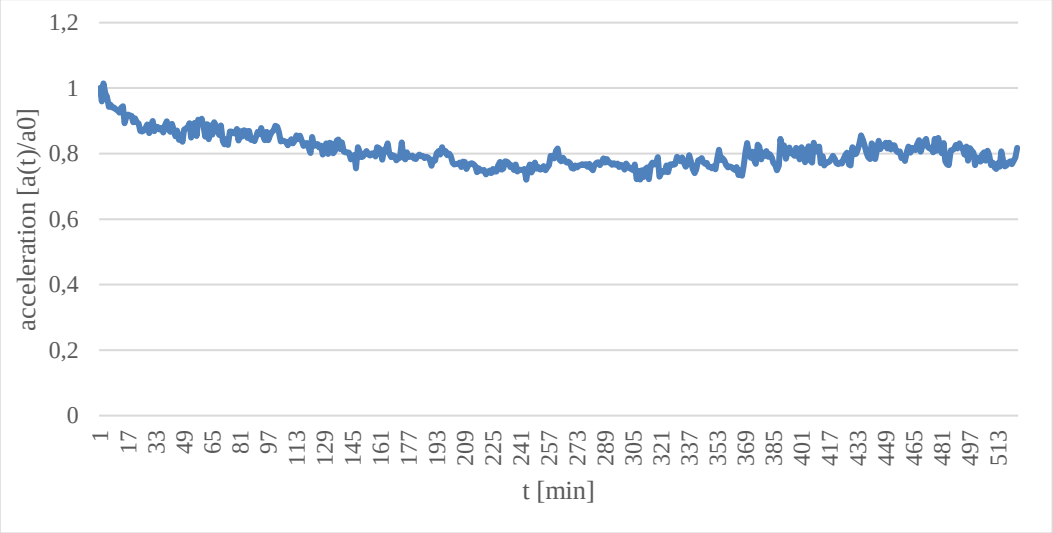

Figure 5.13 - Acceleration trend at 350 N of normalized data over time

Figure 5.13 illustrates the normalized acceleration trend over time, based on data from an accelerometer mounted on the shaker. The trend shows an initial decrease in acceleration, followed by stabilization with minor fluctuations until the specimen's failure. These fluctuations likely indicate small dynamic variations.

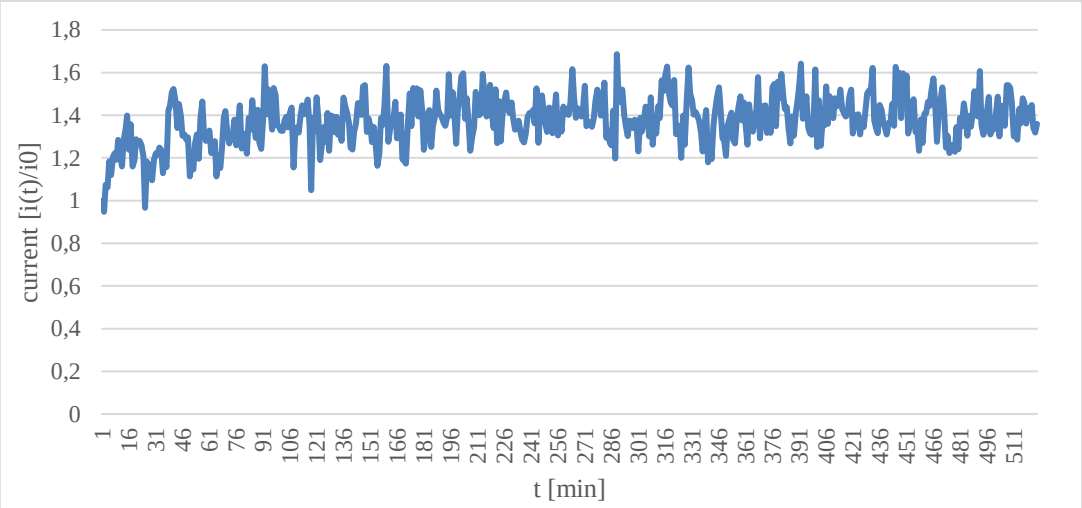

Figure 5.14 - Current trend at 350 N of normalized data over time

The current is measured using a meter connected to the shaker's power supply cable. Figure 5.14 displays the normalized current fluctuations over time, showing somewhat periodic oscillations with varying amplitude. These fluctuations likely represent the shaker's dynamic behaviour under load, possibly caused by the control system adjusting the current. The initial oscillations may indicate the system's attempt to reach a steady state, while the ongoing variations could reflect inherent system characteristics or external factors influencing the current.

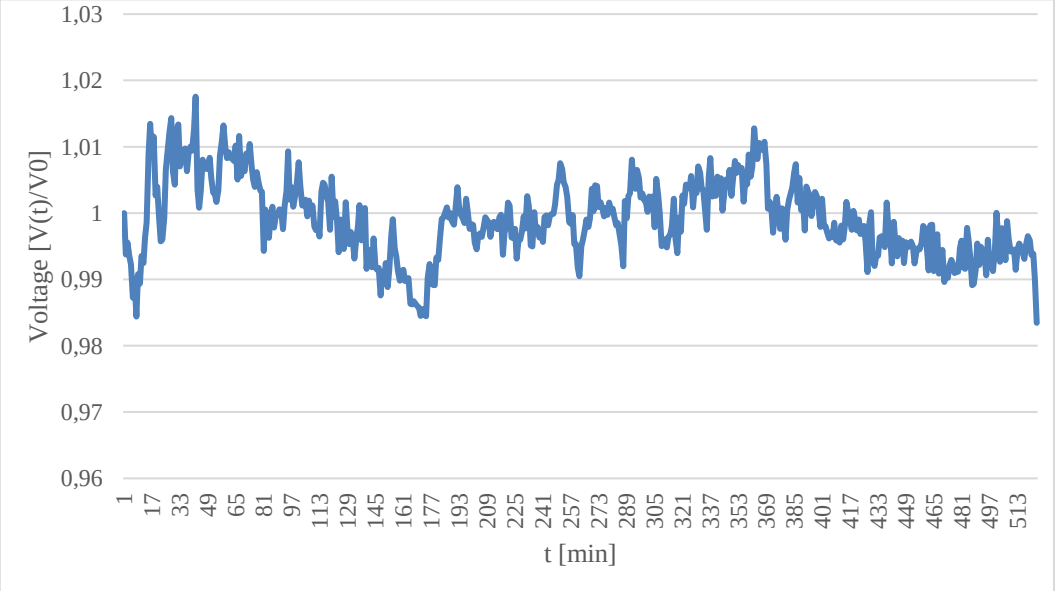

Figure 5.15 - Voltage trend at 350 N of normalized data over time over time

Figure 5.16 illustrates the normalized voltage fluctuations of the shaker, which remain within a narrow range over time. This behaviour indicates that the shaker operates with relatively stable voltage after an initial settling period. The minor fluctuations could be attributed to load variations.

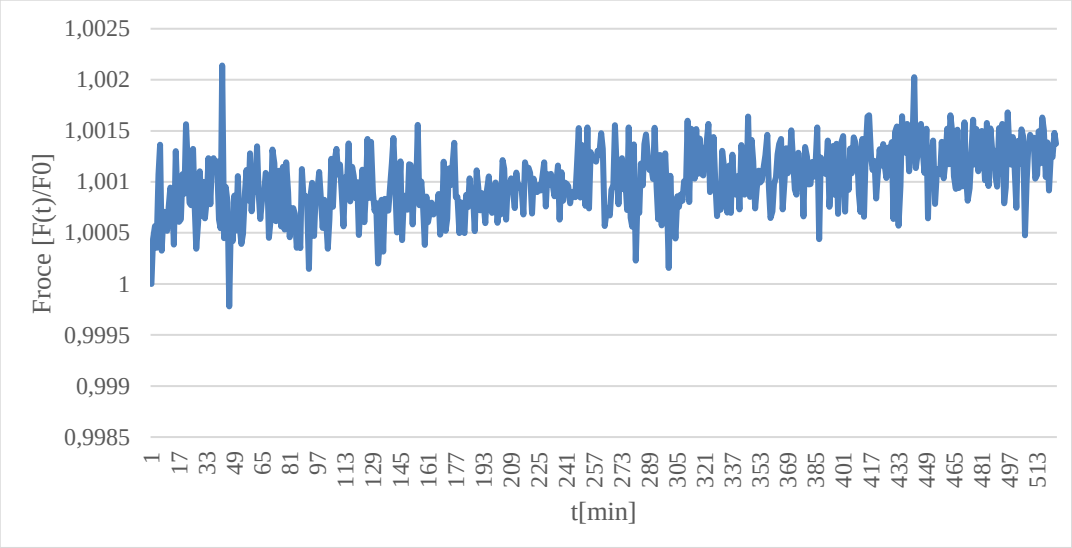

Figure 5.16 - Force trend at 350 N of normalized data over time

Figure 5.16 displays the normalized force oscillations within a narrow range over time. The force is applied as an input in the experiment, and the fluctuations arise from the shaker's control system as it works to maintain a constant force. As the specimen nears failure, the frequency of these fluctuations increases.

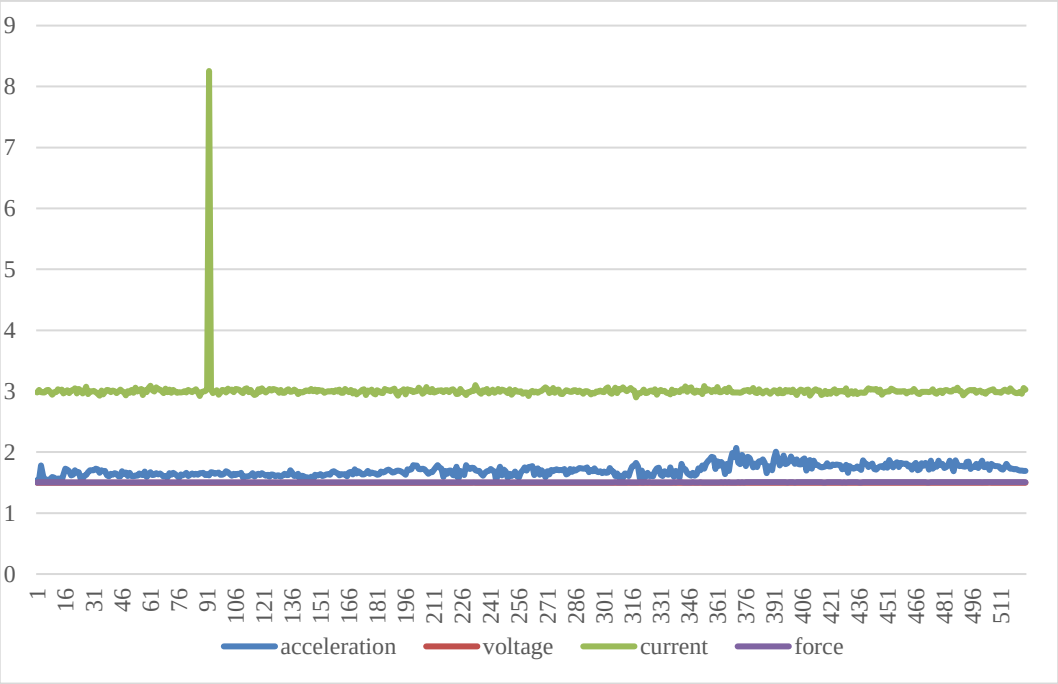

Figure 5.17 - Kurtosis trend of signals over time

Figure 5.17 illustrates the kurtosis of the signals. The current maintains a constant kurtosis value of *3*, indicating a normal distribution. In contrast, the acceleration, voltage, and force exhibit kurtosis values below *3*, suggesting their distributions are less prone to outliers compared to a normal distribution.

5.5.2 Case 8 - 470N – short term experiment

In Case 8, a load level of *470 N* was applied, and the experiment was conducted without activating the ventilation system inside the shaker's cabin. Failure occurred after *282 minutes*, categorizing it as a short-term test.

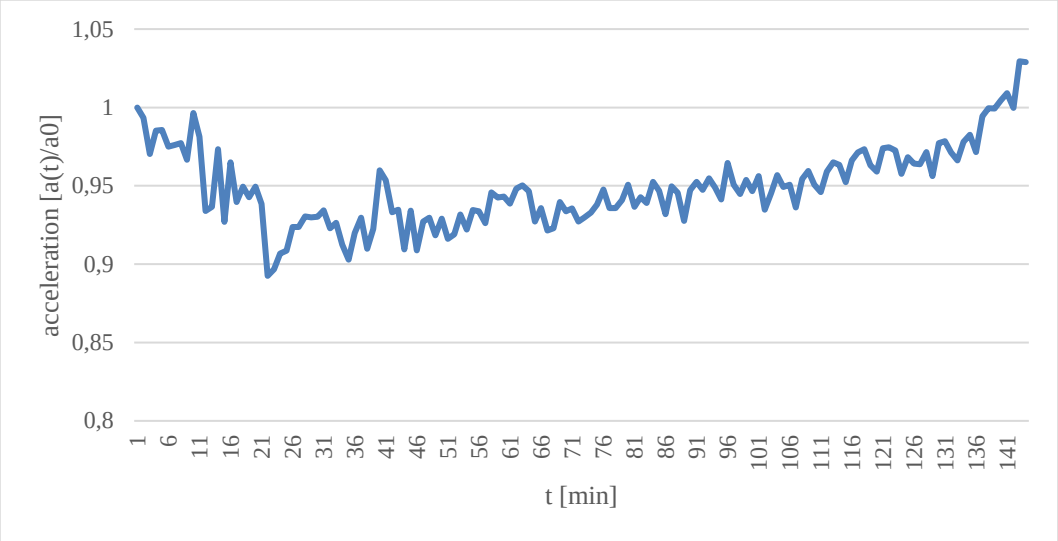

Figure 5.18 - Acceleration trend of normalized data at 470N over time

Figure 5.18 shows the normalized acceleration trend over time under a *470 N* load, based on data from an accelerometer mounted on the shaker. The curve reveals initial fluctuations in acceleration, followed by a stabilization phase, and then a noticeable increase as the specimen neared failure.

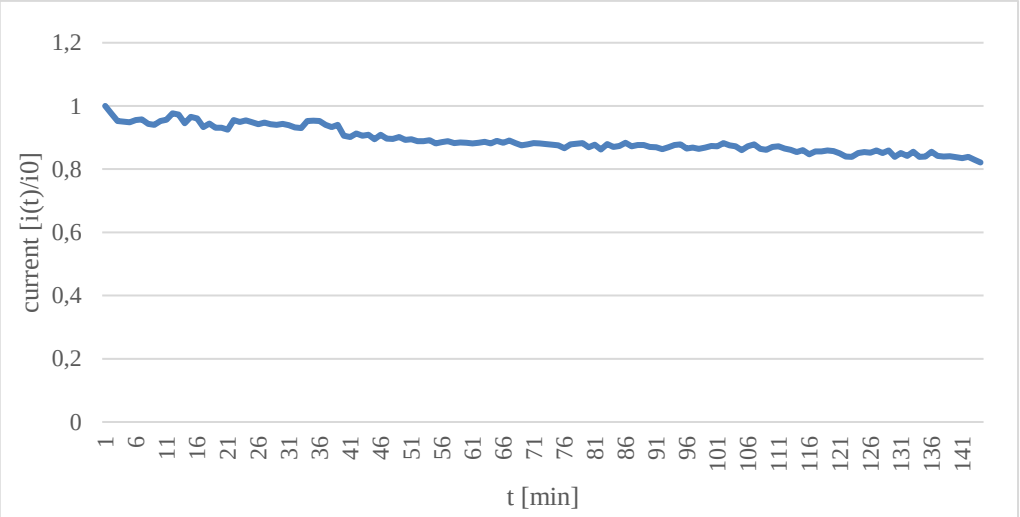

Figure 5.19 - Current trend of normalized data at 470N over time

The current was measured using a meter connected to the shaker's power supply cable. Figure 5.19 illustrates the normalized current fluctuations over time under a *470 N* load. The trend reveals a gradual decline in current, accompanied by minor fluctuations.

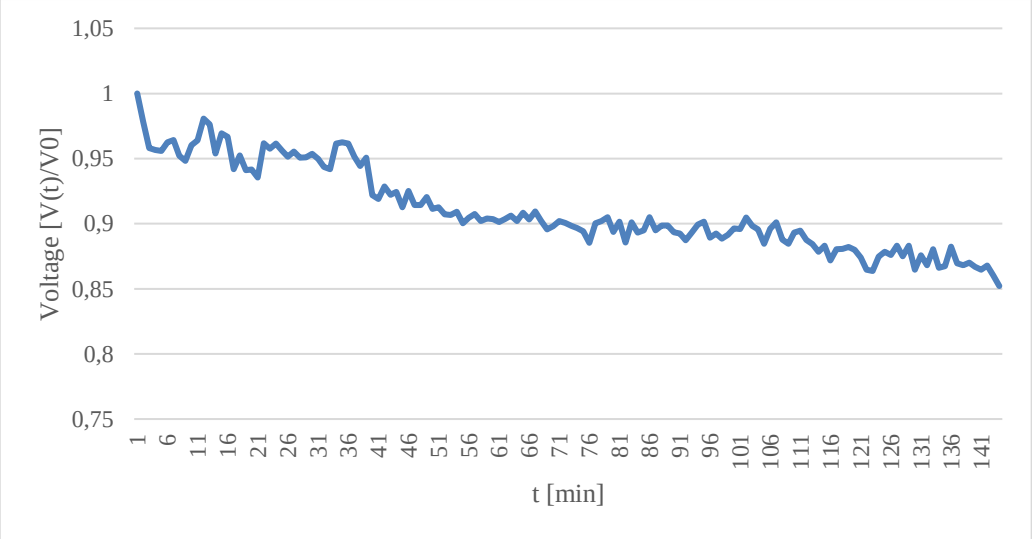

Figure 5.20 - Voltage trend of normalized data at 470N over time

Figure 5.20 shows the normalized voltage fluctuations of the shaker, revealing a steady decrease over time, mirroring the current trend in Figure 5.19. This suggests that the shaker draws less electrical power as the test progresses.

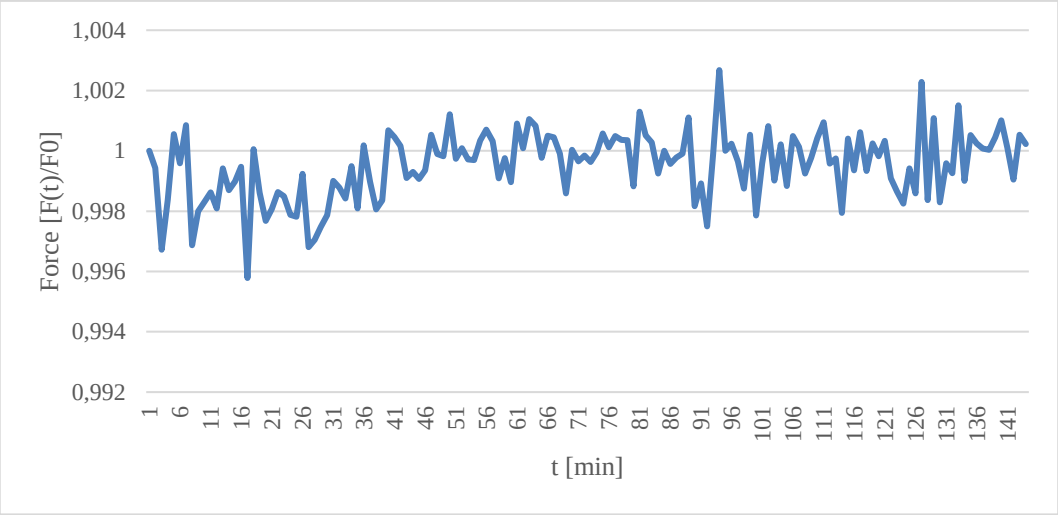

Figure 5.21 - Force trend of normalized data at 470N over time

Figure 5.21 illustrates the normalized force oscillations, which remain within a narrow range over time. The applied force stays relatively stable, exhibiting only minor fluctuations. As the specimen approaches failure, the force shows slight oscillations around the normalized value.

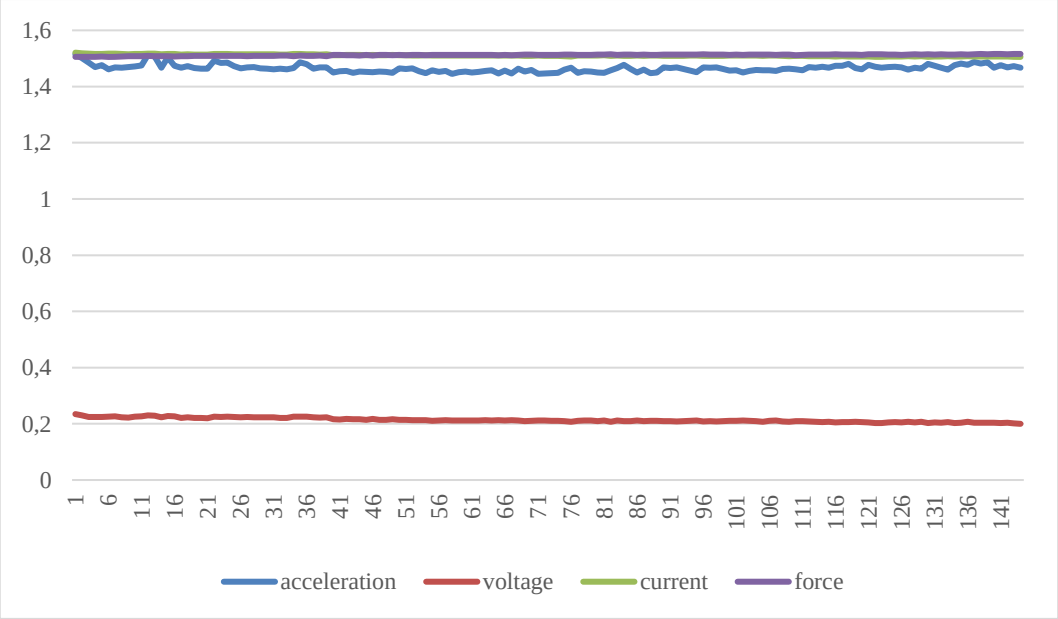

Figure 5.22 - Kurtosis trend of signals over time

Figure 5.22 illustrates the kurtosis of the signals. All measured signals—acceleration, voltage, current, and force—exhibit kurtosis values below *3*, indicating that their distributions are less susceptible to outliers compared to a normal distribution.

5.5.3 350N - long term experiment without failure of the specimen

At a load of *350 N*, the specimen did not reach failure. As shown in Figure 5.23, the RMS values of force, acceleration, current, and voltage remained constant over time. A similar trend is observed in the kurtosis measurements, as illustrated in Figure 5.24. This indicates that when the specimen does not experience failure, the signal trends remain stable over time.

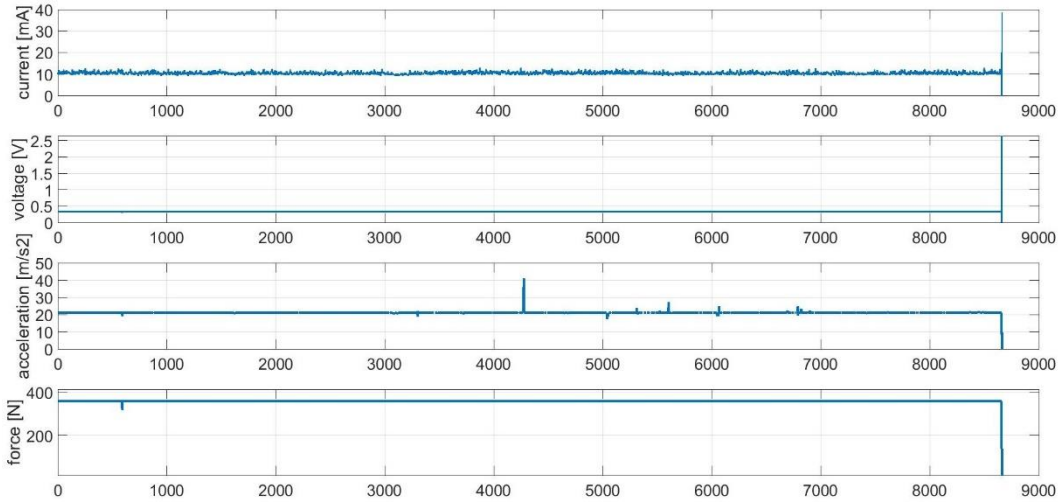

Figure 5.23 - RMS signals of long term experiment at 350N whit no specimen's failure

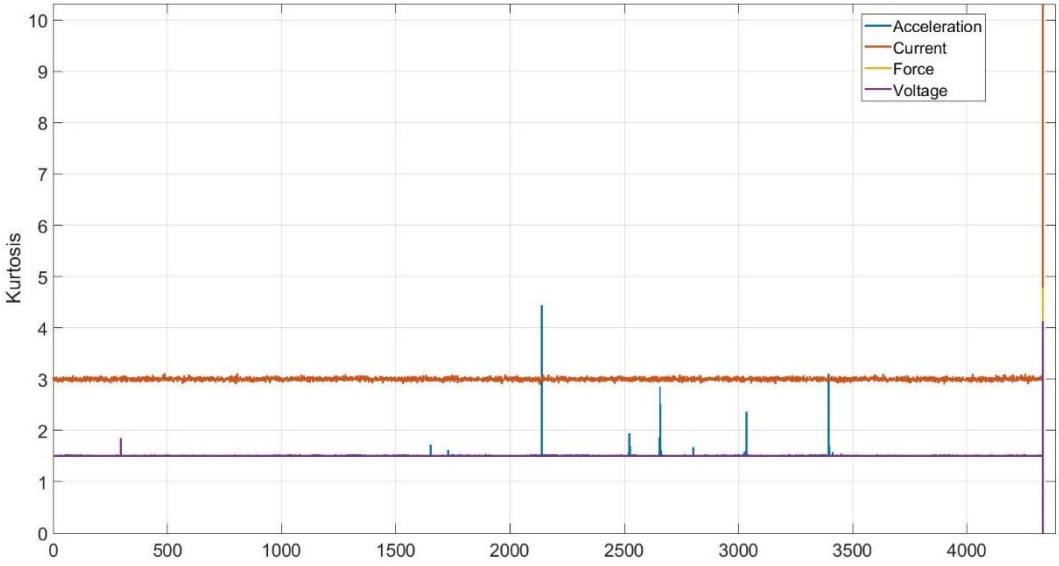

Figure 5.24 - kurtosis trend of the signals at 350N in a long term experiment with no specimen's failure

5.6 Conclusion

This work presents a new high-frequency vibration technique (HFVT) using an advanced electrodynamic shaker. Fatigue tests were conducted at 230 Hz with different loads: *350 N*, *400 N*, *450 N*, and *470 N*. For clarity, only three different cases are reported in the thesis, but each case has been thoroughly post-processed. Voltage serves as the primary signal, providing valuable insights throughout the test.

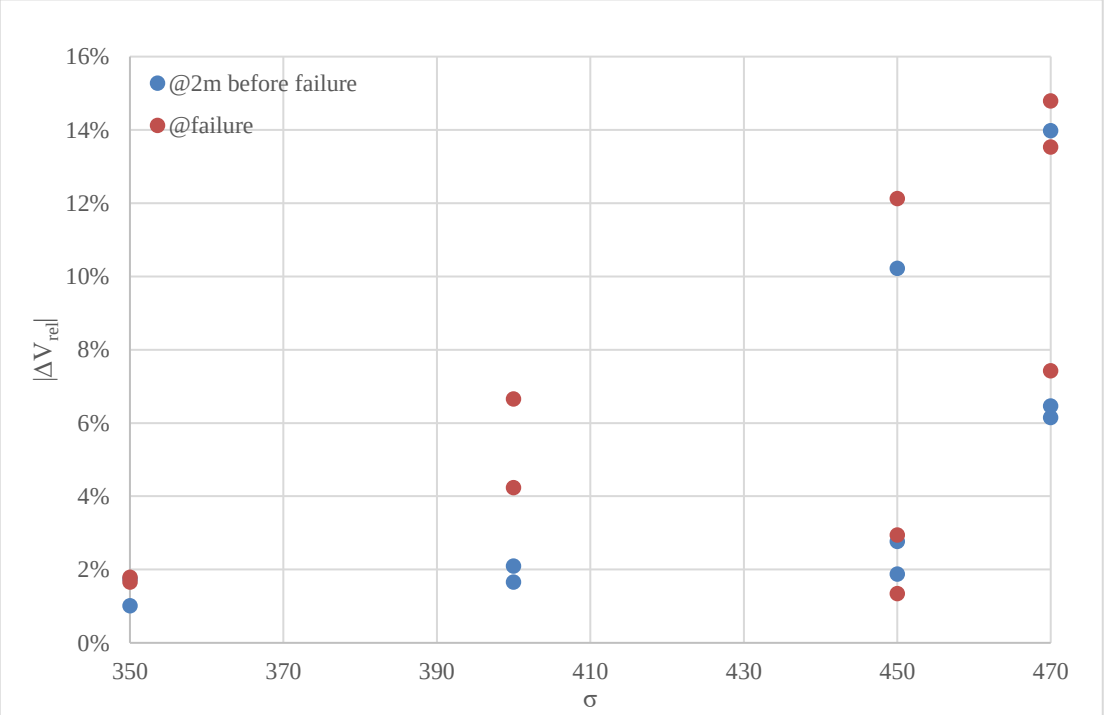

Figure 5.25 - Delta voltage vs load level at failure point and 2 minutes before the failure reference

Specifically, Figure 5.25 illustrates the voltage difference ΔV for each load case. The orange points indicate the percentage difference in voltage from the beginning of the test to the point of specimen failure, while the blue points represent the percentage difference from the start to two minutes before the specimen's failure. In both instances, the voltage increases as the load level rises. This leads to a key conclusion: ΔV is directly dependent on the load level, increasing proportionally with the load.

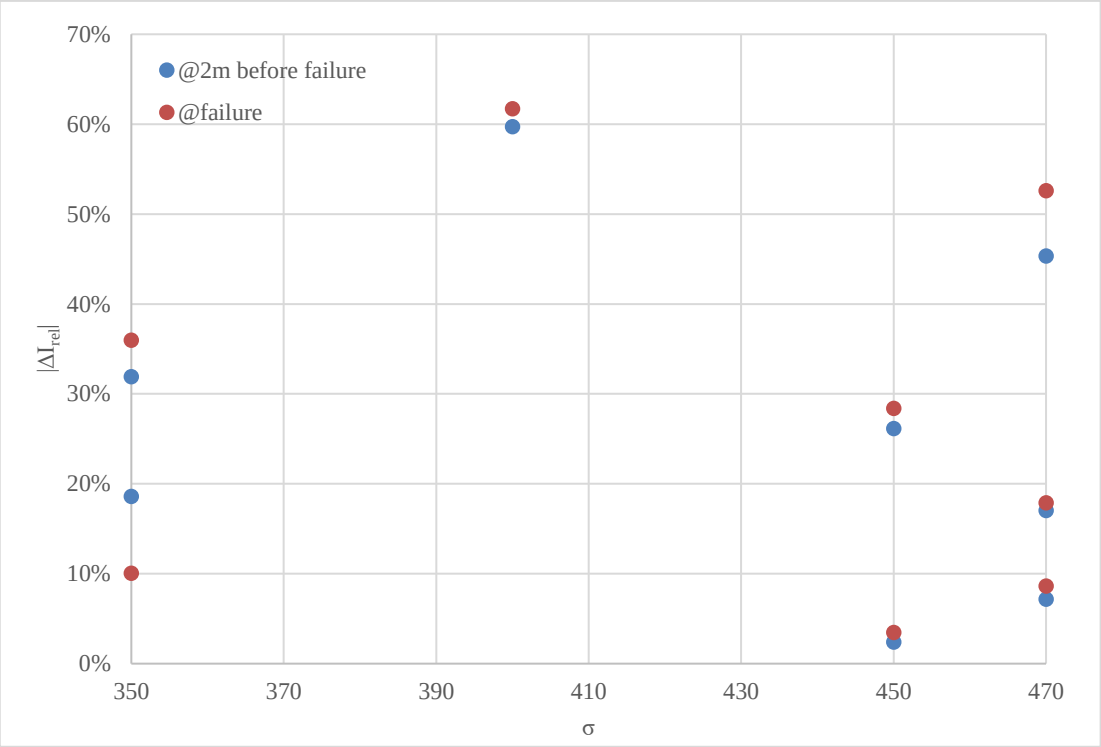

Figure 5.26 - ΔI vs load level at failure point and 2 minutes before the failure reference

Figure 5.26 presents the percentage difference in current at each load level. The orange point indicates the current difference from the beginning of the test to the point of specimen failure, while the blue points represent the current difference from the start to two minutes before the specimen's failure. Due to the instability of the current readings, it is difficult to draw definitive conclusions about the current trend. This instability is primarily attributed to the limitations of the current meter, particularly in long-term experiments where the battery cannot sustain operation for the entire duration.

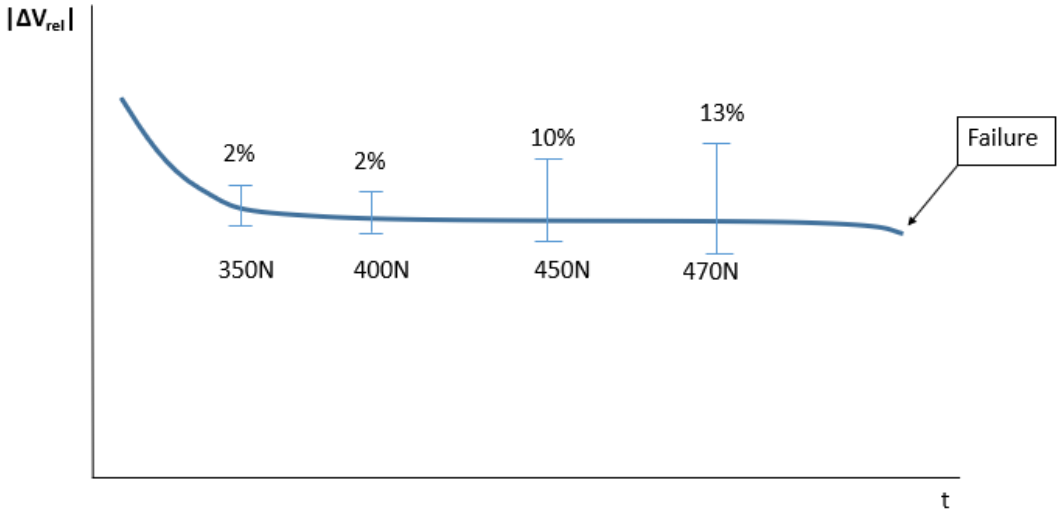

Figure 5.27 - ΔV percentage in function of load level along the time

Figure 5.27 summarizes the key findings of this chapter, highlighting the relationship between ΔV and load level. At lower loads (350 N and 400 N), the voltage difference (|ΔV_rel|) remains minimal and almost identical for both conditions, approximately 2%. However, when the load increases to 450 N and 470 N, |ΔV_rel| shows a substantial increase, from 10% to 13%. In particular, when the sample does not reach failure, the root mean square values of stress, current, and acceleration remain stable over time.

5.6.1 Contributions to research

In this chapter, the main contributions to research are related to

- Early damage detection in the field of very high cycle fatigue (VHCF) testing of PEEK materials.

The results will be reported in a high impact factor international journal of fatigue, which is under development.

6. FINAL CONCLUSION

This work has been structured to present conclusions, discussions, and other key aspects at strategic points throughout the thesis. Therefore, this chapter provides only a high-level overview, offering general conclusions and reflections. It also includes observations on the main achievements and novelties of the project.

In particular, the general conclusions are first provided in the form of a concise summary of all the chapters of this thesis. Then, more details are given related to

1) multiphysics design and modelling of WFSG for aerospace applications;
2) thermal rotor modelling of WFSM for traction applications;
3) fatigue monitoring of PEEK material.

Finally, some ideas for future work are also included.

6.1. General conclusions and future works

This research has highlighted the challenges and opportunities of employing WFSM in the transportation sector. Through a comprehensive multiphysics design and modelling approach, WFSM emerges as a promising alternative to PM machines.

In Chapter 2, a thorough literature review was conducted on the use of WFSM in the aerospace and automotive industries, emphasizing the importance of a multiphysics methodology. This laid the foundation for the advanced analytical and numerical tools (i.e., 3D TEC, 2D and 3D FE, 3D CFD) developed throughout the study, which were specifically designed to address the thermal and mechanical challenges. This chapter was fundamental to understand the state of the art of multiphysics modelling of electric machines, in particular those with WFSM, and to define the novelty of the thesis, as discussed in detail in chapters 4 and 5.

Chapter 3 focused on the structural integrity of the WFSM rotor at high rotational speeds, presenting a solution to enhance rotor durability by incorporating a 4 mm non-electrical steel layer at the rotor end caps. This design allows the rotor to operate safely at 15 krpm while promoting axial air flow for cooling. Simulations suggest that this solution could enable a reduction in airgap thickness from 2 mm to 1 mm, potentially improving machine performance. This solution is highly innovative because, in the current state of the art, only rotor cages are used, which prevent active cooling of the rotor and significantly increase its weight. Future work will further explore this geometric optimization. Additionally, both the stator and rotor winding temperatures remain well below the insulation class limits, indicating considerable potential for increasing current density and thereby enhancing overall WFSM performance. This is a significant achievement, as it allows for an increase in power density while keeping costs low. The downside, however, is that the generator has been electromagnetically designed to operate in the 15 krpm range. These optimizations will be further investigated in future studies.

Chapter 4 addressed the thermal management challenges of the WFSM rotor, proposing a design approach for electrical machines specifically tailored to transportation applications. A TEC model was developed to strike an efficient balance between computational time and accuracy in estimating heat extraction for both passive (hollow shaft) and active (axial fan) cooling systems. Despite the simplified geometric assumptions (modeled as two concentric cylinders), the TEC model showed strong agreement with FE simulations. The CFD model further highlighted the importance of predicting heat transfer coefficients through CHT models, which accurately replicate fluid dynamics based on machine geometry, operating conditions, and cooling systems. While active cooling introduces added complexity and potential mechanical power losses due to aerodynamic effects, these drawbacks can be mitigated through optimized subsystem integration and intelligent thermal management, which will be explored in future research. The main advantage of this approach is that, once the machine's targets are defined, the machine designer can select the appropriate cooling system and then optimize it using detailed models. The drawback is that the machine is considered as a cylinder

but as discussed in the thesis, by calibrating the model with experimental or numerical data, a more accurate result can be achieved.

Due to delays in the machine's manufacturing process, the experimental validation of the scientific findings could not be conducted. At the time of writing this thesis, the machine was still in production.

Lastly, Chapter 5 explored VHCF testing of PEEK, a material widely used as insulation in electrical machines. The degradation and aging of electrical insulation systems are becoming increasingly critical in the development of electrified vehicles, as they directly impact both cost optimization and the longevity of electrical machines. While thermal-mechanical aging in electrical machines is well-documented, limited research exists on the VHCF behaviour of PEEK.This study introduced time- and frequency-based methods for early damage detection during stress-controlled fatigue tests. The voltage signal demonstrated a proportional increase in voltage drop with rising load levels, serving as a key early indicator of specimen failure. However, when failure was not reached, the RMS values of current, voltage, and acceleration remained stable over time.Future work will focus on automating post-processing analysis and reducing the sampling time from 2 minutes to 30 seconds, enabling more precise failure predictions within the critical range.

REFERENCES

[1] J. Benzaquen, J. He and B. Mirafzal, "Toward more electric powertrains in aircraft: Technical challenges and advancements," in CES Transactions on Electrical Machines and Systems, vol. 5, no. 3, pp. 177-193, Sept. 2021, doi: 10.30941/CESTEMS.2021.00022.

[2] E. Sayed et al., "Review of Electric Machines in More-/Hybrid-/Turbo-Electric Aircraft," in IEEE Transactions on Transportation Electrification, vol. 7, no. 4, pp. 2976-3005, Dec. 2021, doi: 10.1109/TTE.2021.3089605.

[3] I. O. Hockmeyer. "‘e generation and regulation of electric power in aircra‰: a survey of
design features of generators and their control". In: Journal of the Institution of Electrical
Engineers - Part II: Power Engineering 93.31 (1946), pp. 2.

[4] V. Madonna, P. Giangrande, and M. Galea. "Electrical Power Generation in Aircraft: Review, Challenges, and Opportunities". In: IEEE Transactions on Transportation Electrification 4.3 (2018), pp. 646–659.

[5] I. Moir, A. Seabridge, and M. Jukes. Civil Avionics Systems. Aerospace Series. Wiley, 2013.

[6] W. K. Boice and L. G. Levoy. "Basic considerations in selection of electric systems for large aircraft". In: Electrical Engineering 63.6 (1944), pp. 279–287.

[7] J. A. Rosero et al. "Moving towards a more electric aircra.". In: IEEE Aerospace and Electronic Systems Magazine 22.3 (2007), pp. 3–9.

[8] P. Wheeler and S. Bozhko. ".e More Electric Aircra.: Technology and challenges." In: IEEE Electri€cation Magazine 2.4 (2014), pp. 6–12.

[9] K. Ni et al. "Electrical and Electronic Technologies in More-Electric Aircra.: A Review". In: IEEE Access 7 (2019).

[10] C. Anghel, "Modeling and simulation of a power generation system with a high power generator," SAE Tech. Paper 2013-01-2126, 2013.

[11] V. Madonna, A. Walker, P. Giangrande, G. Serra, C. Gerada, and M. Galea, "Improved thermal management and analysis for stator endwindings of electrical machines," IEEE Trans. Ind. Electron., vol. 66, no. 7, pp. 5057–5069, Jul. 2019, doi: 10.1109/TIE.2018.2868288.

[12] K. Bersch et al., “Combined thermofluid and electromagnetic optimisation of stator vent cooling,” in Proc. 13th Int. Conf. Electr. Mach. (ICEM), Sep. 2018, pp. 1116–1122, doi:10.1109/icelmach.2018.8507231.

[13] A. Guiducci et al., "Refined Structural Design and Thermal Analyses of a High-Speed Wound-Field Generator for the More Electrical Aircraft," 2023 IEEE Workshop on Electrical Machines Design, Control and Diagnosis (WEMDCD), Newcastle upon Tyne, United Kingdom, 2023, pp. 1-6, doi: 10.1109/WEMDCD55819.2023.10110937.

[14] D. Gerada, A. Mebarki, N. L. Brown, C. Gerada, A. Cavagnino, and A. Boglietti, “High-speed electrical machines: Technologies, trends, and developments,” *IEEE Trans. Ind. Electron.*, vol. 61, no. 6, pp. 2946–2959, Jun. 2014, doi: 10.1109/TIE.2013.2286777.

[15] A. L. Rocca *et al.*, “Thermal management of a high speed permanent magnet machine for an aeroengine,” in *Proc. 13th Int. Conf. Electr. Mach. (ICEM)*, Sep. 2016, pp. 2732–2737, doi: 10.1109/ icelmach.2016.7732908 .

[16] Z. Xu *et al.*, “Thermal management of a permanent magnet motor for an directly coupled pump,” in *Proc. 13th Int. Conf. Electr. Mach. (ICEM)*, Sep. 2016, pp. 2738–2744, doi: 10.1109/ICELMACH. 2016.7732909.

[17] V. Madonna, P. Giangrande, A. Walker, and M. Galea, “On the effects of advanced end-winding cooling on the design and performance of electrical machines,” in *Proc. 13th Int. Conf. Electr. Mach. (ICEM)*, Sep. 2018, pp. 311–317, doi: 10.1109/ICELMACH.2018. 8507170.

[18] S. Nuzzo, N. L. Brown, M. Galea, C. Gerada, D. Gerada, and A. Mebarki, “Damper cage loss reduction and no-load voltage THD improvements in salient-pole synchronous generators,” in Proc. 8th IET Int. Conf. Power Electron., Mach. Drives (PEMD), 2016, pp. 1–7, doi: 10.1049/cp.2016.0203

[19] D. D. Pollard and G. E. Krajci, “Packaging the VSCF system for an aircraft engine environment,” SAE Tech. Paper 811088, 1981.

[20] A. Di Gioia et al., “Design of a wound field synchronous machine for electric vehicle traction with brushless capacitive field excitation,” in Proc. IEEE Energy Convers. Congr. Expo. (ECCE), Sep. 2016, pp. 1–8, doi: 10.1109/ECCE.2016.7855023.

[21] L. Andrade and C. Tenning, “Design of the Boeing 777 electric system,” in Proc. IEEE Nat. Aerosp. Electron. Conf. @m_NAECON, vol. 3, May 1992, pp. 1281–1290, doi: 10.1109/NAECON.1992. 220573.

[22] S. Jacobs, E. Liebermann, and C. Babad, “Altitude performance test results for low pressure turbine mounted generator,” SAE Tech. Paper 2006-01-3056, 2006.

[23] B. Bilgin and A. Emadi, “Electric motors in electrified transportation,” IEEE Power Electron. Mag., vol. 1, no. 2, pp. 10–12, Jun. 2014.

[24] M. A. Rahman, M. A. Mansur, and M. N. Uddin, “Impacts of interior permanent magnet machine technology for electric vehicles,” in Proc. IEEE Int. Electr. Veh. Conf., Greenville, SC, USA, Mar. 2012, pp. 1–5.

[25] G. Petrelli et al., "Comparison of Aluminium and Copper Conductors in Hairpin Winding Design for High Power Density Traction Motors," 2022 International Conference on Electrical Machines (ICEM), Valencia, Spain, 2022, pp. 1635-1641, doi: 10.1109/ICEM51905.2022.9910796.

[26] R. Thomas, L. Garbuio, L. Gerbaud and H. Chazal, "Modeling and design analysis of the Tesla Model S induction motor," 2020 International Conference on Electrical Machines (ICEM), Gothenburg, Sweden, 2020, pp. 495-501, doi: 10.1109/ICEM49940.2020.9270646.

[27] Y. Xu, Z. Xu, H. Cao and W. Liu, "Torque Ripple Suppression of Synchronous Reluctance Motors for Electric Vehicles Based on Rotor Improvement Design," in IEEE Transactions on Transportation Electrification, doi: 10.1109/TTE.2022.3231301.

[28] M. Di Nardo et al., "High Speed Permanent Magnet Assisted Synchronous Reluctance Machines – Part II: Performance Boundaries," in IEEE Transactions on

Energy Conversion, vol. 37, no. 4, pp. 2567-2577, Dec. 2022, doi: 10.1109/TEC.2022.3176383.

[29] G. Klempner, I. Kerszenbaum, “Operation and control,” in Handbook of Large Turbo-Generator Operation And Maintenance. NY, NY, USA: Wiley IEEE Press, 2018, pp. 201–330.

[30] S. Nuzzo et al., "A Methodology to Remove Stator Skew in Small–Medium Size Synchronous Generators via Innovative Damper Cage Designs," in IEEE Transactions on Industrial Electronics, vol. 66, no. 6, pp. 4296-4307, June 2019, doi: 10.1109/TIE.2018.2864699.

[31] Y. Wang, S. Nuzzo, H. Zhang, W. Zhao, C. Gerada and M. Galea, "Challenges and Opportunities for Wound Field Synchronous Generators in Future More Electric Aircraft," in IEEE Transactions on Transportation Electrification, vol. 6, no. 4, pp. 1466-1477, Dec. 2020, doi: 10.1109/TTE.2020.2980189.

[32] G. Devito, S. Nuzzo, D. Barater and G. Franceschini, "A Simplified Analytical Approach for Hybrid Exciters of Wound-Field Generators," in IEEE Transactions on Transportation Electrification, vol. 8, no. 4, pp. 4303-4312, Dec. 2022, doi: 10.1109/TTE.2022.3167797.

[33] Nonaka, S. and Kesamary, K. (1981), Brushless self-excited singlephase synchronous generator using wound rotor type three-phase induction machine. Elect. Eng. Jpn., 101: 109-116. https://doi.org/10.1002/eej.4391010614

[34] Izzat, L.F., & Heier, S. (2013). Development in design of brushless self-excited and self-regulated synchronous generator. 2013 International Conference on Renewable Energy Research and Applications (ICRERA), 1024-1029.

[35] G. Petrelli, S. Nuzzo, T. Zou, D. Barater, G. Franceschini and C. Gerada, "Review and Future Developments of Wound Field Synchronous Motors in Automotive," 2023 IEEE International Conference on Electrical Systems for Aircraft, Railway, Ship Propulsion and Road Vehicles & International Transportation Electrification Conference (ESARS-ITEC), Venice, Italy, 2023, pp. 1-6, doi: 10.1109/ESARS-ITEC57127.2023.10114826.

[36] D. G. Dorrell, "Are wound-rotor synchronous motors suitable for use in high efficiency torque-dense automotive drives?," IECON 2012 - 38th Annual Conference on IEEE Industrial Electronics Society, Montreal, QC, Canada, 2012, pp. 4880-4885, doi: 10.1109/IECON.2012.6389578.

[37] Hussain, A.; Baig, Z.; Toor, W.T.; Ali, U.; Idrees, M.; Shloul, T.A.; Ghadi, Y.Y.; Alkahtani, H.K. Wound Rotor Synchronous Motor as Promising Solution for Traction Applications. Electronics 2022, 11, 4116. https://doi.org/10.3390/electronics11244116

[38] S. Sakurai, T. Suwazono, “EV Traction Wound Field Syncrhonous Motor”. [Online] Available: https://www.meidensha.co.jp/rd/rd_02/rd_02_02/rd_02_02_10/rd_02_02_05_01/__icsFiles/afieldfile/2021/06/14/Review_182_07_web_210607_1.pdf

[39] W. Chai, J. -W. Kwon and B. -I. Kwon, "Analytical Design of a Hybrid-Excited Wound Field Synchronous Machine for the Improvement of Torque Characteristics," in IEEE Access, vol. 8, pp. 87414-87421, 2020, doi: 10.1109/ACCESS.2020.2993317.

[40] W. Chai, W. Zhao and B. -i. Kwon, "Optimal Design of Wound Field Synchronous Reluctance Machines to Improve Torque by Increasing the Saliency Ratio," in IEEE Transactions on Magnetics, vol. 53, no. 11, pp. 1-4, Nov. 2017, Art no. 8206604, doi: 10.1109/TMAG.2017.2707459.

[41] S. -I. Park and K. -C. Kim, "Torque Ripple Reduction Method With Asymmetric Pole for Wound-Field Synchronous Motor," in IEEE Transactions on Magnetics, vol. 51, no. 3, pp. 1-4, March 2015, Art no. 8102504, doi: 10.1109/TMAG.2014.2357853.

[42] Do, Sang-Hwa & Lee, Byeong-Hwa & Lee, Ho-Young & Hong, J.P. (2012). Torque ripple reduction of wound rotor synchronous motor Conference on Electrical Machines and Systems. 1-4.

[43] H. -J. Park and M. -S. Lim, "Design of High Power Density and High Efficiency Wound-Field Synchronous Motor for Electric Vehicle Traction," in

IEEE Access, vol. 7, pp. 46677-46685, 2019, doi: 10.1109/ACCESS.2019.2907800.

[44] S. Nuzzo, D. Barater, C. Gerada and P. Vai, "Hairpin Windings: An Opportunity for Next-Generation E-Motors in Transportation," in IEEE Industrial Electronics Magazine, vol. 16, no. 4, pp. 52-59, Dec. 2022, doi: 10.1109/MIE.2021.3106571.

[45] EU: LIGHT-DUTY: NEW EUROPEAN DRIVING CYCLE OVERVIEW and DESCRIPTION https://www.transportpolicy.net/standard/eu-light-duty-neweuropean- driving-cycle/.

[46] Y. Wang, S. Nuzzo, C. Gerada, W. Zhao, H. Zhang and M. Galea, "3D Lumped Parameter Thermal Network for Wound-Field Synchronous Generators," 2021 IEEE Workshop on Electrical Machines Design, Control and Diagnosis (WEMDCD), Modena, Italy, 2021, pp. 5-9, doi: 10.1109/WEMDCD51469.2021.9425624.

[47] F.Graffeo, “Design and analysis of different rotor configurations for wound field synchronous machines”, M.S. thesis, Dept. El. Eng., Politecnico di Torino, Torino, Italy, 2020

[48] A. Guiducci, S. Nuzzo, D. Barater, G. Franceschini and R. Wrobel, "Thermal Modelling of Advanced Rotor Cooling Solutions for Traction Applications," 2024 International Conference on Electrical Machines (ICEM), Torino, Italy, 2024, pp. 1-7, doi: 10.1109/ICEM60801.2024.10700224.

[49] A. Saleem, Y. Zhang, H. Gong, and M. K. Majeed, “Fluoride doped SiC/Si3N4 composite as a high thermal conductive material with enhanced mechanical properties,” Ceram. Int., vol. 45, no. 16, pp. 21004–21010, Nov. 2019, doi: 10.1016/j.ceramint.2019.06.289

[50] T. Zou et al., "A Comprehensive Design Guideline of Hairpin Windings for High Power Density Electric Vehicle Traction Motors," in IEEE Transactions on Transportation Electrification, vol. 8, no. 3, pp. 3578-3593, Sept. 2022, doi: 10.1109/TTE.2022.3149786.

[51] Fallows, Daniel & Nuzzo, Stefano & Galea, Mikiel. (2021). Exciterless Wound-Field Medium-Power Synchronous Machines: Their History and Future. IEEE Industrial Electronics Magazine. PP. 2-9. 10.1109/MIE.2021.3093024.

[52] M. G. Pasquinelli, P. Bolognesi, A. Guiducci, S. Nuzzo and M. Galea, "Design of a High-Speed Wound-Field Synchronous Generator for the More Electric Aircraft," 2021 IEEE Workshop on Electrical Machines Design, Control and Diagnosis (WEMDCD), Modena, Italy, 2021, pp. 64-69, doi:10.1109/WEMDCD51469.2021.9425625.

[53] Bramerdorfer, G., Marth, E., Nuzzo, S., & Galea, M. (2020). Multi- Objective Optimization of Medium-Scale Wound-Field Electric Generators. In CEFC 2020 - Selected Papers from the 19th Biennial IEEE Conference on Electromagnetic Field Computation [9451327] https://doi.org/10.1109/CEFC46938.2020.9451327.

[54] Bramerdorfer, G., Marth, E., Nuzzo, S., & Galea, M. (2020). Multi-Objective Optimization of Medium-Scale Wound-Field Electric Generators. In CEFC 2020 - Selected Papers from the 19th Biennial IEEE Conference on Electromagnetic Field Computation [9451327] https://doi.org/10.1109/CEFC46938.2020.9451327.

[55] J. R. Hendershot and T. J. E. Miller, *Design of brushless permanent magnet machines*. Motor Design Books Venice, Florida, USA, 2010.

[56] T. A. Lipo, *Introduction to AC machine design*. John Wiley & Sons, 2017.

[57] J. Pyrhonen, T. Jokinen, and V. Hrabovcova, *Design of rotating electrical machines*. John Wiley & Sons, 2013.

[58] V. Ostović, “The Art and Science of Rotating Field Machines Design,” 2017.

[59] W. Tong, *Mechanical design of electric motors*. CRC press, 2014.

[60] A. Krings, A. Boglietti, A. Cavagnino, and S. Sprague, “Soft magnetic material status and trends in electric machines,” *IEEE Trans. Ind. Electron.*, vol. 64, no. 3, pp. 2405–2414, 2016.

[61] F. Fiorillo, “Magnetic materials for electrical applications: A Review,” Torino, 2010.

[62] A. El-Refaie, “Role of advanced materials in electrical machines,” *CES Trans. Electr. Mach. Syst.*, vol. 3, no. 2, pp. 124–132, 2019.

[63] M. A. Darmani, E. Poskovic, L. Ferraris, and A. Cavagnino, “Multiple Layer Compression of SMC and PM Powdered Materials,” in *IECON 2019 - 45th Annual Conference of the IEEE Industrial Electronics Society*, Oct. 2019, pp. 1216–1221.

[64] M. A. Darmani, E. Poskovic, S. Vaschetto, F. Franchini, L. Ferraris, and A. Cavagnino, “Multilayer Bonded Magnets in Surface-Mounted PM Synchronous Machines,” in *2020 IEEE Energy Conversion Congress and Exposition (ECCE)*, Oct. 2020, pp. 1052–1059.

[65] R. Hemmati, F. Wu, and A. El-Refaie, “Survey of insulation systems in electrical machines,” in Conf. Rec. *IEMDC*, 2019, pp. 2069–2076.

[66] M. Borghei and M. Ghassemi, “Insulation materials and systems for more and all-electric aircraft: A review identifying challenges and future research needs,” *IEEE Trans. Transp. Electrif.*, 2021.

[67] Y. Zhao, D. Li, T. Pei, and R. Qu, “Overview of the rectangular wire windings AC electrical machine,” *CES Trans. Electr. Mach. Syst.*, vol. 3, no. 2, pp. 160–169, 2019.

[68] M. Rios, G. Venkataramanan, A. Muetze, and H. Eickhoff, “Thermal Performance Modeling of Foil Conductor Concentrated Windings in Electric Machines,” IEEE Trans. Ind. Appl., vol. 54, no. 5, 2018.

[69] S. Chapman, Electric machinery fundamentals, New York: McGraw-Hill, 2005.

[70] P. R. C. a. A. S. H. David A. Howey, «Airgap convection in rotating electrical machines,» *IEEE Transactions on Industry Electronics*, vol. 59, n. 3, pp. 1367-1375, 2012.

[71] D. S. A. B. A. C. D. H. a. J. G. Mircea Popescu, «Modern heat extraction systems for electrical machines - a review.,» IEEE Workshop on Electrical Machines Design, Control and Diagnosis (WEMDCD) , 2015.
[72] Y. A.-A. K. R. J. e. a. Yang, «State-of-the-art electrified powertrains: hybrid, plug-in hybrid, and electric vehicles,» *Int. J. Powertrains,* vol. 5, pp. 1-28, 2016.
[73] P. M. S. W. Group, "IEEE Standard Test Procedure for Thermal Evaluation of Systems of Insulating Materials for Random-wound AC Electric Machinery," IEEE Std, pp. 117–2015, 2015.

[74] S. Xue, W. Q. Chu, Z. Q. Zhu, J. Peng, S. Guo, and J. Feng, "Iron loss calculation considering temperature influence in non-oriented steel laminations," *IET Sci. Meas. Technol.*, vol. 10, no. 8, 2016.
[75] X. Pei, A. C. Smith, L. Vandenbossche, and J. Rens, "Magnetic characterization of soft magnetic cores at cryogenic temperatures," *IEEE Trans. Appl. Supercond.*, vol. 29, no. 5, pp. 1–6, 2019.
[76] Arnold Magnetic Technologies, "Using Permanent Magnets at Low Temperature," 2015.
[77] M. Seif *et al.*, *Temperature-dependent material modeling for structural steels: formulation and application*. US Department of Commerce, National Institute of Standards and Technology, 2016.
[78] R. Wrobel, P. H. Mellor, M. Popescu and D. A. Staton, "Power Loss Analysis in Thermal Design of Permanent-Magnet Machines—A Review," in IEEE Transactions on Industry Applications, vol. 52, no. 2,
pp. 1359-1368, March-April 2016, doi: 10.1109/TIA.2015.2489599.
[79] Z. Gmyrek and A. Cavagnino, "Influence of punching, welding, and clamping on magnetic cores of fractional kilowatt motors," *IEEE Trans. Ind. Appl.*, vol. 54, no. 5, pp. 4123–4132, 2018.
[80] P. O. Gronwald and T. A. Kern, "Traction Motor Cooling Systems: A Literature Review and Comparative Study," IEEE Transactions on Transportation Electrification, vol. 7, no. 4. Institute of Electrical and Electronics Engineers Inc., pp. 2892–2913, Dec. 01, 2021.

[81] M. Popescu, D. Staton, A. Boglietti, A. Cavagnino, D. Hawkins, and J. Goss, “Modern heat extraction systems for electrical machines – A review,” in Proceedings - 2015 IEEE Workshop on Electrical Machines Design, Control and Diagnosis, WEMDCD 2015, Aug. 2015, pp. 289– 296.

[82] F. Zhang et al., “Back-Iron Extension Thermal Benefits for Electrical Machines with Concentrated Windings,” IEEE Trans. Ind. Electron., vol. 67, no. 3, pp. 1728–1738, Mar. 2020.

[83] S. Nategh et al., “A Review on Different Aspects of Traction Motor Design for Railway Applications,” in IEEE Transactions on Industry Applications, May 2020, vol. 56, no. 3, pp. 2148–2157.

[84] P. Shams Ghahfarokhi, A. Kallaste, T. Vaimann, and A. Belahcen, “Thermal Analysis of Totally Enclosed Fan Cooled Synchronous Reluctance Motor-state of art - IEEE Conference Publication,” in IECON 2019 - 45th Annual Conference of the IEEE Industrial Electronics Society, 2019, pp. 1–5.

[85] P. Lindh et al., “Direct Liquid Cooling Method Verified with an Axial-Flux Permanent-Magnet Traction Machine Prototype,” IEEE Trans. Ind. Electron., vol. 64, no. 8, pp. 6086–6095, Aug. 2017.

[86] P. Lindh, I. Petrov, J. Pyrhonen, E. Scherman, M. Niemela, and P. Immonen, “Direct Liquid Cooling Method Verified with a Permanent-Magnet Traction Motor in a Bus,” IEEE Trans. Ind. Appl., vol. 55, no. 4, pp. 4183–4191, Jul. 2019.

[87] N. A. Rahman, E. Bostanci, and B. Fahimi, “Thermal analysis of switched reluctance motor with direct in-winding cooling system,” Jan. 2017.

[88] E. Nitsche and M. Naderer, “Internally Cooled Hollow Wires Doubling the Power Density of Electric Motors,” ATZelektronik Worldw., vol. 12, no. 3, pp. 42–47, Jun. 2018.

[89] P. Lindh et al., “Performance of a Direct-Liquid-Cooled Motor in an Electric Bus under Different Load Cycles,” IEEE Access, vol. 7, pp. 86897–86905, 2019.

[88] M. Popescu, D. A. Staton, A. Boglietti, A. Cavagnino, D. Hawkins, and J. Goss, “Modern Heat Extraction Systems for Power Traction Machines—A Review,” IEEE Trans. Ind. Appl., vol. 52, no. 3, pp. 2167–2175, May 2016.

[89] Z. Xu et al., “A semi-flooded cooling for a high speed machine: Concept, design and practice of an oil sleeve,” in Proceedings IECON 2017 - 43rd Annual Conference of the IEEE Industrial Electronics Society, Dec. 2017, vol. 2017-Janua, pp. 8557–8562.

[90] P. Arumugam et al., “Permanent magnet starter-generator for aircraft application,” in SAE Technical Papers, 2014, vol. 2014-Septe, no. September.

[91] A. Tüysüz, F. Meyer, M. Steichen, C. Zwyssig, and J. W. Kolar, “Advanced Cooling Methods for High-Speed Electrical Machines,” IEEE Trans. Ind. Appl., vol. 53, no. 3, pp. 2077–2087, May 2017.

[92] A. Acquaviva, S. Skoog, E. Grunditz, and T. Thiringer, “Electromagnetic and Calorimetric Validation of a Direct Oil Cooled Tooth Coil Winding PM Machine for Traction Application,” Energies, vol. 13, no. 13, pp. 33-39, Jun. 2020.

[93] C. Liu et al., “Experimental Investigation on Oil Spray Cooling with Hairpin Windings,” IEEE Trans. Ind. Electron., vol. 67, no. 9, pp. 7343–7353, Sep. 2020.

[94] T. Davin, J. Pellé, S. Harmand, and R. Yu, “Experimental study of oil cooling systems for electric motors,” Appl. Therm. Eng., vol. 75, pp. 1–13, Jan. 2015.

[95] C. Liu et al., “Estimation of Oil Spray Cooling Heat Transfer Coefficients on Hairpin Windings with Reduced-parameter Models,” IEEE Trans. Transp. Electrif., pp. 1–1, Oct. 2020.

[96] Y. Gai et al., “Cooling of Automotive Traction Motors: Schemes, Examples, and Computation Methods,” IEEE Trans. Ind. Electron., vol. 66, no. 3, pp. 1681–1692, Mar. 2019.

[97] M. Jaensch, “Cooling Concepts of High-Power Electric Machines,” in Future Powertrain Conference 2019, Feb. 2019, pp. 1–13.

[98] Y. Gai et al., “Shaft cooling and the influence on the electromagnetic performance of traction motors,” Aug. 2017.

[99] “Technology highlight: Audi’s internal rotor cooling | Engine + Powertrain Technology International.” https://www.enginetechnologyinternational.com/features/technologyhighlight-audis-internal-rotor-cooling.html#prettyPhoto.

[100] R. Thomas, L. Garbuio, L. Gerbaud, and H. Chazal, “Modeling and design analysis of the Tesla Model S induction motor,” in Proceedings - 2020 International Conference on Electrical Machines, ICEM 2020, Aug. 2020, pp. 495–501.

[101] Audi, “Audi e-tron cooling concept e-motor (animation) | Video | Audi MediaTV,” 2021. https://www.audimediacenter.com/en/audimediatv/video/audi-e-tron-cooling-concept-emotor-animation-4847.

[102] G. Liang and I. Mudawar, “Review of spray cooling – Part 1: Singlephase and nucleate boiling regimes, and critical heat flux,” International Journal of Heat and Mass Transfer, vol. 115. Elsevier Ltd, pp. 1174–1205, Dec. 01, 2017.

[103] I. Mudawar, “Recent advances in high-flux, two-phase thermal management,” J. Therm. Sci. Eng. Appl., vol. 5, no. 2, May 2013.

[104] K. A. Estes and I. Mudawar, “Comparison of two-phase electronic cooling using free jets and sprays,” J. Electron. Packag. Trans. ASME, vol. 117, no. 4, pp. 323–332.

[105] J. X. Wang et al., “Investigation of a spray cooling system with two nozzles for space application,” Appl. Therm. Eng., vol. 89, pp. 115–124, Jun. 2015.

[106] P. Shams Ghahfarokhi, A. Podgornovs, A. Kallaste, A. J. Marques Cardoso, A. Belahcen and T. Vaimann, "The Oil Spray Cooling System of Automotive Traction Motors: The State of the Art," in *IEEE Transactions on Transportation Electrification*, vol. 9, no. 1, pp. 428-451, March 2023, doi: 10.1109/TTE.2022.3189596

[107] Z. Li, D. Fu, J. Guo, G. Gu, and B. Xiong, “Study on spraying evaporative cooling technology for the large electrical machine,” 2009.

[108] B. B. M. K. S. N. H. S. M. J. C. N. S. A. E. Yinye Yang, «“Thermal management of electric machines”».

[109] A. C. S. M. S. M. M. a. C. M. Aldo Boglietti, “Evolution and Modern Approaches for Thermal Analysis of Electrical Machines,” *IEEE TRANSACTIONS ON INDUSTRIAL ELECTRONICS*, vol. 56, no. 3, MARCH 2009.

[110] K. A. R. Srinivas, «Analysis and characterization of switched reluctance motors: part ii - flow, thermal and vibration analyses,» *IEEE Trans. Magn.*, pp. 1321-1332, 2005.

[111] Y. A.-A. K. R. J. e. a. Yang, «State-of-the-art electrified powertrains: hybrid, plug-in hybrid, and electric vehicles,» *Int. J. Powertrains*, vol. 5, pp. 1-28, 2016.

[112] R. Lin, S. D. Sudhoff, and C. Krousgrill, “Analytical method to compute bridge stresses in V-shape IPMs,” IET Electr. Power Appl., vol. 12, no. 7, pp. 938–945, 2018.

[113] Shimizu S, Tosha K, Tsuchiya K. New data analysis of probabilistic stress-life (P-SN) curve and its application for structural materials. Int J Fatig 2010;32:565 – 75.

[114] Manikkavel A, Kumar V, Lee DJ. Simple fracture model for an electrode and interfacial crack in a dielectric elastomer under tensile loading. Theor Appl Fract Mech 2020;108:102626.

[115] Davino D, Krejci P, Pimenov A, Rachinskii D, Visone C. Analysis of an operator differential model for magnetostrictive energy harvesting. Commun Nonlinear Sci Numer Simul 2016;39:504 – 19.

[116] Sangid MD. The physics of fatigue crack initiation. Int J Fatig 2013;57:5872.

[117] Chan KS. Roles of microstructure in fatigue crack initiation. Int J Fatig 2010;32:1428 – 47.

[118] J. C. Shaw, S. D. A. Fletcher, P. J. Norman, and S. J. Galloway. More electric power system concepts for an environmentally responsible aircraft (n+2). In 2012 47th International Universities Power Engineering Conference (UPEC), pages 1–6, 2012.

[119] P. Wheeler and S. Bozhko. The more electric aircraft: Technology and challenges. IEEE Electrification Magazine, 2(4):6–12, 2014.

[120] P. Wheeler. Technology for the more and all electric aircraft of the future. In 2016 IEEE International Conference on Automatica (ICAACCA), pages 1–5, 2016.

[121] Y.Wang et al., ”Integrated Damper Cage for THD Improvements of Variable Speed Salient-Pole Synchronous Generators for the More Electric Aircraft,” in IEEE Transactions on Transportation Electrification, doi: 10.1109/TTE.2021.3139366.

[122] H. Guo et al., ”Comprehensive Analysis and Solution of Voltage Build-Up Failure in Aircraft PM-Assisted Reluctance Starter/Generator System,” in IEEE Transactions on Industrial Electronics, 2022, doi: 10.1109/TIE.2022.3217611

[123] N. B. a. S. Bolognani, Metodologia di progettazione delle macchine elettriche, CLEUP, 2001.

[124] P. Bolognesi, «A mid-complexity analysis of long-drum-type electric machines suitable for circuital modeling,» In 18th International Conference on Electrical Machines, pp. 1-5, 2008.

[125] P. B. C. G. a. M. G. S. Nuzzo, «Simplified damper cage circuital model and fast analytical–numerical approach for the analysis of synchronous generators,» IEEE Transactions on Industrial Electronics, vol. 66, n. 11, p. 8361–8371, 2019.

[126] Mircea Popescu, Dave Staton, Aldo Boglietti, Andrea Cavagnino, Douglas Hawkins, and James Goss. Modern heat extraction systems for electrical machines - a review. IEEE Workshop on Electrical Machines Design, Control and Diagnosis (WEMDCD), 2015.

[127] Cicalese, G., Berni, F., Fontanesi, S. Integrated in-cylinder / CHT methodology for the simulation of the engine thermal field: An application to high performance turbocharged DISI engines (2016) SAE
International Journal of Engines, 9 (1), DOI: 10.4271/2016-01-0578

[128] Berni, F., Cicalese, G., Borghi, M., Fontanesi, S. Towards grid- independent 3D-CFD wall-function-based heat transfer models for complex industrial flows with focus on in-cylinder simulations, Applied
Thermal Engineering, Volume 190, 2021, 116838, ISSN 1359-4311, https://doi.org/10.1016/j.applthermaleng.2021.116838.

[129] I. Bjorklund and W. Kays, "Heat transfer between concentric rotating cylinders," Journal of Heat Transfer, vol. 81, pp. 175–186, 1959.

[130] K. Becker and J. Kaye, "Measurements of diabatic flow in an annulus with an inner rotating cylinder," Trans. ASME, Journal of Heat Transfer, vol. 84, pp. 97–105, 1962.

[131] S. Kosterin and Y. Finatev, "Heat transfer in turbulent airflow the annular space between rotating coaxial cylinders (in Russian)," Inzh. Fiz. Z. H., vol. 8, pp. 3–9, 1962.

[132] A hollow-shaft rotor cooling system for automotive traction motors http://theses.ncl.ac.uk/jspui/handle/10443/5024.

[133] M.A. Valenzuela, J.A. Tapia, Heat transfer and thermal design of finned frames for TEFC variable speed motors, Industrial Electronics, IEEE Transactions 55 (10)(2008)3500-3508.

[134] S. Seghir-OualiI, S. Harmand, D. Laloy, Study of the thermal behavior of a synchronous motor with permanent magnets, International Journal of Engineering 3 (3) (1990) 229-256.

[135] M. Fènot, Y. Bertin, E. Dorignac, G. Lalizel, A review of heat transfer between concentric rotating cylinders with or without axial flow, International Journal of Thermal Sciences,Volume 50, Issue 7, 2011, Pages 1138-1155, ISSN 1290-0729.

[136] “The influence of a radial temperature gradient on the instability of fluid flow in an annulus with an inner cylinder rotating,” Trans. ASME, Journal of Heat Transfer, vol. 84, pp. 106–110, 1962.

[137] C. Cez´ario, M. Verardi, S. Borges, J. Silva, A. Antˆonio, and M. Oliveira, “Transient thermal analysis of an induction electric motor,” in Proc. 18th Int. Congr. Mech. Eng., 2005, pp. 1–8.

[138] Y. Gai et al., “On the measurement and modeling of the heat transfer coefficient of a hollow-shaft rotary cooling system for a traction motor,” IEEE Trans. Ind. Appl., vol. 54, no. 6, pp. 5978–5987, Nov. 2018, doi: 10.1109/TIA.2018.2860558.

[139] Y. Gai et al., “Numerical and experimental calculation of CHTC in an oil-based shaft cooling system for a high-speed high-power PMSM,” IEEE Trans. Ind. Electron., vol. 67, no. 6, pp. 4371–4380, Jun. 2020, doi: 10.1109/TIE.2019.2922938.

[140] P.H. MELLOR, D. ROBERT and D R. TURNER, ”Lumped parameter thermal model for electrical machines of TEFC design”, Proc. IEE, vol. 138, no. 5, pp. 205-218, 1991.

[141] J. Nonneman, B. Van der Sijpe, I. T’Jollyn, S. Vanhee, J. Druant, and M. De Paepe, ”Evaluation of High Performance Rotor Cooling Techniques for Permanent Magnet Electric Motors,” in 2021 IEEE International Electric Machines and Drives Conference (IEMDC), 2021, pp. 1-7.

[142] Bathias C, Pineau A. Fatigue of materials and structures, 1st ed., vol. 53 of ISTE. Wiley-ISTE; 2013. s.l..

[143] Wöhler A. Ueber die Festigkeits-Versuche mit Eisen und Stahl 1866:74–106.

[144] Bathias C, Paris PC. Gigacycle fatigue of metallic aircraft components. Int J Fatigue 2010;32(6):894–7.

[145] Haibach E. Betriebsfestigkeit: Verfahren und Daten zur Bauteilberechnung. 3rd ed. Berlin: VDI-Buch, Springer; 2006.

[146] Miner M et al. Cumulative fatigue damage. J Appl Mech 1945(12):A159–64.

[147] Neppiras EA. Techniques and equipment for fatigue testing at very high frequencies 1959(59):691–709.

[148] Stanzl-Tschegg SE. Very high cycle fatigue measuring techniques. Int J Fatigue 2014;60:2–17.

[149] Mayer H. Ultrasonic torsion and tension–compression fatigue testing: measuring principles and investigations on 2024-T351 aluminium alloy. Int J Fatigue 2006;28(11):1446–55.

[150] Marines-Garcia I, Doucet J, Bathias C. Development of a new device to perform torsional ultrasonic fatigue testing. Int J Fatigue 2007;29(9–11):2094–101.

[151] Bathias C. Piezoelectric fatigue testing machines and devices. Int J Fatigue 2006;28(11):1438–45.

[152] Morgan JM, Milligan WW, A 1 kHz Servohydraulic fatigue testing system: symposium proceedings in honor of Professor Paul C. Paris: proceedings of a symposium sponsored by the structural materials division (SMD) of the minerals, metals and materials society (TMS) held during Materials Week ’97 in Indianapolis, IN, September 14–18, 1997, hosted by the Minerals, Metals and Materials Society and ASM International; 1997. p. 305–12.

[153] Nicholas T. Step loading for very high cycle fatigue. Fatigue Fract Eng Mater Struct 2002;25(8–9):861–9.

[154] Morrissey R, Nicholas T. Staircase testing of a titanium alloy in the gigacycle regime. Third international conference on very high cycle fatigue (VHCF-3) third international conference on very high cycle fatigue 2006;28 (11):1577–82.

[155] Murakami Y, Yokoyama NN, Nagata J. Mechanism of fatigue failure in ultralong life regime. Fract Eng Mater Struct 2002;25(8–9):735–46.

[156] Christ H-J. Ermüdungsverhalten metallischer Werkstoffe. 2nd ed. Weinheim: Wiley-VCH-Verl.; 2009.

[157] Jinpeng Li et al 2023 J. Phys.: Conf. Ser. 2457 012026.

[158]https://products.evonik.com/assets/35/91/VESTAKEEP_Compounds_EN_EN_243591.pdf

[159]https://www.zeusinc.com/wpcontent/uploads/2018/01/CS_MotorRewind_PekInsulationMaterial_Zeus.pdf.

[160] https://www.fst.com/news-stories/press-releases/2022/expanding-material-portfolio-for-e-motors/.

[161] Yun GJ, Abdullah ABM, Binienda W. Development of a closed-loop high-cycle resonant fatigue testing system. Exp Mech 2012;52(3):275–88.

[162] George TJ, Seidt J, Herman Shen M-H, Nicholas T, Cross CJ. Development of a novel vibration-based fatigue testing methodology. Int J Fatigue 2004;26 (5):477–86.